Title
Fabrication of Extremely Soft Cellular Hydrogels for Vascular Modelling

Author
Heidari, Hossein

Publication Date
2020

Peer reviewed|Thesis/dissertation

Fabrication of Extremely Soft Cellular Hydrogels for Vascular Modelling

By

Hossein Heidari

A dissertation submitted in partial satisfaction of the

requirements for the degree of

Doctor of Philosophy

in

Engineering – Mechanical Engineering

in the

Graduate Division

of the

University of California, Berkeley

Committee in charge:

Hayden Taylor, Chair
Dorian Liepmann
Michel Maharbiz

Spring 2020

Abstract

Fabrication of Extremely Soft Cellular Hydrogels for Vascular Modelling

By

Hossein Heidari

MS, University of California at Berkeley (2017)
BS, Sharif University of Technology (2015)

Submitted on May 27th in partial fulfillment of the requirements for the degree of
Doctor of Philosophy in Mechanical Engineering
at the University of California at Berkeley

In the past three decades, microtissue models grown inside miniaturized fluidic systems fabricated using soft lithography, were probably the most widespread form of engineered cellular structures. This conventional methodology has now been challenged by biofabrication techniques that offer shorter lead times and greater three-dimensional design freedom, while circumventing the manual alignment and inter-layer bonding challenges of soft lithography. As a result, attention has moved towards additive fabrication solutions.

Fused deposition modelling (FDM), inkjet, and stereolithographic projection-based 3D-printing solutions have demonstrated the possibility of printing master molds and sacrificial structures as well as encapsulated fluidic networks directly. As an example, we will briefly explore one such indirect fabrication strategy that we have developed for large area fabrication of multi-material soft structures (Multi-layered Micro-casting). Despite the simplicity and cost-efficiency of such indirect methods, an alternative direct bioprinting technique would overcome the geometrical limitations and enable better automation and process yield. However, direct printing in extremely soft hydrogels has its own diversity of challenges. These techniques typically require the use of support structures when printing overhanging features such as encapsulated fluidic networks. This support material is, in some cases, entirely impractical to remove from small-scale channels. Additionally, due to the material deformation during printing, most existing printing techniques are limited to materials that are orders of magnitude higher in elastic modulus than biological tissue.

In contrast, we introduce a new additive technique, computed axial lithography (CAL), which enables volumetric 3D-printing by illuminating a rotating volume of photosensitive material with a 3D light intensity map constructed from the angular superposition of many 2D projections. Oxygen inhibition-induced thresholding of the materials' dose response enhances patterning contrast. We report the application of CAL to fabricate structures in methacrylated gelatin with elastic moduli as low as 100 Pa, as well as stiffer acrylates. Uncured resin provides mechanical support during printing, eliminating the need for solid support. Among other advantages are print durations as low as a few minutes and the possibility to overprint gels on/in other structures.

Acknowledgements

I would like to start by saying how fortunate I've been in my entire life to have such wonderful family, friends and mentors. My parents Shahin and Janet have been a remarkable source of inspiration every second of my life for as long as I can remember. They've been reminding me time and time again how I shouldn't give up on seemingly large but actually very minor challenges in life, and how hard work and persistence are the main ingredients of success. For a lifelong dedication to getting me where I currently am, I would like to dedicate this thesis to them with lots of love. My lovely brother Reza, though ten years younger than me, has been a source of momentum and realism pumping energy and positivity into our family in my absence. I can't imagine how my parents would have survived this past five years without him.

I would like to dedicate my success and accomplishments in this tremendous journey since 2015 to the world's most dedicated supervisor who I love as much as a family member and a best friend, Hayden Taylor. He is not only the true definition of an expert scientist, and one of the most intelligent, innovative and hard-working scientists I've ever met indeed but more notably a true teacher that values ethics, sincerity and the professional development of his students more than anything else.

I am grateful to Dorian Liepmann, the chair of my qualifying exam committee and one of the loveliest and most genuine mentors I've ever had. I will forever remember the joyful experience of being a GSI for his microfluidics lab and learning from his endless experience in microfabrication and microfluidics and his unique teaching method. I would also like to thank the other members of my thesis committee: Michel Maharbiz, Liwei Lin and Mohammad Mofrad. They have all helped with perceptive questions and timely suggestions of new areas for investigation.

I am also grateful for the guidance and experience of Chris Spadaccini and Maxim Shusteff at the Lawrence Livermore National Lab, true experts in additive manufacturing. Also grateful for the many constructive discussions with other great collaborators and colleagues, particularly Robert Mcleod in the University of Colorado Boulder for his insight and expertise in photo-chemistry, Karen Dubbin in LLNL for her collaborative efforts in Bio-CAL, Joshua Speros, Dami Philips, Nate Wood and Herve Dietsch at BASF, Chris McCoy in You3Dit, Chris Parsell, Gary Gin and Aleta Martinez in the Jacobs Institute for Design Innovation, Scott McCormick, Jacob Gallego and Dennis Lee in the Mechanical Engineering Machine Shop, Alison Killilea and Carissa Tasto in the Cell Culture facility, Mary West in the High-throughput Screening Facility, and Paul Lum, Naima Azgui and AJ Gubser in the Berkeley Biomolecular Nanotechnology Center.

The Berkeley Fellowship committee put a great deal of faith in me when it funded my first two years here. So did the Anselmo Macchi Fellowship committee which I am also grateful for their support during my third year. I'm also grateful to BASF for their funding and support throughout the last two years.

My fellow students in the Design for Nanomanufacturing Research Group, Brett Kelly, Hannah Gramling, Brian Salazar, Joe Toombs, Nicole Luk, Alvin Chi Chung Lee, Kyle Soochan Chung and Kristyn Kadala have been a delight to work with. I've been fortunate to spend a ton of great time working on various exciting projects with them in the lab downstairs Etcheverry Hall. Outside the group, I particularly appreciate the fruitful interactions and help of Sofia Arevalo giving me extensive access to the nanoindentation system. Working with these fantastic individuals in such a collegial atmosphere has made for a very happy five years.

Biography

I started my academic career with a core interest in mechanical engineering as I was especially intrigued by the art of design, craftsmanship and ingenuity that goes into the nuts and bolts of every man-made product. It intrigued me that despite mankind's dream of perfectly mimicking nature, deep down we've always wanted to improve upon it, augment it, functionalize it, and utilize it in ways that it wasn't originally meant to be used. Soon I realized that there are many ways in which we can improve, augment and help restore the biological functionality or dysfunctionality of our own bodies. During the last two years of my undergraduate studies I came to realize the enormous and unique impact of modelling and manipulating material at the micro and nano scale. I became familiar with state-of-art design and manufacturing techniques that are now utilized in building new interfaces with the micro- and nano-biological world. I studied the permeability of the blood-brain barrier (BBB) cellular interface to drug coated nano-carriers and tried modelling the adhesive properties of graphene as a nano-filler in tissue scaffolds, both examples of how man-made systems and devices could interact with biological systems in our body. I received my B.S. degree in Mechanical Engineering from Sharif University of Technology in 2015.

I came to Berkeley that same year, having a computational biomechanics background image in my mind, and knowing all about the shortcomings of computational models, I decided to learn more about microfabrication and biofabrication. UC Berkeley was a perfect catalyst as I was not only able to spend numerous hours with one of the most clever, innovative and hard-working researchers and mentors I have known thus far, my supervisor Hayden Taylor, but also to learn from fabulous minds and visionary characters in our field such as Dorian Liepmann, Luke Lee, Ali Javey and Liwei Lin. In 2017, I received my M.S. degree in Mechanical Engineering from UC Berkeley and continued my research on modelling vascular interfaces *in vitro*. The focus of my M.S. and Ph.D. work, as I will thoroughly explain in this thesis, has been to discover biofabrication and bioprinting technologies that could be utilized to produce cell-embedded tissue constructs made of extremely soft biomaterials.

In the course of this past five years and with the endless support and advisory of Prof Hayden Taylor, I've been fortunate to receive multiple national and international awards for my M.S. and Ph.D. research: I received the $100K BASF Shark Tank Prize in 2018, the SPIE Start-up Challenge Award in 2019, the Anselmo Macchi fellowship in 2018, the CHEMINAS Young Researcher Award at microTAS 2017 and the Berkeley Fellowship from 2015 to 2017.

SPIE Photonics
startup challenge
2019

From leaders of the photonics industry

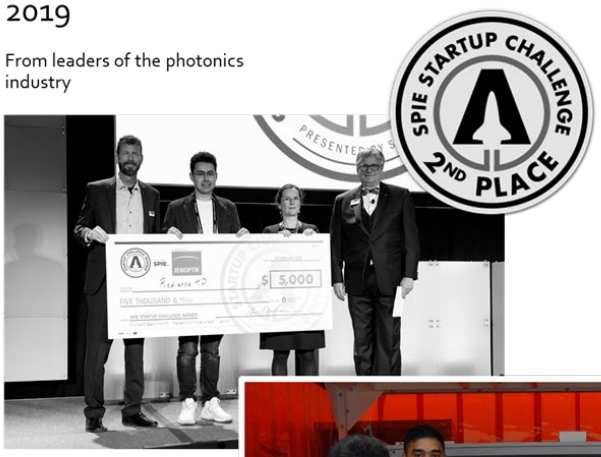

BASF Innovent
Shark tank
2018

From leaders of the chemicals industry

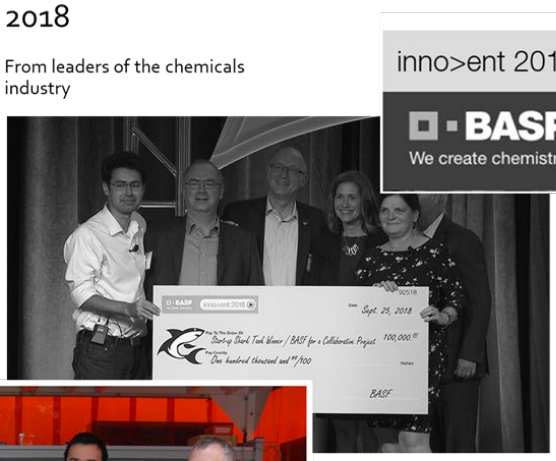

Celebrating the publication of our work in Science, and the great excitement it had triggered, one of the happiest moments for the entire CAL team.
Left to right: myself, Indrasen Bhattacharya, Hayden Taylor, Maxim Shusteff, Brett Kelly, and Christopher Spadaccini

Contents

Table of Figures

Chapter 1

Introduction

In this introductory chapter, we will first take a moment to glance at the problem definition. What's the motivation for producing extremely soft and compliant structures? How would we define *'extremely soft'* in the biological realm? Which organs do we target and what sub-architectures require this level of delicacy and compliance? And ultimately, what are the fabrication challenges and complications associated with soft materials that we need to overcome? In order to understand what differentiates the processes introduced in the present work, we will briefly explore the different classes of biofabrication techniques that have been targeting this very challenge with innovative manufacturing strategies in the past two decades.

1.1. Biological significance of soft biomaterials

The very first question to ask is '*why is there a need to fabricate soft in vitro tissue models?*'. Perhaps the more fundamental question is '*why is there a need for in vitro tissue models at all?*'. Replicating human tissue *in vitro* is not only vital for understanding and conquering human diseases and examining the efficacy of therapeutic solutions, but also in replacing and augmenting *in vivo* tissue. The latter is exactly where the throughput and other fundamental capabilities of the conventional approaches are challenged. Despite the enormous advancements that have been made in the fabrication of small and on-chip *in vitro* tissues with conventional microfabrication techniques, we would need to ultimately find a way to deliver the same physiological realism at larger tissue scales. Microfluidic platforms allow one to hold and constrain the extremely compliant gels inside relatively rigid chambers and micro-channels. This inherent feature that comes at the cost of compromising some physiological signatures of native tissue, eliminates the need to deal with the challenges of soft and deformable structures. However, to produce tissue volumes any larger than a few microliters, these platforms will no longer be of any use. This has been a motivation for tissue engineers to invent clever fabrication solutions and adapt

the techniques used for other classes of engineering polymers to produce large-scale *in vitro* tissue models.

The choice of a manufacturing platform heavily depends on the mechanical properties of the material that you're trying to shape. Hence comes the important and critical consideration associated with the elastic moduli and stiffness of the biomaterial. As a matter of fact, this is also of great importance in the biological realm. In the macroscopic scale of the human body, in the smaller scale of an organ or even an organoid, and even smaller than that in the scale of a microscopic arteriole and venule, we have gradients and variations of mechanical properties. All the way from the thick viscoelastic blood that shears the thin and elastic endothelium to the more sturdy layer of smooth muscle cells, we have a multiplexed unit that could be again surrounded by tissue structures as compliant as the brain with only a few hundred pascals of stiffness or the much stiffer cartilage tissue with stiffnesses in the range of a few megapascals. Every domain of this broad range of mechanical properties, introduces its own engineering challenges. To replicate our bone and cartilage units, we need to engineer highly porous biomaterials that are capable of withstanding impact and severe fatigue and cyclic loading while the eye tissue requires an extremely intricate and precise architecture and an astonishing positioning and alignment accuracy that can only be enabled by very fine elastic bundles of cellular fibers.

Here, we direct our focus to extremely soft tissues in the range of only 100–5000 pascals. To have an intuitive sense of how compliant a few hundred pascals is, you can think of the compliance of a marshmallow; the structures we are trying to fabricate are ten to a hundred times softer than a typical marshmallow. A good example of such tissue is the highly vascularized brain tissue. As one of the most complicated organs in our body, the brain's tissue is also among the most compliant of tissues, and its mechanical characteristics are spatially heterogeneous, nonlinear, time-dependent, and directional. They are also challenging to measure, with reported values varying over at least an order of magnitude depending on, e.g., the loading method used and the age of the tissue [1]. For example, Prange and Margulies [2] modelled the instantaneous (pre-relaxation) shear modulus, G, of various in vitro samples of dead human and porcine brain tissue to be in the range 130–530 Pa. Taking the tissue to be incompressible for short deformation time-scales, this result corresponds to Young's modulus, E, of 390–1590 Pa ($E = 2G(1 + \nu)$ and $\nu = 0.5$). Later work by Gefen and Margulies, however, found that the short-term shear modulus of unconditioned (i.e., previously undeformed), living porcine brain was on average 1875 Pa, corresponding to E = 5.6 kPa when incompressibility is assumed [1]. More recently, Budday et al. used nanoindentation to determine bovine white matter to have a Young's modulus of 1.895±0.592 kPa and gray matter a modulus of 1.389±0.289 kPa [3]. Recent measurements of dead human brain tissue also show a strong dependence on location in the brain, with, e.g., shear moduli extracted from simple shear measurements varying from 0.33±0.18 kPa in the corpus callosum to 1.06±0.36 kPa in the cortex [4]. Assuming incompressibility, these measurements imply Young's moduli of 0.99±0.54 kPa and 3.18±1.08 kPa respectively.

While the mechanical properties of brain tissue are a topic of extensive ongoing research, and realistic models need to be able to replicate cerebral mechanical characteristics, the brain tissue like any other organ in our body also hosts an extremely high density of vascular networks.

Vascular networks are probably the finest architectural element and feature repeated in almost all organs and tissue sites. A complete synthetic human organ will thus require the production of complex, branched vessel networks covering volumes of many cubic centimeters and spanning from the arterial (~1 cm) to capillary (≲100 μm) scales. All applications of tissue engineering (with the exception of cartilage tissue) call for vasculature in some form [5]. The need for drug screening platforms that go beyond a simple assay and can replicate the tissue-specific biological response is one of the primary therapeutic applications for *in vitro* vasculature. The human vasculature is also one of the most important systems involved in the progression of almost all diseases and fundamental disease studies require *in vitro* disease models that replicate the geometrical complexity as well as the multitude of vasculature-specific cell types [6]. Additionally, an enormous opportunity and challenge lies in the in vitro growth of meat for food, which may have the potential to cut greenhouse gas emissions vastly compared to conventional agriculture, to reshape land use, and to address antibiotic resistance [7]. Nascent meat-growing efforts, however, have been hampered by the lack of a vasculature synthesis technique scalable to hundreds of grams of tissue and the centimeter thicknesses needed [8].

Therefore, blood vessels represent a perfect benchmark for a biofabrication process. Not only are they amongst the finest features but also a necessary element for every tissue model. As mentioned, there has been significant progress in the recent years in producing perfusable blood vessels inside microfluidic systems. There remains a need, however, to create functional networks reliably in much larger-volume systems and realistic yet scalable methods of culturing three-dimensional vasculature *in vitro* are among the greatest current challenges facing tissue engineering. In the next two sections we will take a look at the specific challenges of manufacturing soft tissue components as we explore the current landscape of biofabrication techniques and evaluate the strengths and weaknesses of each method.

1.2. Biofabrication technologies: a highway from organ-on-chip models to organ-on-human prototypes

Tissue engineering had already evolved quite significantly in the past few decades, especially with the advent of a set of very powerful tools including a rich library of natural as well as synthetic biopolymers and hydrogels that enable 3D encapsulation of most available cell types, 2D nano-patterning techniques and microfluidic platforms enabling accurate parallelized sample preparation and handling. These are a few of the main game-changing technologies that have enabled great advances in translational medicine for in-vitro disease models and organs-on-chips. However, despite all these advancements, one could still spot a relatively large gap between small ‘on-chip’ models and large ‘transplantable’ ones. In other words, there was always a need for a technological equivalent to the large volume molding, subtractive and additive manufacturing technologies available for plastics, metals and ceramics in the biomaterial realm.

Along with the introduction of more sophisticated and flexible biofabrication techniques, the ability of the fabricated prototypes to mimic the native tissue became a key differentiating factor.

Bio-printed tissue constructs often lacked biological functionality and performance, and microfluidic and on-chip models, however accurate, were not easily scalable to the dimensions of a transplantable organ. Hence, when it came to the production of dense volumetric samples of tissue, thicknesses even on the millimeter scale were far from reach, as was observed in the efforts of many research groups. An example of such work was the aforementioned idea of lab grown meat, where some groups were hardly able to produce a centimeter-thick burger with almost 20,000 millimetric strands of muscle cell bundles [8]. Two very important characteristics of most vital organs became appreciated more than ever. The fate of a group of cells forming a piece of tissue heavily depends on the transport of species in that domain, the external stiffness gradients, and the ability of cells to proliferate, differentiate and migrate in response to these two external stimuli. Hence, the two characteristics were the ability to modulate the mechanical properties of the gel and to achieve stiffness values as low as the native tissue, and to be able to mimic the transport interface i.e. the vascular networks that span that piece of tissue.

Evidently, the degree of physiological realism needed in cultured vasculature can be expected to depend on whether the application is scientific, medical, or agricultural. For example, requirements for realistic endothelial permeability are likely to be looser for cultured meat than for drug-screening models. The same holds for gel stiffness; depending on the kind of tissue that we're trying to mimic, the complications and challenges associated with the stiffness and deformation of the matrix could vary significantly. As mentioned before, for the purposes of this study we will be focusing on soft vascularized tissue. Therefore, our attention is naturally drawn towards techniques that are targeting soft vascular tissue models.

Several common ingredients of successful vasculature growth can, however, be identified. Firstly, the mechanical properties of the extra-cellular matrix (ECM) need to be representative of tissue, with elastic moduli typically ranging from 1–100 kPa [9]. Secondly, the ECM needs to contain the requisite adhesive protein sequences to promote cell spreading and needs to allow remodeling as cellular structures emerge. Thirdly, whether vessels are defined 'top-down' in pre-determined geometries or allowed to emerge naturally in 3D culture, confluent monolayers of endothelial cells are needed with inter-cellular junctions that offer sufficiently realistic molecular permeability. Hydrodynamic shear stresses on the order of 1 Pa exerted on the internal walls of the endothelia by blood flow are known to drive tight endothelial junction formation [10], and a realistic in vitro vasculature model is likely to need to mimic these stresses. This shear stress value can vary quite significantly across different vascular interfaces depending on the physiological flow rates experienced at that level and the physical size of the lumen. Evidently, with lumens ranging all the way from tens of microns to tens of millimeters and different tissue sites requiring different circulation rates, shear stress values can vary quite significantly. In vitro models usually target physiologic shear stresses ranging from 100 to 1000 mPa corresponding to a blood flow rate of 100-200 µl/min that is typical of larger capillaries and small arterioles. In the next section we will look at the state-of-art in vascular tissue fabrication techniques.

1.3. State of the art biofabrication techniques, capabilities and limitations

Before we start our classification of different biofabrication techniques, and in order to avoid further confusion, it is worth defining some terms. The term biofabrication is usually defined as the production of living and non-living biological products from raw materials such as living cells, molecules, extracellular matrices, and biomaterials. While the biological products can include drug delivery systems, antibody test kits, biodegradable stents etc. – here we are only looking at a sub-category of such production techniques – were the product is an *in vitro* living tissue model. Bioprinting is also usually defined as the use of additive manufacturing technologies with materials that incorporate viable living cells etc., to produce tissue, and is therefore these techniques are a subcategory of the broader biofabrication library of manufacturing methods.

As previously mentioned, bioprinting techniques emerged as a solution to scale-up and expand the capabilities and complexities of available microscopic models of tissue. We will start our analysis and classification with some very simple biofabrication technologies. One could even consider the soft lithography process used to fabricate a microfluidic chip as an early biofabrication technique. Earlier engineered tissue models attempted to solve the *in vitro* modelling needs with the use of simple microscopic channels and chambers that were a common feature of all microfluidic designs. In order to enhance the capabilities of such simple chips, several clever tweaks were made. An interesting approach that soon became common in various microfluidic co-culture models as well as epithelial and endothelial models was to use a porous 2D membrane as an interface that would host multiple cell types on either side [11] [6]. This membrane system would allow the researchers to capture the cell-specificity of these biological interfaces and perform most transport related studies while being extremely easy to use and convenient. Another clever approach following the same lines of thought and falling in the same category of 2D interfaces were diffusion chambers injected with extra-cellular matrix (ECM) that could separate multiple culture compartments [12] [13] [14]. Such models would rely on the diffusion of biomolecules, growth factors and other agents through the gel interface. Although these channels enable diffusion of cell-secreted factors and chemicals, they suppressed important signaling pathways such as intercellular mechano-transduction and direct cell-cell signaling because neighboring cell types were kept isolated [15].

The use of hydrogels in conjunction with microfluidic systems brought many additional innovative features to the conventional chips. As an example, a technique called ‘viscous finger patterning’ was introduced that utilized capillary flow through a gel-filled channel to produce a hollow cylindrical vessel surrounded uniformly by the gel [16] [17]. This would eliminate one of the most important flaws of all microfluidic models which was exposing endothelia to materials that were far stiffer than that encountered in the body. The elastomeric poly-dimethyl-siloxane (PDMS) surfaces of these microfluidic chips were 100–1000 times stiffer than typical ECM, and the polystyrene trans-well membranes that we mentioned earlier were around 10^6 times higher in elastic modulus.

Despite the numerous improvements made to the classic microfluidic chips, these models were still heavily geometrically constrained. The co-culture complexities and morphologies needed to mimic *in vivo* tissue were far from reach, and the tissue volumes that could be modeled were limited to a few microliters. There was clearly a need to scale up the process and break the barriers of microfluidic systems.

Although the golden age of soft lithography seemed to be over and the method had reached its technological limits for tissue modelling, the idea of molding and pattern transfer was still on the table and was in fact the dominant approach for engineering polymers. Hence, the idea was adopted for biological polymers as well. Perhaps the simplest molding technique that was used was the needle removal method. In this process, a hydrogel was cast around a cylindrical needle, and after removing the needle a channel remained on the surfaces of which an endothelium could be cultured to simulate a blood vessel [18]. A geometrically generalized version of this method was introduced later that used a thermally gelling, aqueous material such as F127 from the Pluronic family as the sacrificial structure [19]. The key rate-limiter in such processes tended to be the liquefaction or dissolution and subsequent removal of the sacrificial material. Another key limitation with the sacrificial casting technique was that it did not in itself enable multi-material structures; yet such complexity was very essential to almost all realistic tissue models. In other words it suffers from the same complications associated with seeding multiple cell types and producing multiple concentric shells and layers, since we are only able to remove the sacrificial core once.

The novelty of the multi-layered micro-casting technique that we will introduce in this thesis addresses this exact flaw of this class of indirect biofabrication techniques. By utilizing a customized 3D-printed mold design and multiple casting steps, it allows the user to define many layers of hydrogel material within the same build. Hence, it will enable patterning of multiple matrix compositions and cell types in different localized regions of the fabricated construct. Despite these enhancements, the same geometrical limitations and constraints of casting that exist for engineering polymers still exist for these biofabrication equivalents. The molds need to be removable, and the structures cannot easily extend beyond the casting planes. Lack of design freedom and the necessity of customized tooling and fixturing calls for the advent of direct biofabrication solutions.

Additive manufacturing technologies have been around for many decades and are among the few alternatives that enable repeatable production of almost any arbitrary geometry with very little effort in customized and labor-intensive process preparation. The most widespread technique that could apply to almost any thermoplastic polymer is fused deposition modelling (FDM) or extrusion-based additive manufacturing. The simplicity and convenience of this technique as well as the suitability of an extrusion scheme for most of the water-based hydrogel precursors has put it in the forefront of early efforts and an immediate first candidate for bioprinting. In accordance with this subset of bioprinters, the term bio-ink was coined to demonstrate the extrusion and jetting of the fluid precursor through a nozzle.

The first approach pertaining to this class of nozzle-based processes is to culture cells inside sub-mm-diameter “tissue spheroids” and then deposit these spheroids as the building blocks of larger-

scale structures [20] [21]. The larger three-dimensional tissue structures are thus formed through the post-printing fusion of the deposited bio-ink particles. This is very similar to the inkjet technology that has been widely adopted for use with engineering resins and polymers. However, most of the research modules and commercialized versions of these bioprinters only use a single nozzle for deposition in contrast with the engineering resin equivalents that typically use an array of more than ten nozzles to increase throughput. Hence, the available examples of this process have an inherently slow print speed as the droplets have to be deposited one droplet at a time.

An alternative approach is to extrude a continuous filament of hydrogel precursor or bio-ink through the nozzle. There are also various sub-categories for this approach. For instance, with respect to the gelation modality of the bio-inks, some processes extrude a liquid precursor which is thermally solidified upon deposition on a cooled bed, some utilize an exposure system to photo-crosslink the deposited material [22] [23] and some deposit the material into a controlled pH environment and utilize an ion-transfer reaction to crosslink the precursor [24] [25]. You can also classify these processes based on the nozzle configurations. One approach is to use multiple nozzles to extrude sacrificial material as well as the main bio-inks, and then use the hollow spaces emerging upon the dissolution of the sacrificial material as a perfusable network [26]. Another clever approach to integrate the vascular networks into the printed structures is to use a single nozzle with a coaxial extrusion mechanism that utilizes a sheath flow and core flow that may contain multiple agents. The use of a central core flow that does not crosslink accompanied with a coaxial surrounding flow that does crosslink allows one to directly print hollow cylindrical tubes of hydrogel [27] whose crosslinking may be triggered either by light or a pH change.

In both approaches, cells may be suspended in the ink and by using multiple ink channels, heterogeneous cellular structures can be defined rather easily. Resolutions down to ~100 μm have so far been demonstrated with these nozzle-based techniques [28]. However, a very important consideration for such processes is that as you reduce the nozzle diameter to achieve better resolution and layer thickness, the volumetric deposition rate will also be reduced significantly and hence the print speed will suffer drastically.

Another innovation that enhanced the capabilities of extrusion-based processes was the idea of printing into a block of sacrificial gel. One can imagine that in cases where hollow or delicate structures are to be printed, mechanical support must usually be provided. A promising approach to meet this need is “freeform embedding of hydrogels within a sacrificial gel” (FRESH), where a long extrusion needle draws out the required cellular structure within a volume of soft, thixotropic supporting gel [29] [30]. However, in terms of resolution, FRESH faces the same constraints as any other extrusion technique. In other words, the minimum feature size that defines the thickness of the vascular wall is limited to the diameter of the extruded material. The process also suffers from the same slow print speeds and low throughput issues that all other extrusion-based technologies are also facing.

While droplet dispersion and extrusion of UV-crosslinkable bio-inks with inkjet and extrusion technologies has seen extensive use, as zero-dimensional printing processes they suffers from extremely slow print speeds and not so good print resolution that keep even the most over-

engineered versions of these printers up for debate for many real-life applications in the future. Maximum print speeds of only a few hundred microliters a minute, mean that printing an average-sized organ would take a couple of days of continuous printing.

However, photo-crosslink-able bio-inks offer much more than just an additional crosslinking network. The ability to selectively pattern these materials with light has given rise to some very powerful bioprinting technologies including the method that we have invented and will present in the next chapter. Using many of the same compositions and photo-activated chemistries and a simple source for patterned illumination, photolithographic approaches have been able to enhance both print speed and quality [31] [32]. Most of these lithographic approaches utilize a DLP projector with a digital micromirror display (DMD) chip to project the desired two-dimensional patterns on a thin layer of photosensitive bio-ink [33]. The part being printed is produced from the stacking of many thin layers that are each cured and formed upon exposure to the mentioned light pattern. In some cases the part is inverted and withdrawn from the vat of hydrogel precursor and the source of illumination is positioned underneath a transparent window [34] whereas in another configuration, the vat of resin is placed under the illumination source, and the stage containing the part is gradually lowered [35].

In order to limit the penetration depth of the light so that only a single layer of material is affected by the projected pattern, absorptive dyes such as food coloring are used in the bio-ink mixture's composition [34]. Furthermore, to achieve continuous printing, and eliminate the sequential stepping motion that is necessary to avoid adherence to the transparent window, the material used in the window has been modified to polydimethylsiloxane (PDMS) which is permeable to oxygen. The oxygen-rich layer adjacent to the window inhibits photo-polymerization in that so-called 'dead-zone' thus preventing adhesion to the window [36].

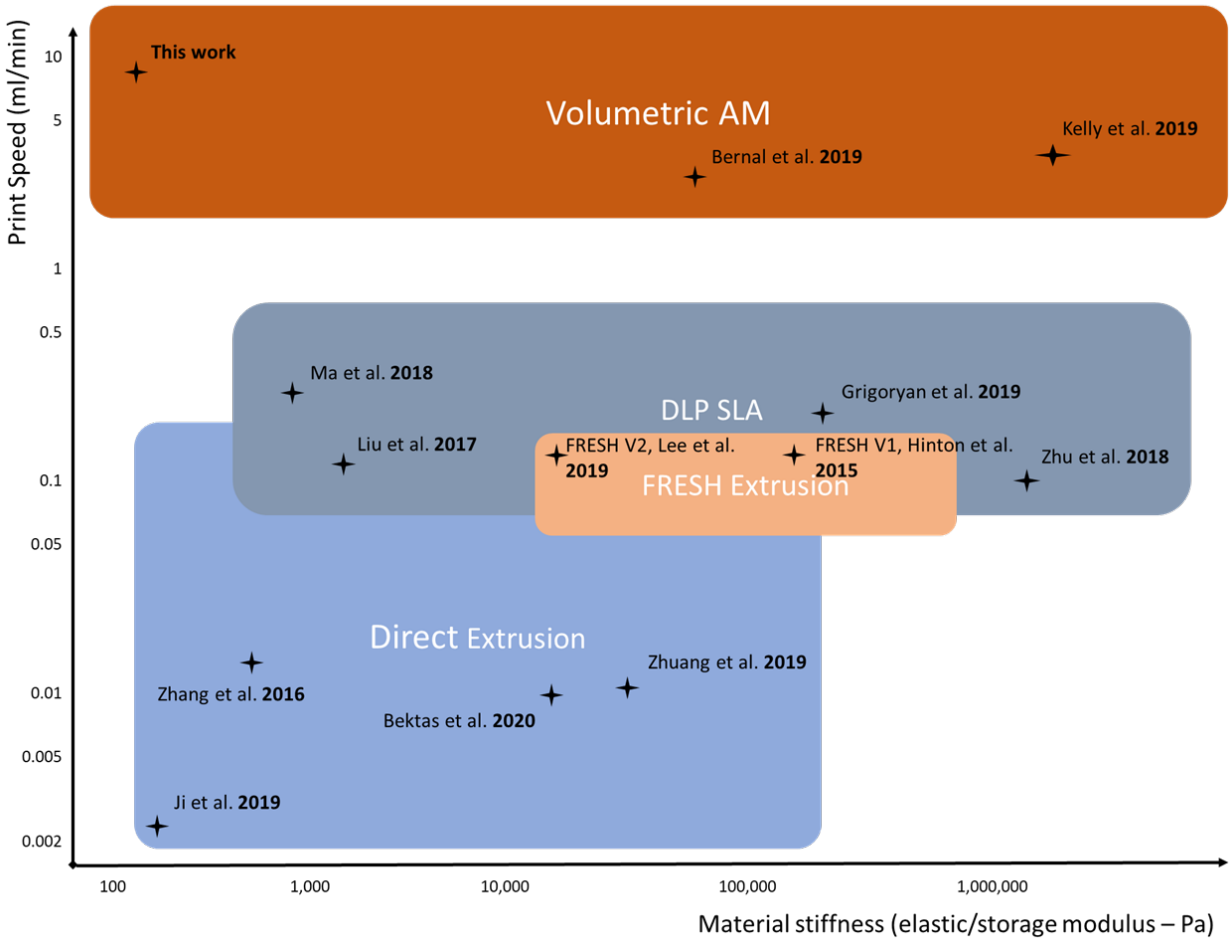

Figure 1 The current landscape of additive biofabrication technologies with respect to two critical parameters: throughput and matrix compliance.

An alternative strategy to embedding the structure in support material is to eliminate the use of supports altogether through volumetric variants of optical lithography [37]. The idea here is to print the entire volume of an object all at once instead of one layer at a time. Although such techniques have only been introduced recently, as we will discuss in detail, they can hold great promise for support-free 3D printing of soft materials. The volumetric and *contact-free* nature of the tomographic additive manufacturing process that we will introduce in this thesis also allows for many other improvements to the conventional bioprinting processes. For example, the use of thermal gelation prior to printing provides a thixotropic environment that holds the printed features perfectly intact throughout the process and can be easily removed by heating the gel to incubator temperatures. Constructs can be printed over other objects allowing for integration of connectors, inlet and outlet ports etc. with the printed tissue for perfusion and incubation purposes. The volumetric bioprinting technology introduced here surpasses the throughput and speed of other processes by one to two orders of magnitude while allowing us to print in material in the sub kilopascal range (Figure 1).

Before moving to the next section, there is an alternative technique to produce vascular networks that uses a bottom-up approach. This approach is inspired by vasculogenesis and angiogenesis and involves the natural growth of endothelial sprouts within a 3D hydrogel matrix. Microvascular networks-on-a-chip fall in this category, and many groups have successfully produced perfusable endothelialized sprouts that extend within a microfluidic gel chamber [14] [38] [39] [40]. This method offers an organic vascular growth model and extremely fine capillary networks. Although this approach has been in large been adopted by microfluidic models of tissue, the combination of this bottom-up approach with the top-down biofabrication techniques reviewed in this section seems to be the ultimate solution for large scale organ models.

Otherwise, the use of such microscopic capillary network models in solitude poses many functional and geometrical limitations when modelling tissue. For example, single layered lumens with only one cell type can be produced and it is impossible to produce a secondary lumen of cells surrounding those sprouts, and in the best case a second cell type can be added by embedding cells within the surrounding ECM. Furthermore, the range of lumen diameters that are achievable with such organic growth models is limited to micro-capillaries, and without integration with a synthetic macroscopic network that spans the artery and arteriole length-scales, such models can hardly be engineered.

1.4. Selecting a suitable biomaterial candidate

Another important consideration to have in mind when selecting the ideal biofabrication process for our application is the flexibility of the process with respect to the choice of material, as well as the range of properties that could be achieved with the physics of the process in hand. The choice of a biomaterial can depend on many different variables. The type of tissue that we're trying to model with respect to the cell type and density as well as its compliance, whether we expect the matrix to gradually degrade, and the geometrical complexity of the target architecture are a couple of factors that influence the decision. The first and last on this list which are mostly entangled with the achievable elastic modulus of the printed gel are heavily dependent on the crosslinking mechanism and the hydrogel chemistry. The second property has to do with the biological structure of the macromolecule and whether it possesses digestible sequences and domains that would enable biodegradation. As we shall briefly study, this problem could also be potentially addressed via functionalization and synthetic enhancements to the monomer structure. Let's briefly study a couple of different candidate biomaterials with respect to the abovementioned characteristics.

Poly (ethylene glycol) diacrylate (PEG-DA) is among the most frequently used photo-crosslink-able synthetic polymers. One of the main reasons for such broad acceptance of PEG-DA is the wide range of elastic moduli that could be achieved with different molecular-weight variants of this polymer or just by simply varying the polymer content of PEG-DA in the hydrogel precursors. Evidently the biocompatibility and abundance of this polymer are among the other reasons although its lack of adhesion domains has proven to be problematic. This is typically addressed with the integration of the adhesive tetrapeptide RGDS (Arg-Gly-Asp-Ser) in the polymer chain

[41] [42]. The degradation of polymers and hydrogels is a different challenge which can also be addressed with some of the same chemical tweaks. For instance, PEG-DA hydrogels are susceptible to slow degradation *in vivo* and are therefore unsuitable for use in the production of long-term implants. This degradation is shown to be due to hydrolysis of end-group acrylate esters [43]. To enhance and tune the degradation of PEG-DA based polymers and hydrogels, functionalization with dithiothreitol (DTT) has been proposed and examined [44].

Another example of such widely adopted photo-crosslink-able monomers is gelatin methacrylate (Gel-MA). The exceptional inherent biological properties and tunable physical characteristics of Gel-MA have made it an ideal candidate for modelling soft tissue. Gel-MA already possesses the cell-adhesive domains and degradation characteristics and therefore doesn't require additional functionalization procedures [45]. The main limitation with Gel-MA is the difficulty of achieving high resolutions and feature sizes with pure Gel-MA. Hence, many have proceeded to use Gel-MA in combination with PEG-DA to achieve higher print fidelity as well as better mechanical and structural performance [46]. It is worth noting that Gel-MA and gelatin in general can also be used as a thermally crosslinking component in a bio-ink blend. This is a property of Gel-MA that we will extensively utilize in computed axial lithography.

Alginate-based hydrogels that are typically crosslinked upon reaction with calcium chloride are another good example of natural matrices. Despite the challenges of controlled transport and fluidic mixing that makes such chemical crosslinking processes more constrained than flexible, biofabrication techniques such as inkjet printing and extrusion are able to utilize these hydrogels by including the reactive species either in the coaxial nozzle core/sheath flow or in the build vat [47]. Apart from this process design concern, these hydrogels offer a great candidate for low stiffness tissue models [48] and hollow tube extrusion [49]. Alginate is also frequently used in along with other components of composite hydrogels or bio-ink blends to enable multi-parameter control of matrix stiffness and degradation [50] [51].

Collagen and collagen methacrylate are also great natural biopolymers. Collagen has previously been extensively used with microfluidic devices serving either as a gel [52] [53] or just a thin coating [54]. It has also gained lots of interest in the bioprinting and biofabrication community. The easiest method to fabricate structures out of collagen-based hydrogels is either simple extrusion [55] or FRESH [30]. It benefits from all the positive attributes of gelatin while having a slightly richer structure. Despite the availability of functionalized photo-crosslink-able collagen, combining pure collagen with Gel-MA has also shown promising results in promoting angiogenesis within the printed gels [56]. Here, we have used collagen in combination with agarose to deliver the crucial biological properties to our composite hydrogels.

Agarose has also been used as a thermally crosslinking natural hydrogel matrix with an interesting structural robustness originating from the hysteresis behavior of its gelation process which we will further discuss in the next three chapters. The issues associated with agarose are very similar to those previously mentioned for PEG-DA, lack of cell-adhesive domains and a digestible backbone. The solutions incorporated to overcome these limitations are also quite similar. Here, we have used

agarose in combination with collagen, however, other groups have demonstrated promising results combining agarose with Matrigel [57] and alginate [58].

Hyaluronic acid (HA) and HA-methacrylate represent another biologically rich candidate hydrogel precursor that is widely used in biomedical applications due to their excellent biocompatibility. They are also typically mixed and dual-crosslinked with another component being Gel-MA or PEG-DA in order for these monomers to benefit from the crucial biological advantages of HA [59] [60].

1.5. The structure of this thesis

Hopefully this introductory chapter has assisted the reader in obtaining a clear image of the current landscape of biofabrication technologies, clever innovations and improvements made to existing techniques, and the main advantages that each approach offers as well as their inherent constraints.

While indirect biofabrication methods such as molding are considered geometrically constrained, their convenience and simplicity as well as their repeatability and reasonable resolution makes them a perfect candidate for drug-screening and disease modelling platforms and assays. The biological relevance of the structures fabricated with these indirect methods is what we seek to enhance with multi-layered micro-casting.

Direct biofabrication methods also referred to as bioprinting techniques offer greater design freedom, automation and parallelization. However, the layer by layer deposition that all these processes have in common, limits their speed and throughput, necessitates the use of support and most importantly constrains the lower bound of achievable hydrogel stiffnesses. These limitations are what we seek to overcome with computed axial lithography.

In **Chapter 2** we will describe the details associated with the cell and tissue culture procedures, preparation of the cell-laden biomaterials and coatings, and customized fixtures and tools. We will also provide the reader with the tools, kits and protocols used to characterize the fabricated structures for their biological and mechanical performance.

In **Chapter 3** we will explain the methodology used in each of the two proposed biofabrication techniques, the details and considerations associated with each step of the process, the components, equipment and system setups and experimental configurations. We will demonstrate the specific advantages and unique capabilities of each process through experimentation.

In **Chapter 4** we will look at the outcomes of each process by evaluating the experimental results obtained after the tissue models have been fabricated, cultured and come to confluence. Various characterization schemes will be introduced, and the biological merits of the fabricated constructs will be measured against these metrics.

Chapter 2

Biomaterials, tissue culture, and characterization

In this chapter we shall introduce the various biomaterial compositions used throughout the study, the strengths and weaknesses of each component from a biological and mechanical point of view, and customizations and tweaks made to these tailored extracellular matrices. We will also look at the different human cell lines that were cultured in these fabricated microenvironments as well as the growth factors and supplements used to enhance the tissue culture procedure. Finally, we will review the characterization tools and procedures utilized to evaluate the mechanical and biological performance of the constructs produced in each experiment. These tools will ultimately determine the effectiveness of each of the chosen biomaterial candidates and biofabrication methods in producing biologically relevant tissue models and replicas.

2.1. Preparation of the hydrogel extracellular matrices

In the course of this study and for each of the two biofabrication techniques presented here, a variety of candidate biomaterial compositions were chosen and evaluated. The two main gelation modalities utilized in both processes are thermal and photo-polymerization. Composites of agarose and collagen were used alongside a couple of different thin coatings such as poly-D-lysine, collagen and fibronectin for the multi-layered micro-casting process while composites of gelatin methacrylate and polyethylene glycol di-acrylate were used for the volumetric bioprinting process. The three natural biopolymers (agarose, collagen and gelatin) represent ECM components and carry sequences that are present in native tissue and have therefore become very popular in the tissue engineering community. Polyethylene glycol also represents a great candidate photopolymer due to its biocompatibility and the wide range of mechanical properties that it offers. The ability to mix and match multiple components of the choices mentioned above, provides us with more freedom to modulate multiple biological and mechanical characteristics to our desired values.

For the multi-layered micro-casting process, we needed a composite that would not only offer great biological performance but one that would also retain its integrity and shape after the casting

process is completed. Agarose is a thermosensitive natural polysaccharide that consists of copolymers of 1,4-linked 3,6-anhydro-α-L-galactose and 1,3-linked β-galactose [61]. Since the gelation mechanism of agarose is through hydrogen bonding and chain entanglement, the gelation temperature can be configured for the desired application between 17 °C and 40 °C, by tuning the degree of hydroxylethyl substitution. The melting temperature of agarose, meanwhile, is as much as ~40 °C greater than the gelation temperature, displaying a useful hysteresis behavior which we will incorporated in the multi-layered micro-casting process. As we will demonstrate in the fourth chapter, agarose-based hydrogels show exceptional mechanical performance, and can be used to cast sub-millimeter geometries even at very low polymeric concentrations (1% w/v and lower) and elastic moduli (1–10 kPa and less). Pure agarose, however, lacks cell-adhesive domains, resulting in poor cell viability and adhesion in long-term cultures. One way of resolving this biocompatibility issue is by immobilizing adhesion ligands on the crosslinked chains through the activation of hydroxyl groups [62]. An alternative way is the use of binary composites of agarose and other natural biopolymers and ECM proteins [15]. The latter solution offers more degrees of freedom and multi-parameter tunability, via the independent modulation of each component of the hydrogel.

Here, we've studied a wide range of binary agarose–collagen (AC) hydrogels with varying agarose and collagen concentrations (0.25–3.0% w/v and 0–0.2% w/v respectively). We have evaluated them for their mechanical performance, manufacturability and biocompatibility in both 2D (endothelial) and 3D culture. High-melting-point agarose (J.T. Baker, Center Valley, PA, USA) with a gelation temperature of 36 °C was dissolved in sterile Dulbecco's Phosphate Buffered Saline (DPBS, Gibco, Rockville, MD, USA), filter-sterilized, and kept at 40 °C before mixing with type 1 rat-tail collagen (Corning, Corning, NY, USA; supplied at 3–4 mg/mL in 0.02 N acetic acid) that had been diluted in media containing cells as required.

For the purpose of the volumetric bioprinting approach using computed axial lithography (CAL), we either used pure gelatin methacrylate or a composite of gelatin methacrylate and polyethylene glycol di-acrylate as our hydrogel matrix. The Gel-MA in lyophilized format (Cellink, Boston, MA, USA) was dissolved in sterile Dulbecco's Phosphate Buffered Saline (DPBS, Gibco, Rockville, MD, USA) at 42 °C, mixed with a diluted version of poly(ethylene glycol) diacrylate (average M_n 700, Sigma-Aldrich, St. Louis, MO, USA), filter-sterilized, and kept at 40 °C before mixing with the cells. The photo-initiator Lithium phenyl-2,4,6-trimethylbenzoylphosphinate (LAP, Cellink, Boston, MA, USA) was used at a concentration of 0.1–0.2% w/v of the solution. The photo-initiator was slowly mixed with the solution at 42 °C just before the sterilization step. In all experiments, the cell-embedded mixture was refrigerated and thermally gelled at 4 °C. There are two important considerations associated with this step of the process. Firstly, due the difference of oxygen solubility limits at different temperatures the sample should either be cooled down very briefly (just enough for gelation to occur) or should be given ample time for the oxygen diffusion profile to develop a steady state oxygen concentration across the vial. Secondly, when cells are present the mixture should be gently displaced at intervals during the cooling process so that the cells do not collect at the bottom of the vial. For more complex printed geometries, a blend resin

was created using poly (ethylene glycol) diacrylate at 7.5% (v/v) and gelatin methacrylate at a final concentration of 5% (w/v).

2.2. Hydrogel surface coatings

In obtaining an endothelial lumen, the cell adhesion properties of the hydrogel surfaces play a central role. Unlike many hydrogels, such as collagen, gelatin, and methacrylates of polyethylene glycol, gelatin and hyaluronic acid, whose surface adhesion properties have been studied intensively, agarose hydrogels have not been explored as much. We therefore conducted a study of various surface coatings that would enable cell adhesion and spreading on agarose surfaces. The main surface coatings studied were poly-d-lysine (PDL), Matrigel, collagen, and human-derived fibronectin (hFN). The following protocols were used:

PDL hydrobromide powder (Sigma-Aldrich, St. Louis, MO, USA) was dissolved in sterile DPBS to a concentration of 0.1 mg/mL and this stock solution was then diluted over a range of concentrations (0.01–0.25 mg/mL) in order to find the optimal coating concentration. The hydrogel substrates were covered with 250 μL/cm^2 of the diluted PDL solutions. The samples were incubated at 37 °C and 5% CO_2 for an hour and then removed from the incubator and washed twice with sterile DPBS, after which they became ready for cell seeding or the application of a secondary coating.

Matrigel in solution (Corning) was stored at –20 °C, thawed overnight at 2–8 °C and then kept over ice throughout the dilution process. The Matrigel was diluted in sterile DPBS to a range of concentrations (0.1–0.4 mg/mL). The hydrogel substrates were then covered with 50 μL/cm^2 of the diluted solutions, incubated for 30 minutes, and rinsed with DPBS.

Collagen type 1 stock solution from one of two sources was diluted at 2–8 °C in sterile tissue-culture-grade deionized water to a concentration in the range 0.5–5.0 mg/mL, and was then applied to the hydrogel surfaces at 200 μL/cm^2. The samples were then incubated for an hour and rinsed with DPBS. The two different collagen sources evaluated were (*a*) rat-tail type 1 collagen (Corning), as used for the AC composites described in Chapter 4, and (*b*) bovine type 1 collagen (PureCol EZGel, Advanced Biomatrix, San Diego, CA), obtained at a concentration of 5.0 mg/mL and a pH of 6.8–7.4.

The hFN powder (Corning) was dissolved to 1 mg/mL in sterile tissue-culture-grade deionized water, frozen and stored at –20 °C, and then, after re-melting, further diluted to 50 μg/mL and used to coat the surface of the hydrogel substrates at 100 μL/cm^2. The samples were then incubated for 30 minutes and rinsed with DPBS.

All coated substrates were then covered with 100 μL/cm^2 of media containing HMEC or SY5Y cells at concentrations of 8.4×10^5 and 13.4×10^5 cells/mL respectively.

2.3. Cell types and the culture procedure

Human microvascular endothelial cells (HMECs, ATCC CRL-3243, American Type Culture Collection, Manassas, VA, USA) were cultured in MCDB 131 medium (Thermo-Fisher Scientific, Waltham, MA, USA) supplemented with 10% fetal bovine serum, 10 ng/mL endothelial growth factor (EGF, Thermo-Fisher Scientific), and 1% penicillin/streptomycin at 37 °C in a humidified 5% CO_2 atmosphere.

Human umbilical vein endothelial cells (HUVECs, ATCC CRL-1730, American Type Culture Collection, Manassas, VA, USA) were cultured in α-MEM containing 10% FBS, 10 ng/mL TGF-b1, 1% glutamine, and 1% penicillin-streptomycin, and EBM-2 supplemented with EGM-2 BulletKit and 10% FBS, respectively.

The SH-SY5Y cell line (ATCC CRL-2266, American Type Culture Collection, Manassas, VA, USA) is a neuroblastoma cell line with epithelial morphology. SY5Y cells were cultured in Dulbecco's Modified Eagle's Medium (Gibco) supplemented with 10% fetal bovine serum (Gibco), 1% non-essential amino acids (NEAA), 1% sodium pyruvate and 1% penicillin/streptomycin (Gibco) at 37 °C in a humidified 5% CO_2 atmosphere.

All subcultures were passaged at 80–90% confluence and, throughout the experiments, doubling time was around 48, 48 and 32 hours for the SY5Y, HUVEC and HMEC lines respectively. The cells were recovered at this stage after detachment from the culture plates using fresh 0.05% trypsin-EDTA (1X) solution (Gibco) and then either passaged or used in the experiments. In all long-term culture experiments, the medium was refreshed every four days.

2.4. Preparation of cell-laden hydrogel precursors

For each of the fabricated hydrogel structures, we could either culture the cells as a 2D monolayer on the surface of the solidified hydrogel, or as a 3D cell suspension mixed uniformly into the material prior to casting. Hence, both fabrication processes combine 2D and 3D culture modalities and allow for the utilization of endothelial/epithelial lumens as well as bulk 3D tissue.

In the case of the agarose-collagen composites, and for the 3D culture mode, due to the rapid cooling and thermal crosslinking of agarose, the previously described collagen solution was initially mixed with the media solution containing cells at a target density. The agarose solution was then allowed to cool to below 40°C, after which it was pipetted into the mixture. The blend was mixed thoroughly, after which it was immediately transferred and cast into the final container, where it was stamped with the respective mold. After a few minutes and the completion of the thermal gelation process at room temperature, the samples were covered with media, or in the case of multiple layers, the casting-molding process was repeated with another layer of the cell–hydrogel mixture.

In the case of the gelatin methacrylate and poly (ethylene glycol) diacrylate composites, the cell suspension was added after both components were mixed and filter sterilized. The mixture was

thoroughly hand-stirred and allowed to cool at 2–8°C. During this thermal gelation step, the precursor mixture was agitated every minute in order to ensure uniform dispersion of cells.

2.5. Cell viability, cytoskeletal and immunofluorescence staining and imaging

A LIVE/DEAD® cell viability kit (Molecular Probes L-3224) based on the integrity of the plasma membrane was utilized in accordance with the manufacturer's protocol. AC hydrogels with variations in both components were synthesized and cells were kept in culture within these hydrogel environments for a week, while the media was changed every two days. The viability of cells was evaluated after this seven-day culture period. The dead cells were stained with ethidium homodimer (EthD-1, red stain) and the live cells were stained with calcein AM (CAM, green stain). The samples were then imaged using an Axio Observer D1 fluorescence microscope (Carl Zeiss AG) fluorescent microscope at an excitation wavelength of ~495 nm and the emitted wavelengths were filtered for 495 nm (CAM) and 635 nm (EthD-1). The images were then analyzed using the NIH ImageJ software in order to obtain the cell count for live/dead cells, and viability was calculated as the percentage ratio of live cells to the total number of cells.

Alexa Fluor® 488 phalloidin (Molecular Probes A12379) was used to visualize the filamentous actin structures of the cells in our 2D and 3D cultures. DAPI (Molecular Probes D1306) was also used to counterstain the nuclei of the cells. Briefly, the culture media was gently removed from the cellular constructs, and the constructs were carefully washed with DPBS. Cells were fixed using a 4% solution of paraformaldehyde for 20 minutes after which the solution was removed and the samples were washed three times. The samples were then permeabilized with a diluted solution of 0.5% Triton X-100 (Sigma-Aldrich) for 15 minutes after which they were washed again for three times. The phalloidin solution with a 10 μM concentration was then applied and the samples were incubated for an hour in a dark environment. The phalloidin was then removed and samples were washed twice with DPBS. Finally, the DAPI solution with a 5 μM concentration was added and the samples were incubated for five minutes and then washed with DPBS. The samples were imaged using the aforementioned microscope at an excitation/emission wavelength of 495/518 nm for the phalloidin and 358/461 nm for DAPI.

The ZO-1 monoclonal antibody, Alexa Fluor® 594 conjugate (Invitrogen ZO1-1A12) was used for immunofluorescence analysis and visualization of cell junction localization. After removal of the culture medium, the constructs were washed multiple times with DPBS and the cells were fixed with 4% paraformaldehyde for 20 minutes, then permeabilized with 0.5% Triton™ X-100 (Sigma-Aldrich) for ten minutes and blocked with 5% BSA overnight at room temperature. After blocking, the cells were labeled with the ZO-1 antibody, Alexa Fluor® 594 conjugate at 5 μg/mL in 1% BSA and incubated for three hours at room temperature.

2.6. Mechanical characterization with nano-indentation

A Hysitron TI-950 Triboindenter nano-indentation system (Hysitron, Eden Prairie, MN, USA) was used to evaluate the modulus of elasticity of the samples. Hydrogel samples were prepared inside custom-made 3 mm-tall cubic containers and a 1 mm layer of deionized water covered the top surface of the samples in order to keep them hydrated throughout the indentation process. Indentations were made with 50 μm spacing, using a conospherical tip with a radius of 10 μm. The indentation force range was chosen to be 200–600 μN. This force range translated to an average depth of 5000 nm across multiple samples. The Oliver–Pharr method [63] was used to extract the effective elastic modulus, E_{eff}, from the load–displacement data using the following relationship:

$$E_{eff} = \frac{S}{2\beta}\sqrt{\frac{\pi}{A}}$$

where S is the gradient of the initial unloading portion of the load–displacement curve, β is a dimensionless geometry factor taken to equal 1, and A is the tip–sample contact area. Young's modulus, E, of the sample is related to the effective elastic modulus, the indenter Young's modulus E_i, and the sample and indenter Poisson's ratios ν and ν_i respectively by:

$$\frac{1}{E_{eff}} = \frac{1-\nu^2}{E} + \frac{1-\nu_i^2}{E_i}.$$

Since $E_i \gg E$, and the sample is primarily composed of water so that ν during indentation can be assumed to equal 0.5 (signifying incompressibility), Young's modulus of the sample can be taken to equal $0.75E_{eff}$. Young's moduli are reported in Section 4.1.

2.7. Rheological characterization

For the computed axial lithography approach, the dosage-dependency of the mechanical properties of the hydrogel are of critical importance. Hence, the viscoelastic properties of the hydrogel resins were characterized using an AR2000ex rheometer with a UV attachment (TA Instruments). An omniCure S2000 (Excilitas Technologies) passed through a 405/10nm BrightLine single-band bandpass filter (Semrok) to illuminate the samples for polymerization. The light source was set to an intensity of either 20 mW/cm^2 or 2.5 mW/cm^2 to introduce different dose rates. An aluminum 25 mm detachable parallel plate geometry (TA Instruments) was set to a gap height of 100 μm for measurement. A time sweep with an angular frequency of 2π rad/s was performed using TRIOS software (TA instruments).

2.8. Scanning Electron Microscopy (SEM)

Knowledge of the porosity and morphology of the polymeric networks is extremely important for understanding cellular motility, the structural contributions of each component of the composite,

and structure-function synergies. The ability to visualize the micro- and nano-scale polymeric scaffold and mesh that encapsulates the large water content of the hydrogel is a very useful attribute of scanning electron micrographs. The fabricated gel samples were fixed using a 4% paraformaldehyde solution (Electron Microscopy Sciences, Hatfield, PA, USA), and allowed to sit for 20 minutes. The samples were then cut into 10 mm × 10 mm squares, frozen at –20 °C for an hour and then lyophilized at a vacuum pressure of 0.015 mBar and collector temperature of –52 °C for three days using a benchtop lyophilizer (Labconco, Kansas City, MO, USA). The dried samples were then imaged using a Quanta FEG scanning electron microscope (FEI, Hillsboro, OR, USA) at 2–5 keV and 10–22 nA beam current.

2.9. Trans-endothelial electrical resistance (TEER) measurement

Trans-endothelial electrical resistance (TEER) is widely used as a measure of the tightness of intercellular junctions in an endothelial monolayer [64] [65]. Here, we have utilized TEER as a non-destructive method to evaluate the functionality and biological resemblance of our fabricated hydrogel constructs. The measurement setup consisted of two parallel silver–silver chloride electrodes (530800, A-M Systems, Sequim, WA, USA). One of the electrodes was carefully guided laterally into the lumen and the other was placed on the outer surface of the construct (Figure 27a). TEER was measured under DC conditions using an LCR-6000 high precision LCR meter (GW Instek, New Taipei City, Taiwan) every three to four days during the 11.5 days after fabrication of the vascular construct.

2.10. Perfusion system

As mentioned in the first chapter, shear stress can play a very important role in the quality, integrity and organization of the endothelial lining. The use of a perfusion system allows us to introduce not only a flow of essential nutrients and media during cell culture but also the fluorescent particles and dyes necessary to perform permeability experiments after the culture process has completed. The mechanism through which a hydrogel structure or printed tissue is connected to the external environment is another critical challenge that seems to be slightly overlooked in most published literature. The lack of a systematic engineering solution and the need to connect these jelly-like structures with extremely stiff tubing and fixturing is usually met with *ad hoc* solutions. In the present work, we have thought carefully about this engineering challenge in order to arrive at a generalized systematic solution that can leverage the overprinting capabilities of computed axial lithography and can also be applied to multiple geometrical configurations and designs.

Furthermore, the hydrogels used in this study (especially the 3–5% (w/v) pure gelatin methacrylate composition) are extremely delicate and can easily deform and rupture after extraction from the print environment. Hence, to minimize manual handling of the printed parts during the post-cure rinse and for subsequent perfusion cycles, it would be ideal to print the structures in an integrated fashion and embedded within the final incubation chamber. This is another unique advantage of

computed axial lithography which is enabled due to the volumetric and contact-free nature of the process. Thus, a capsule was designed to contain the hydrogel precursor mixture and connect the materialized vascular prints therein to the perfusion system.

This capsule consists of an 8 cm-long transparent FEP tube of 0.8 mm wall thickness (McMaster-Carr, Elmhurst, IL, USA) sealed on both sides with custom designed connectors with relevant ports for tubing connection and bubble entrapment. The custom connectors were designed in SolidWorks (Dassault Systemes, Vélizy-Villacoublay, France) and 3D-printed with VeroClear (Stratasys, Rehovot, Israel) on an Objet 260 Connex 3D printer (Stratasys, Rehovot, Israel). In addition, a fluid reservoir was also designed with the same software and printed on the same printer, as part of the perfusion system. All components were connected using Tygon® tubing (Saint-Gobain, Malvern, PA, USA).

The operation process of the capsule is designed as follows: the capsule is filled with uncured photopolymer and is sealed on each side with a piece of tubing fitting the ports of the connectors. The capsule is then transferred to the CAL printer, aligned and rotated on the stage to expose the photopolymer to 405 nm light from the projector. Afterwards, the sealing tubing is removed, and the capsule is connected to fluid lines as a part of the perfusion system. In this study, our perfusion system included a syringe filled with cell culture medium (see “Cell Culture” section 2.3) as the fluid source. The syringe is driven by a syringe pump (NE-4000, New Era Pump Systems, Farmingdale, NY, USA). The outlet of the syringe is connected to eight capsules connected in series which then connect to a reservoir for fluid reuse. After each pumping cycle is complete, the pump is reversed to withdraw from the reservoir back to the syringe. Long-term continuous perfusion in a closed system is then achieved, minimizing the risk of contamination during fluid replacement.

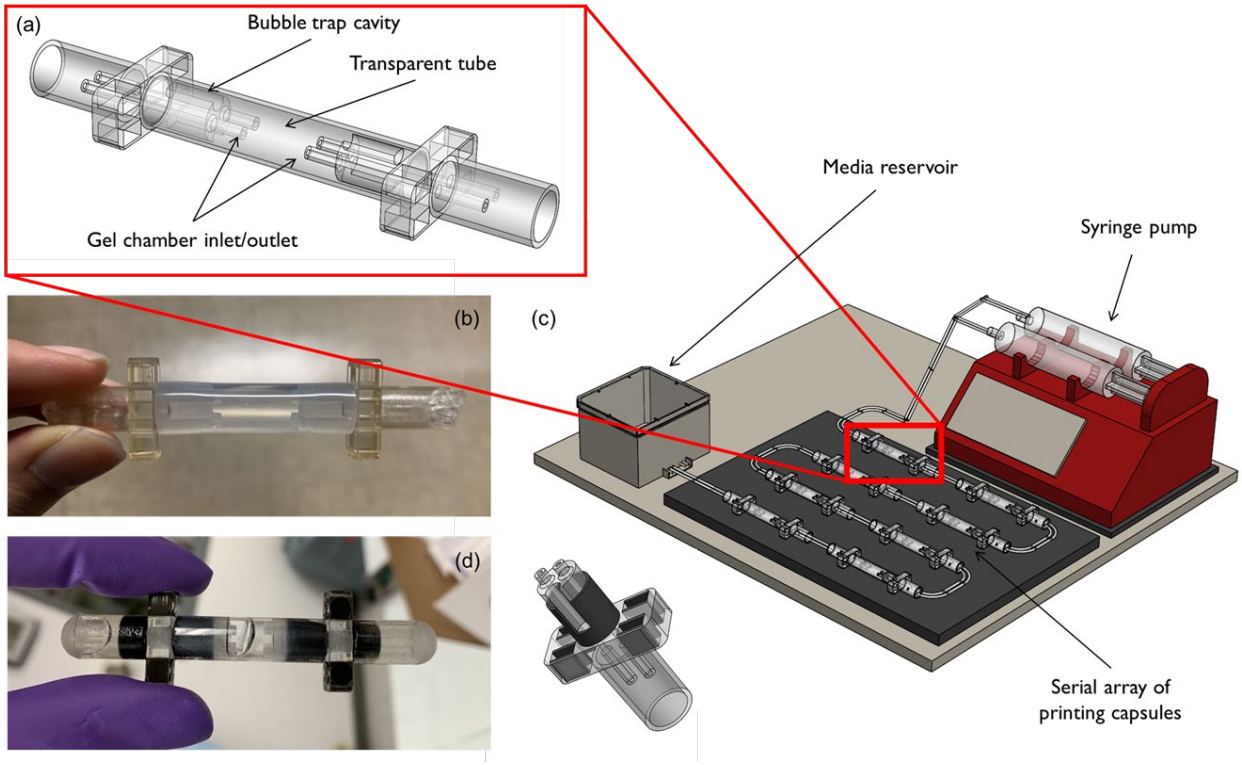

Figure 2 Design and layout of the print capsule and perfusion system: (a) capsule design with central print chamber that holds the gel, and perfusion caps on either side equipped with bubble traps and luer connectors; (b) and (d) an assembled capsule with PFE and glass used as the central tubing respectively. In the case of glass, tango black rubber linings were used to accommodate for the rigidity of the glass while maintaining a leakage-free seal; (c) perfusion system layout with a series of eight capsules connected to the flow source and reservoir.

The choice of FEP tubing for the capsule body was based on the proximity of its refractive index (n = 1.34 in 405 nm wavelength) with water (n = 1.33), its high transmittance (above 95%) at the 405 nm wavelength, and its compliance. A refractive index mismatch can amplify the image noise originating from the rough surface of the transparent tubing hence influencing the Schlieren image obtained from the vial and making it impossible to detect the object (Figure 3a). In the case of FEP, the closely matching refractive index of the material helps cloak the surface roughness and eliminate refraction from the interface allowing us to obtain a clear image of the object emerging in the vial (Figure 3b).

	Glass	Tygon®	PVC	FEP
Refractive Index	1.52	1.34	1.53	1.34
Compliance	None	High	High	Low
Biocompatibility	Good	Good	FDA food	FDA food
Transmittance at 405nm	98% and more	Not good	Okay	95% and more
Thickness	1.1mm	1.6mm	1.6mm	1.6mm
Brittle/fragile	Extremely	No	No	No
Surface quality	Good	Poor	Poor	Not bad

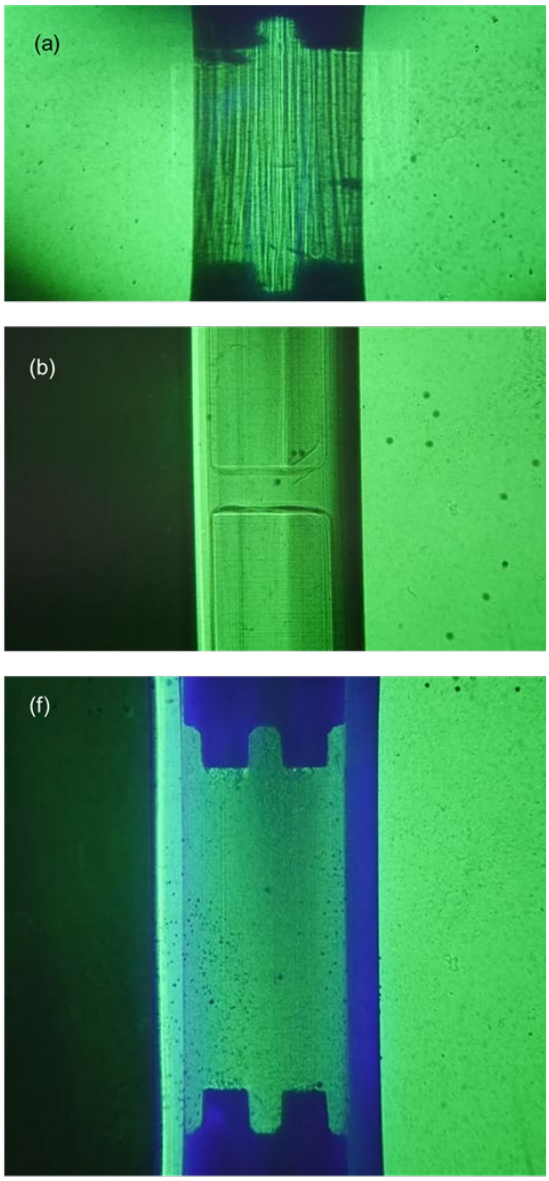

Figure 3 The effect of refractive index mismatch and choice of tubing material on the images obtained with Schlieren: (a) PVC tubing with 15 percent refractive index mismatch vs (b) FEP tubing with close to zero mismatch allowing for great visualization of the printed gels; (c), (d) and (e) images of the fabricated and assembled capsule made with the FEP tubing; (f) Schlieren image of the print chamber of the capsule showing the inlet and outlet ports integrated within the cap design.

The assembled capsules are shown in Figures 2 and 3 with different material configurations. The compliance of FEP further assists with sealing the chamber from any precursor or media leakage whereas alternatives such as glass require a rubber lining to be included in the design to prevent potential leakage (Figure 2b and d). This capsule design and choice of material was ultimately used for the perfusion experiments.

Chapter 3

Biofabrication methods

Thus far we have established the crucial importance of modelling soft tissue, and the vital role of vascular networks in almost all our organs and across different types of tissue. We have also introduced some of the most biologically relevant material candidates and compositions that are able to achieve such incredibly low stiffness values while closely mimicking the native cellular microenvironment. In this chapter we will finally introduce multi-layered micro-casting and computed axial lithography as our two fabrication alternatives to the previously mentioned techniques. We will study these biofabrication techniques in detail, while trying to unravel their innovative features and unique capabilities as well as the various components and the optimal configurations used in each process. We will also try to include any relevant experimental modifications, hardware customizations, and firmware enhancements that we found useful to the soft polymer category of materials that have been studied in the course of this work.

3.1. Multi-layered micro-casting: multi-material pattern transfer as a high-throughput indirect biofabrication technique

As we briefly reviewed in the first chapter, no prior model simultaneously meets the needs for multi-diameter branched vessels, realistic mechanical properties, and layering of multiple cell types around the lumen. The first fabrication platform that we will introduce here, however, provides a potential route to delivering all these capabilities. A sequence of casting and thermal gelation steps is used to build multi-layer coaxial structures (Figure 4a–d). The structures are produced entirely from hydrogels and the sequential casting approach allows multiple coaxial layers to be created with differing hydrogel compositions and cellular contents. In addition to culturing cells in 3D within the hydrogel materials, it is possible to culture 2D cellular monolayers on the surface of the cast hydrogel. Therefore, the technique is ideally suited to modelling the brain microvasculature, in which not only the endothelium but also the surrounding cellular structures are critically important to its function. As a result, this work goes beyond other recent work in which endothelial monolayers were grown inside channels cast in agarose–gelatin composites

[66]. We create structures in two halves using convex-geometry molds, and the halves are then bonded together to produce the final enclosed channels (Figure 1d). In principle, then, the technique can produce arbitrarily arranged networks of channels with spatially varying diameters, provided that the centerlines of all the channels are located within a single plane or can be projected onto a single plane without intersecting each other. Our method's ability to vary channel diameter with position is not easily accomplished with conventional single-layer lithographic techniques.

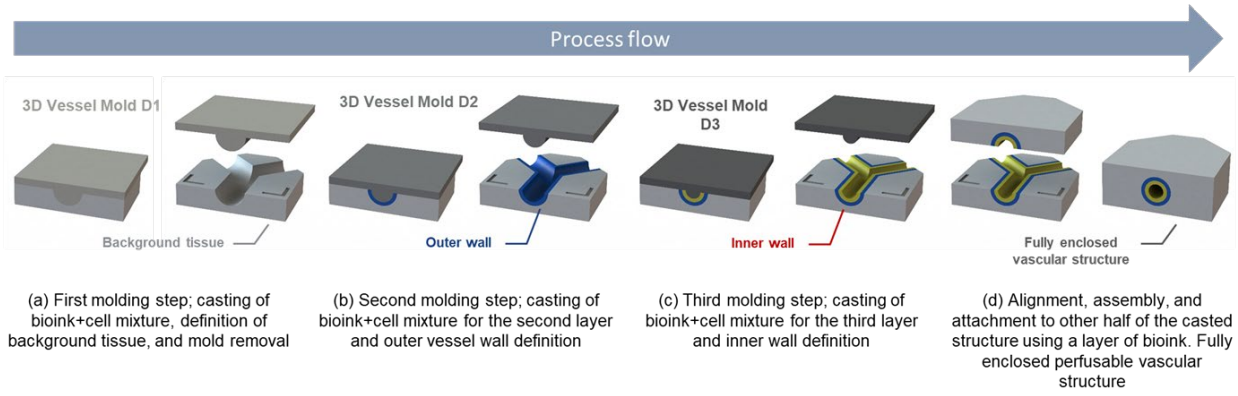

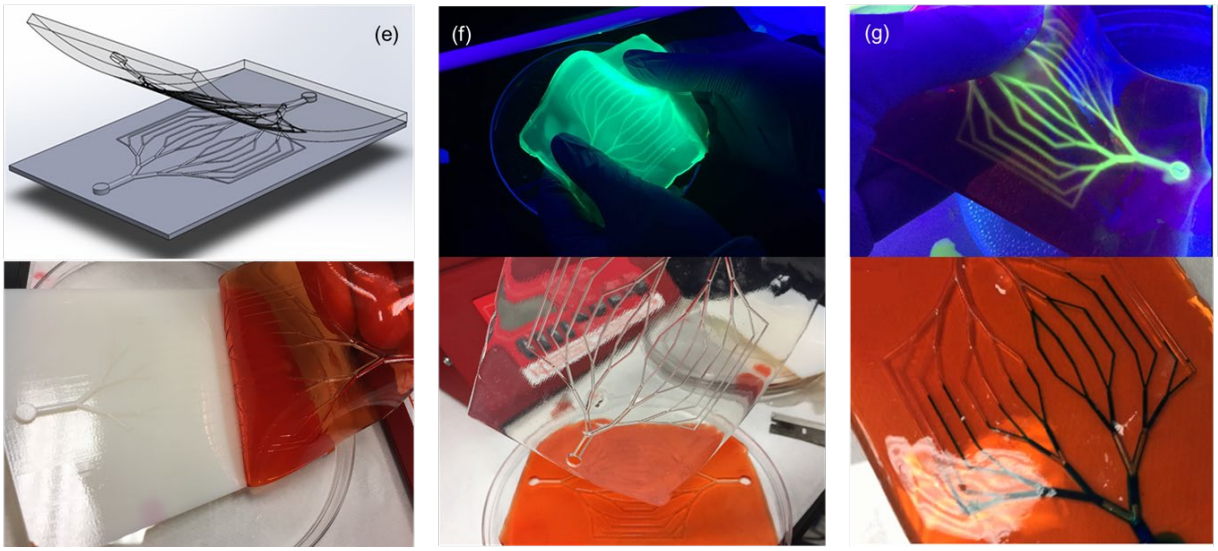

Figure 4 Stepwise fabrication process flow and vascular network replica constructs printed with multi-layered micro-casting: (a) – (d) casting process steps; (e) demolding step schematic and actual process; (f) high compliance and flexibility of the casted thin hydrogels; (g) perfusion of the assembled hydrogel construct with blue food coloring and fluorescing liquid solution. Adapted from Heidari and Taylor *[67]*.

The technique produces multilayered hydrogel structures by using a sequence of 3D-printed molds (Figure 4a–d). At each step, the hydrogel material to be cast is first liquefied by heating. In the first step (Figure 4a), the material is poured into an empty well of a standard polystyrene 12-well plate. The relevant mold is then brought into contact with the liquid to shape it, and the liquid is allowed to cool below its gelation temperature. The mold is then removed. This first step defines the bulk of the device, or the 'background tissue', containing the basic channel geometries. The second and third steps (Figure 4b–c) define cylindrical shells of hydrogel nested within the

channels that have been defined in the first step. In these steps, the liquefied material is poured on to the surface of the pre-existing cast structure inside the well. In principle, this procedure could be repeated to create further concentric layers. The volume of material dispensed at each step is precisely measured (± 0.05 mL) using a calibrated pipette to achieve the desired layer thickness. The material cast at each step can have a different composition, to tune, e.g., stiffness, cellular adhesive properties, or degradability. The material for any specific layer may also have cells mixed into it while it is liquid.

Layer-to-layer registration at each step is enabled by hydrodynamic forces in the liquefied hydrogel precursor, which act to center a mold's protrusions within previously fabricated hydrogel channels. Additionally, posts incorporated into the molds further enhance registration and enable the two halves of the hydrogel construct to interlock and form fully enclosed, coaxial structures (Figure 4d). No special surface treatment is needed for the final assembly step: the flat hydrogel surfaces naturally fuse under the action of surface tension. Prior to assembly of the enclosed structures, the two hydrogel castings are removed from their well-plates and transferred to a Petri dish. This step provides lateral access to the fabricated channel for media perfusion and electrode insertion.

The process uses agarose–collagen hydrogels, whose gelation characteristics possess a strong temperature hysteresis. This hysteresis enables the preservation of cellular viability during thermal casting, and also allows one hydrogel layer to be cast on top of another without destroying underlying structures. As detailed in the previous chapter, the gelation temperature of agarose can be tuned in the approximate range 17–40 °C, and the melting temperature of a solid gel is as much as ~40 °C higher than the gelation temperature. In this work, agarose with a gelation temperature of 36 °C is used—i.e. just below the physiological temperature of 37 °C at which the devices are to be incubated and used. Prior to casting, the material is melted by immersion in a water bath at 65 °C. It is then allowed to cool to 40 °C before any cells are mixed into it—a temperature that is too high to allow gelation but low enough not to damage the cells. The material is cast, and any underlying, pre-patterned gel structures do not come close to re-melting in this process. The cast layer is then allowed to fall to room temperature to induce gelation. When subsequently raised to the incubation temperature of 37 °C, the structure remains solid.

For each layer that is to be cast, a 3D computer model of the desired channel geometry is converted into a design for a corresponding, separable two-part mold with the required alignment protrusions. The molds are 3D-printed using an Objet Connex 260 3D inkjet printer (Stratasys, Rehovot, Israel) with a nominal layer thickness of 16 μm, an in-plane edge-placement precision of approximately ±50 μm, and a minimum in-plane feature size of ~250 μm. The resin used, VeroClear™, is an acrylate-based photocurable material [68]. If finer resolution is needed, alternative mold-making processes such as microstereolithography [69] could be used. In fact, in this work, to probe channel sizes down to diameters of approximately 175 μm, the veins on the underside of a natural tree leaf were used as a mold.

3.2. Computed axial lithography: volumetric additive manufacturing as a fast and scalable direct biofabrication technique to produce structures with extremely low stiffness

As we have discussed so far, the simplicity and convenience of most indirect biofabrication techniques and the numerous advantages they may offer has proven their success in many cases. However, the necessity to engineer and fine tune the details of most process steps, tool configurations and fixtures for every new design means that they're probably not the ideal biofabrication solution for the long run. The ideal biofabrication technology similar to that of any other sub-branch of manufacturing, is to decouple the material and geometry problems from the fabrication method, be able to automate the manufacturing process as much as possible, eliminate the human factor and part handling, and produce any arbitrary geometry without the need of customized fixtures and tools.

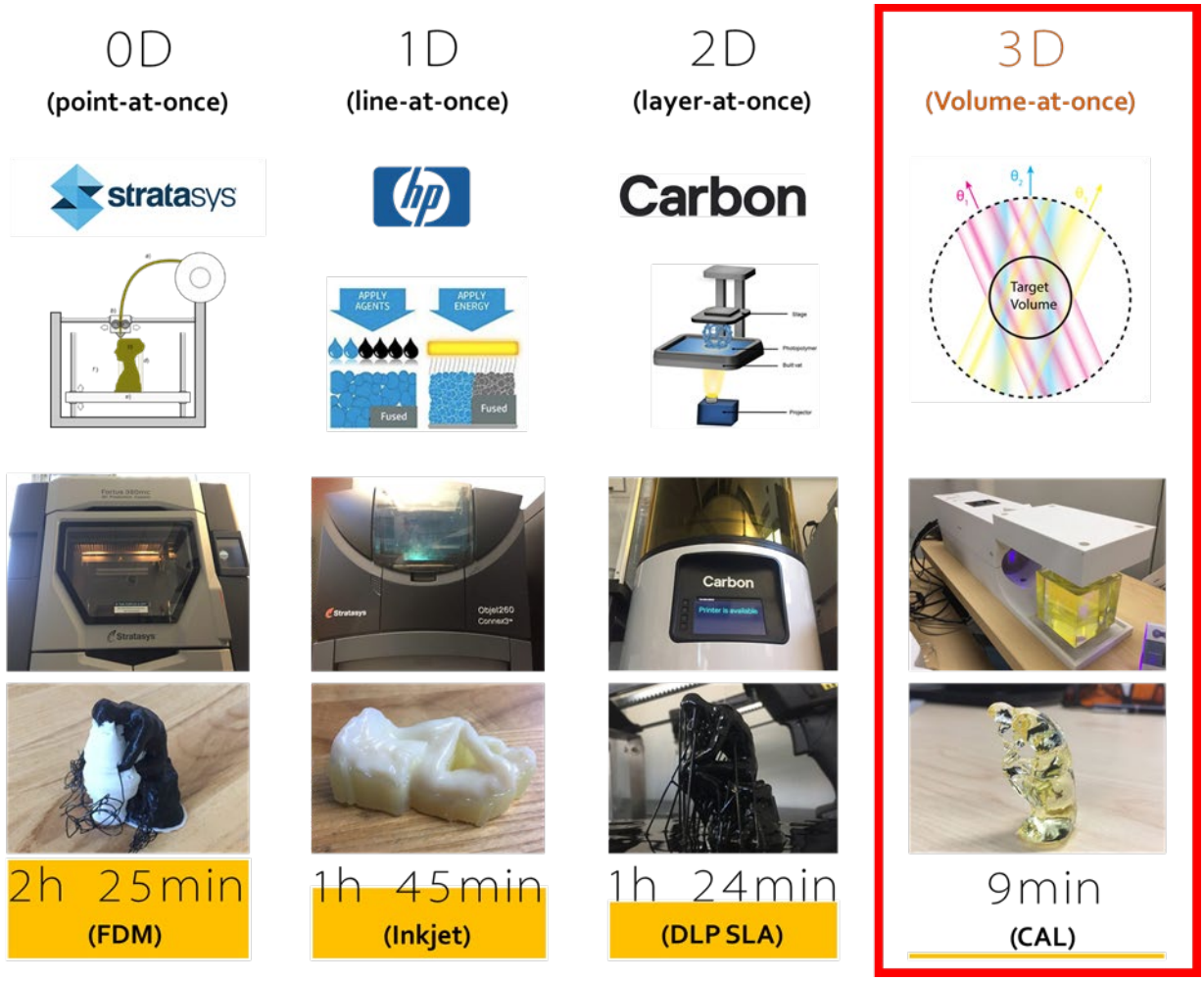

Figure 5 Comparison of different additive manufacturing processes classified by the dimensionality of the sub-unit printed at every step of the process. The extensive use of support structures that are almost always considered as waste, is eliminated with CAL. Furthermore, the surface roughness of the parts printed with CAL is superior to that of the competition. Finally, print speed can be one to two orders of magnitude faster as a result of volumetric exposure and materialization.

Additive manufacturing processes create 3D geometries through repeated one- or two-dimensional unit operations. The nozzle-based extrusion processes that we reviewed in the first chapter are all zero-dimensional as they form the object one point at a time. Inkjet processes are typically one-dimensional as they use an array of nozzles that jet the fluid one line at a time. Finally, conventional lithographic processes that cure a thin layer of bio-ink are two-dimensional as they build up the construct one layer at a time. Such layer-by-layer approaches limit throughput, require the use of sacrificial support, constrain material capabilities to less deformable biomaterials, increase post-processing requirements during which deformations can occur, and may cause anisotropy of mechanical properties. All the above-mentioned constraints and limitations are extremely important in the context of tissue models and cellular microenvironments (Figure 5). A biofabrication technique capable of simultaneously fabricating all points within an arbitrary three-dimensional geometry would address these issues.

Apart from the substantially increased throughput and the elimination of support structures, the volumetric nature of such a process that enables the use of a thixotropic thermally gelled precursors allows us to print extremely delicate and highly compliant hydrogel structures while keeping the cells uniformly dispersed throughout the print. Use of an enclosed print volume that remains untouched throughout the process also eliminates the potential risk of contamination. Moreover, by forming the 3D constructs volumetrically rather than in sequentially defined layers, for the first time the integration of external components and compartments that can serve as the interface between the printed structure and the external systems such as the perfusion system is made possible.

In this section we will present a method, computed axial lithography, which is capable of synthesizing arbitrary geometries volumetrically through photopolymerization. This approach is fundamentally different from conventional layer-based bioprinting methods, thus offering the possibility to print deformable 3D structures with much lower elastic moduli, much higher viscosities—or even solid—photosensitive resins and hydrogels, while avoiding the use of cumbersome dedicated supporting structures. We have previously shown that computed axial lithography is exceptionally scalable to larger print volumes [70], and under a wide range of conditions offers the potential for several orders of magnitude faster printing than layer-by-layer methods as we will demonstrate here. The computed axial lithography system developed in this work selectively solidifies a photosensitive liquid within a contained volume. Light energy is delivered to the material volume as a set of two-dimensional projections. Each image projection propagates through the material from a different angle. The superposition of exposures from multiple angles (Figure 6a) results in a three-dimensional energy dose sufficient to solidify the material in the desired geometry. This process is inspired by the image reconstruction procedures of Computed Tomography (CT), which has been widely used in medical imaging and non-destructive testing [71], but whose core concepts have not previously been applied to additive manufacturing. In the CAL process, nonlinearity in the response of the material to the optical dose allows for exact recovery of the sculpted geometry.

Figure 6c shows a schematic of the computed axial lithography setup used for the purpose of the bioprinting experiments detailed in this thesis. A DLP projector outputs the computed projections, time-sequenced to the rotation rate of vial containing the uncured photosensitive hydrogel precursor material. During the inhibition phase, the free radicals are generated by light activation and are rapidly quenched and deactivated by oxygen [72]. For the material to begin to crosslink at a given position in the volume, oxygen must be sufficiently depleted. The oxygen inhibition requirement enables the thresholding behavior of the material and a nonlinear response to dosage. The projection sets are designed so that the entire volume of the object overcomes inhibition simultaneously and materializes altogether, quite unlike conventional AM technologies which build parts point-by-point or layer-by-layer.

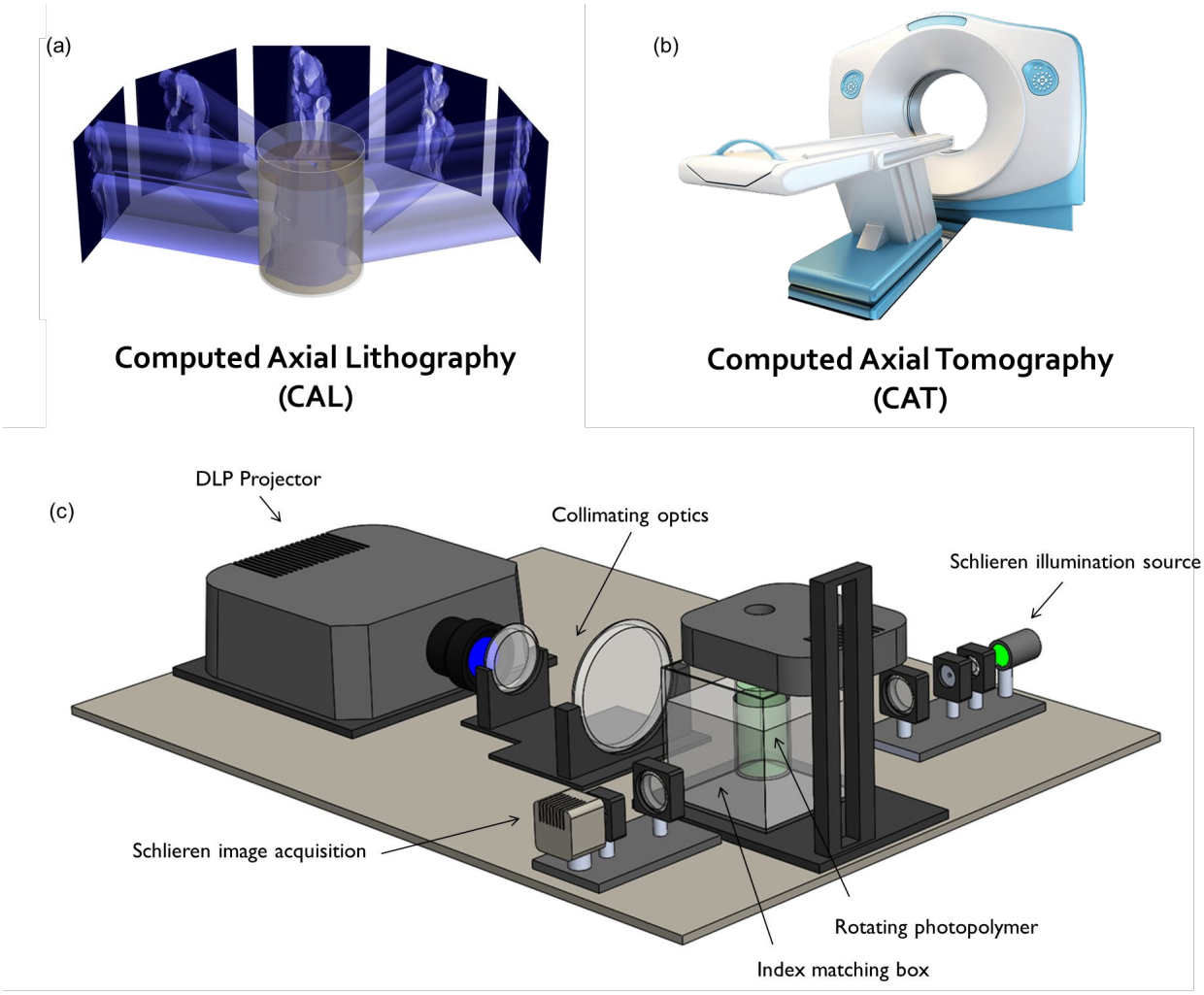

Figure 6 Tomographic reconstruction process used in computed axial lithography: (a) angular superposition of two-dimensional intensity maps projected through the volume of resin results in an overall dosage distribution; (b) the analog of such a process used in conventional computed axial tomography systems utilizing reconstruction of the three-dimensional model from two-dimensional images acquired from different angles; (c) schematic of the setup used for the purpose of this work.

The DLP projection system used for printing the hydrogel structures utilized a DLP Lightcrafter 4500 projector with 4K resolution customized by Keynote Photonics. The light source was a 405 nm LED with a quoted optical output power of 2.5 W. The projection system was controlled via custom MATLAB scripts and programmed to output patterned intensity images using the 405 nm channel. Two plano-convex lenses with 100 mm and 200 mm focal distances were used to collimate the light expanding from the built-in lens tube of the projector (Figure 7). The projector image size at the central plane of the cylindrical build volume was 130 mm by 75 mm thus providing a nominal pixel size of 47 µm and a light intensity of 25 mW/cm^2.

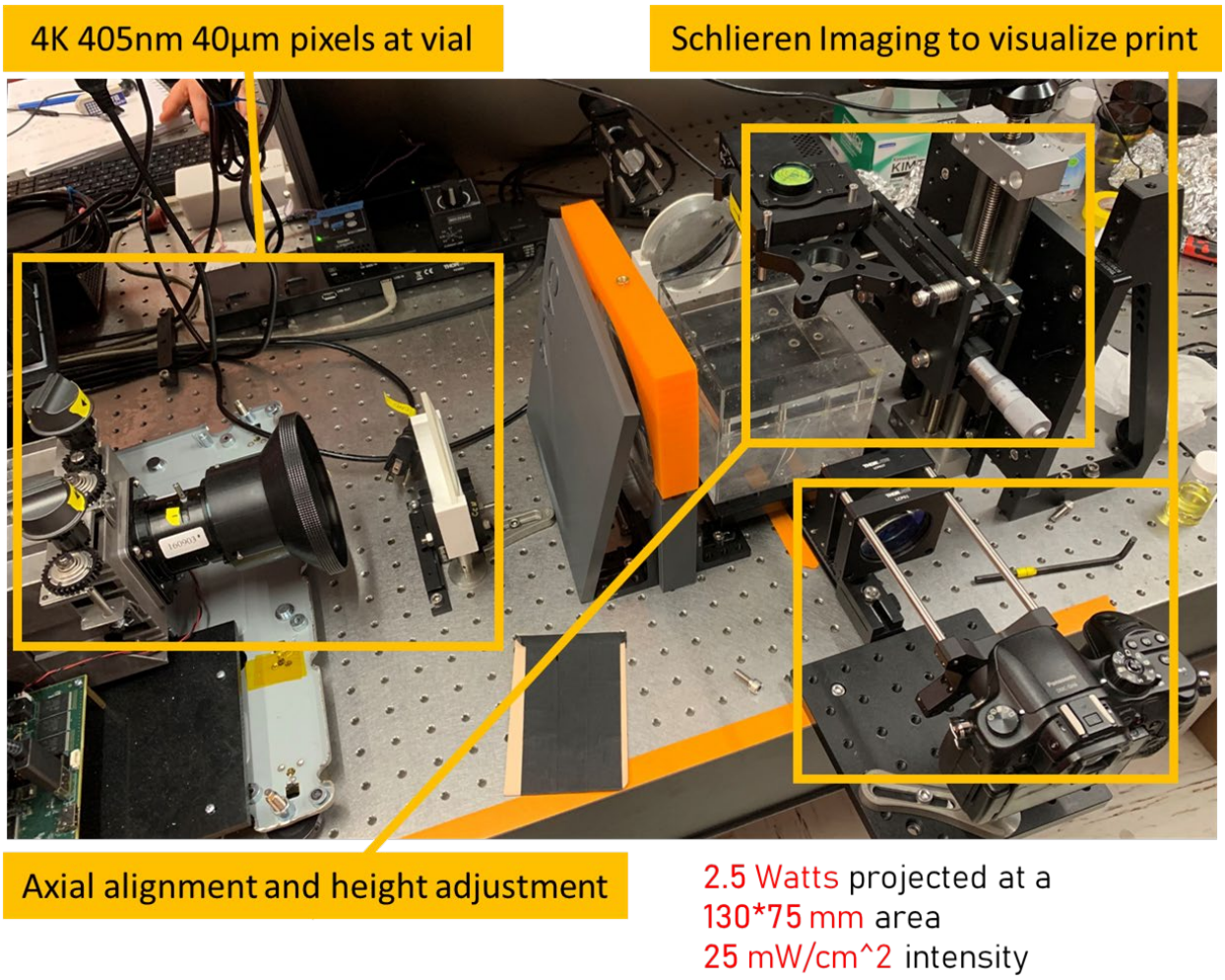

Figure 7 The six-inch printer setup and its various mechanical and optical components.

For the Gel-Ma based composite hydrogels used here, the precursor material is initially thermally gelled to minimize relative motion between the printed object and the precursor, as well as to slow down molecular diffusion-induced blurring in accordance with the Stokes–Einstein relation. In order to retrieve the printed objects, the print container is heated so that the uncured material liquefies. The printed constructs can be further cured using flood exposure in a post-cure chamber

to enhance material properties and complete the polymerization process. The uncured precursor was contained in cylindrical glass vials with diameters in the range 9–40 mm.

Each vial is rotated about its longitudinal axis using a Thorlabs K10CR1 motorized precision rotation mount with a 3–25 °/s rotation rate. The coupling of the vial with the rotation stage is achieved using a magnetic kinematic coupling mount. An example of a custom designed version of this mount is shown in Figure 8b and 8d that was used for the four-inch system displayed in Figure 8a and 8c. An alternative design was used for the six-inch high-resolution system that utilized a commercial Thorlabs SB1 kinematic base. The vial is immersed in a fluid with the same refractive index as the uncured resin—typically by using water which constitutes more than 90% of our hydrogel samples. This index-matching fluid is contained in a transparent rectangular box, two of whose faces were perpendicular to the light propagation direction to minimize beam refraction. In all the different material compositions, the content is mixed for best uniformity and the print is done immediately after the cooling and thermal gelation step so that the solubility difference wouldn't cause the development of an oxygen gradient. The temperature of the index matching solution was also reduced to 10 °C to maintain the temperature of the thermally gelled hydrogel while avoiding build up of a vapor film at ambient humidity levels.

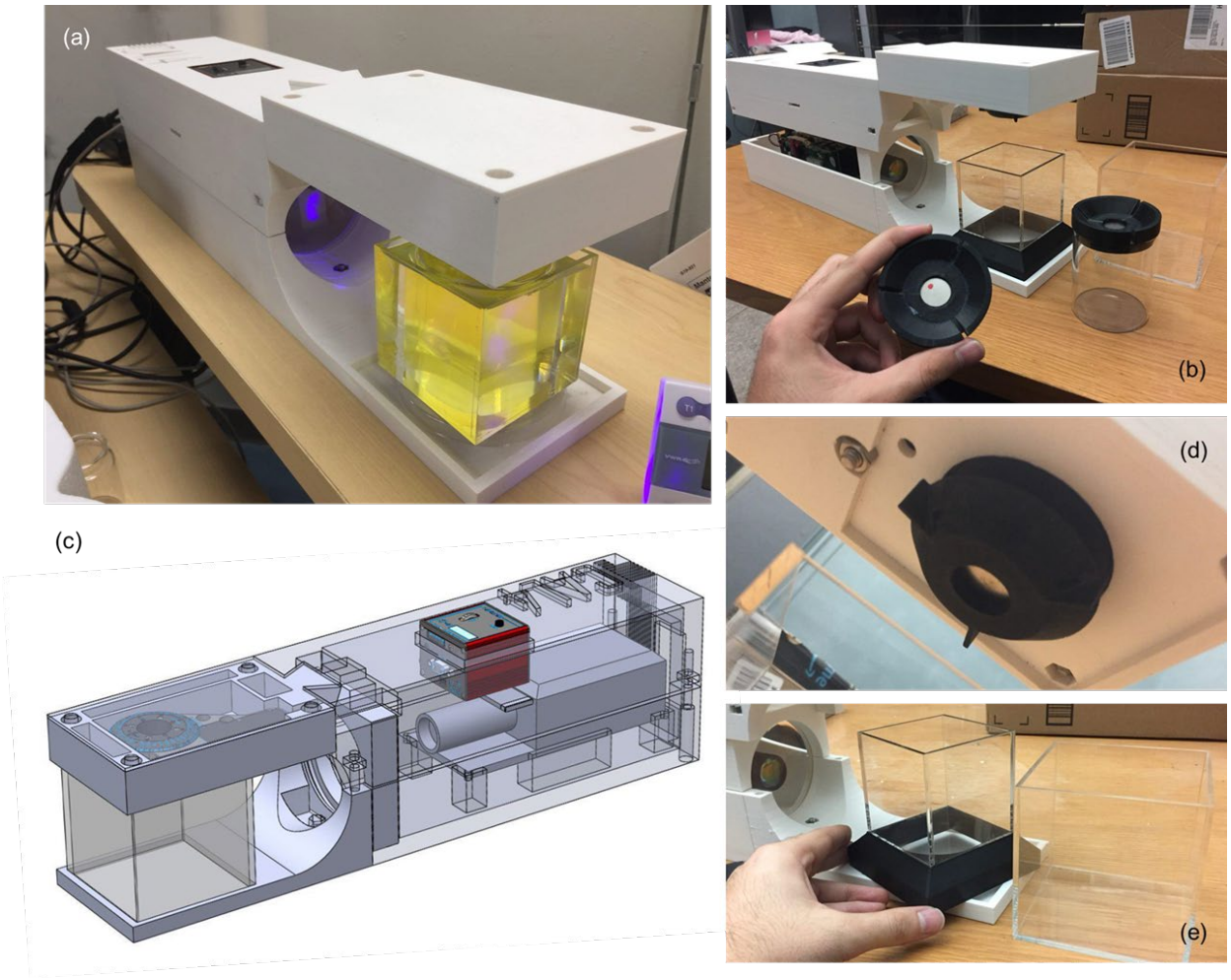

Figure 8 The four-inch printer setup, various mechanical and optical components and customized fixturing. (a) the physical printer assembled altogether; (b) and (d) the magnetic clamping mechanism used the suspend the vial in the index matching box; (c) a 3D model of the printer assembly showing all the mechanical and optical components used; (e) the acrylic index matching box.

Using commercially available projection hardware, the CAL system of Figure 8 demonstrates remarkably fast build times. The 50 mm tall object with the thinker geometry shown in Figure 5 is completed in less than ten minutes. A large range of geometries (Shown in the next chapter) have all been produced in the time range 1–20 mins, with lateral sizes up to ~40 mm, using intensities in the range ~20–25 mW/cm^2.

The Schlieren system shown in Figures 6 and 7 utilized a green LED light-source that was precisely collimated using two plano-convex lenses with 100 mm and 50 mm focal distances and a pinhole on the illumination side. On the image acquisition side, a knife edge effect was produced using a razor blade attached to a Thorlabs CXY1 30 mm cage system and XY translating lens mount. Another set of plano-convex lenses with 100 mm and 50 mm focal distances were also used. The image was collected using a 4K DSLR camera with a 1-inch CMOS sensor (Panasonic, Osaka, Japan).

Chapter 4

Biofabricated constructs, mechanical and biological characterization

In this chapter we will investigate the mechanical and biological quality and performance of our printed structures. Initially we will examine the behavior of the composite hydrogels as we vary the fabrication parameters and the concentrations of different components. We will look at important metrics such as cell viability and the rheological behavior of the composite hydrogels, the colonization and aggregation of cells and microvascular networks within the gel, and two-dimensional growth of endothelial sheets and lumens. Then we will transition to vascular specific characterization tools that are commonly used to analyze the quality and functionality of the endothelial interface. For this purpose, we will stain and image the biological markers for tight junction proteins as well as cytoskeletal actin structures, measure the trans-endothelial electrical resistance throughout the growth of the endothelium, and view the three-dimensional configuration of the microscopic and macroscopic vessels using confocal imaging.

4.1. Mechanical and structural characteristics of agarose-collagen composite hydrogels used in multi-layered micro-casting

Whether in the case of a 3D matrix surrounding the cells omnidirectionally, or a 2D surface supporting sheets of cells, ECM stiffness, is one of the few well-known mechanical cues, with significant influence on the biological performance of the cellular constructs. One of the main advantages of composite hydrogels is the controllability of the gel stiffness and porosity by modulating the concentration of the hydrogel components in the pre-gel mixture [73]. In the case of both multi-layered micro-casting and computed axial lithography, we have utilized composite hydrogel matrices. In the following sections we will look at the ways in which the characteristic mechanical properties of the matrix can be influenced by the different components.

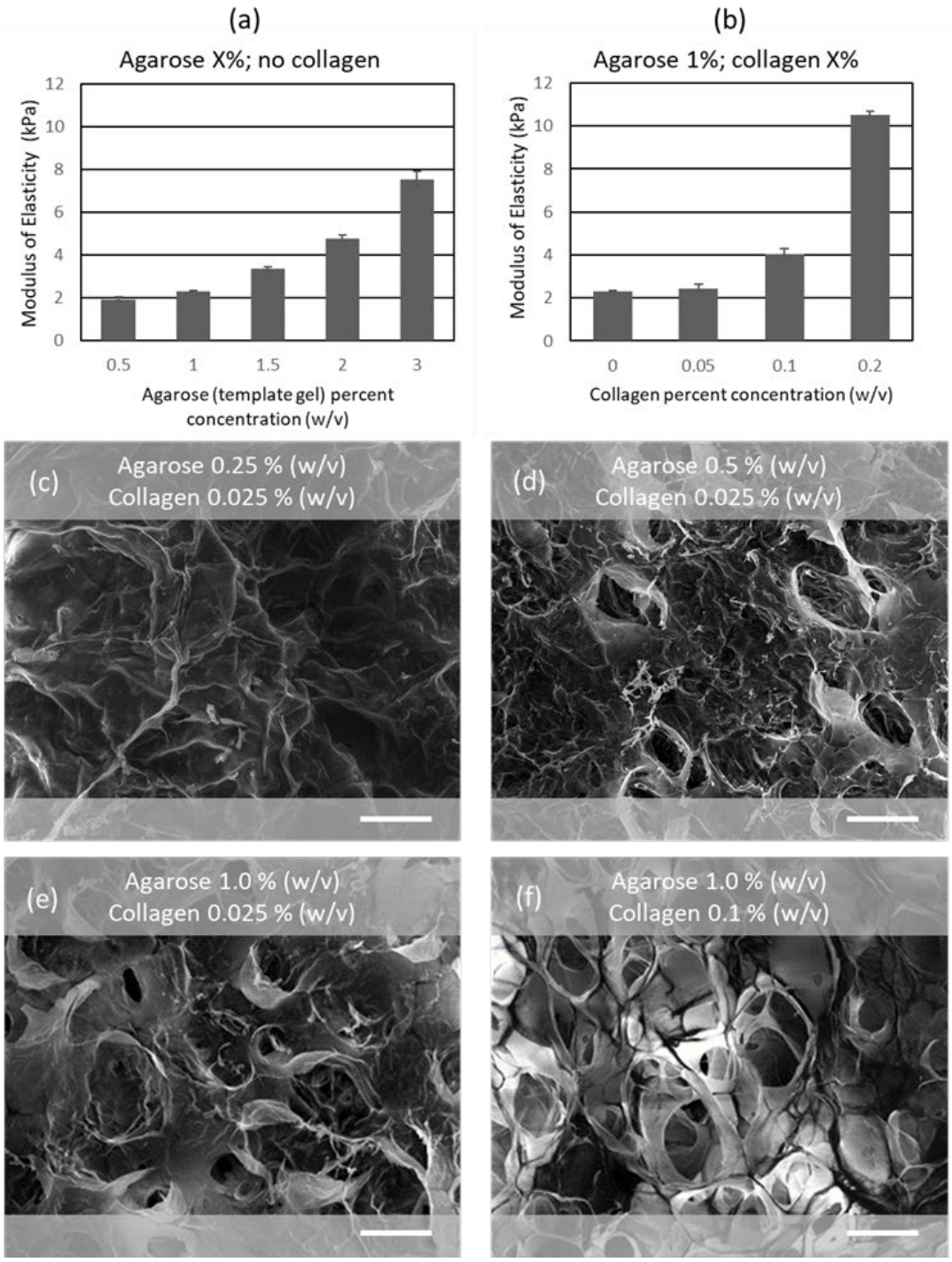

Figure 9 Mechanical properties and microstructure of agarose–collagen hydrogels. The effects on hydrogel elastic modulus of varying (a) agarose and (b) collagen concentrations show the stronger effect, weight for weight, of collagen concentration. The moduli achieved are comparable to those of in vivo cerebral and vascular tissue. Error bars in (a) show ± one sample standard deviation; those in (b) show ± one standard error of the mean, based on the number of measurements shown in the supporting information. Electron micrographs of lyophilized gel structures indicate: (c–e) a reduction in the average diameter of pores at higher agarose concentrations, and (f) added structural support from apparent fiber bundles at higher collagen concentration. Scale bars are all 100 μm. Adapted from Heidari and Taylor *[67]*.

For the case of the agarose-collagen composite system, we started by investigating the mechanical stiffnesses of agarose hydrogels with no added collagen. As the concentration of agarose was increased from 0.5% to 3.0% w/v, Young's modulus of the gel, measured by nanoindentation, increased nonlinearly from 1.4 kPa to 5.6 kPa (Figure 9a). The agarose concentration was then fixed at 0.5% w/v and samples were produced with collagen content varying from 0.05% to 0.2% w/v. The addition of the collagen resulted in Young's moduli of the composite hydrogels ranging from 1.4 kPa to 5.1 kPa (Figure 9b). Meanwhile, fixing agarose content at 1% w/v and varying collagen over the same range yielded Young's moduli ranging from 1.8 kPa to 8.3 kPa. These results overlap with the large range of measured mechanical properties of brain tissue summarized in Chapter 1 [1]– [3], indicating that the agarose–collagen system is suitable for BBB modeling. We also note that while the lowest Young's modulus of the gels we made is 1.4 kPa, we have no evidence that this is a lower limit of the material system, and it may well be possible to achieve lower moduli with different compositions.

The results also show that, weight-for-weight, collagen content results in considerably higher moduli than agarose: for example, the addition of 0.2% w/v collagen to a 1% w/v agarose gel increases Young's modulus by 6 kPa, whereas in a purely agarose gel, 3% w/v is needed to approach a modulus of 6 kPa. Elastic modulus alone, however, does not provide a complete picture of mechanical suitability. In preliminary tests, we found that gels composed only of collagen—even at polymeric contents as high as 10 mg/mL—readily disintegrated when handled as monolithic layers without any other support. This finding suggests that they would be unable to survive the mechanical manipulation needed to assemble the 3D structures described in Chapter 1. Therefore, the relationship between agarose and collagen appears to be synergistic, with some agarose content being needed for the casting process.

An important difference between the multi-layered micro-casting and previous techniques is that, in this process, cast gel layers are peeled from the mold and manipulated after casting (Figure 9e–g) without any additional supporting material present. They thus require greater integrity than gels that are simply injected into microfluidic channels and remain there (*e.g.* [74]) or gel layers that are cast against and then separated from a mold while being supported by a more rigid material on the back-side (*e.g.* [69]). In those prior microfluidic devices, plain collagen at ~10 mg/mL was used successfully, but our work has the advantage of being able to produce much larger areas of patterned material that can be directly handled without support. For example, in Figure 9e–g we show a cast network of branched channels on a 150 mm × 100 mm hydrogel sheet. The ability to handle hydrogel layers without support provides a plausible route to assembling multi-level, deformable tissue and organ models in the future that are beyond the scope of microfluidic gels confined within rigid materials.

To gain better insight into the interactions between agarose and collagen in these hydrogels, we used scanning electron microscopy to image the porous structures of lyophilized samples with various compositions. Agarose structures with very low collagen concentrations (Figure 9c–e) resemble a tangled mesh of thin, membrane-like material. The mesh density is seen to increase with agarose concentration, resulting in a decrease in the average pore size. The addition of collagen above approximately 0.05% w/v (Figure 9f), however, results in the appearance of a more

'wireframe'-like network, in which thicker bundles of fibers with diameters as large as a few micrometers have polymeric membranes stretched between them. This organization of the polymeric constituents into thicker wires of material than in the low-collagen cases is expected to reduce buckling and bending of the network, and thus increase the network's specific stiffness considerably.

4.2. Mechanical and structural characteristics Gel-Ma-PEG-Da hydrogel composites used in computed axial lithography

In order to evaluate the viscoelastic behavior of the hydrogels used for computed axial lithography, we incorporated a rheological characterization scheme. We utilized a dynamic exposure system and measured the complex response of the hydrogel as a function of exposure time. This would allow us to determine the exact modulus of the printed part after a known exposure and print time.

Two different exposure scenarios were studied. The first one involved 30 seconds of constant illumination with a 405 nm LED source at an exposure intensity of 25 mW/cm^2, and in the case of the second one, the illumination continued throughout the entire measurement window.

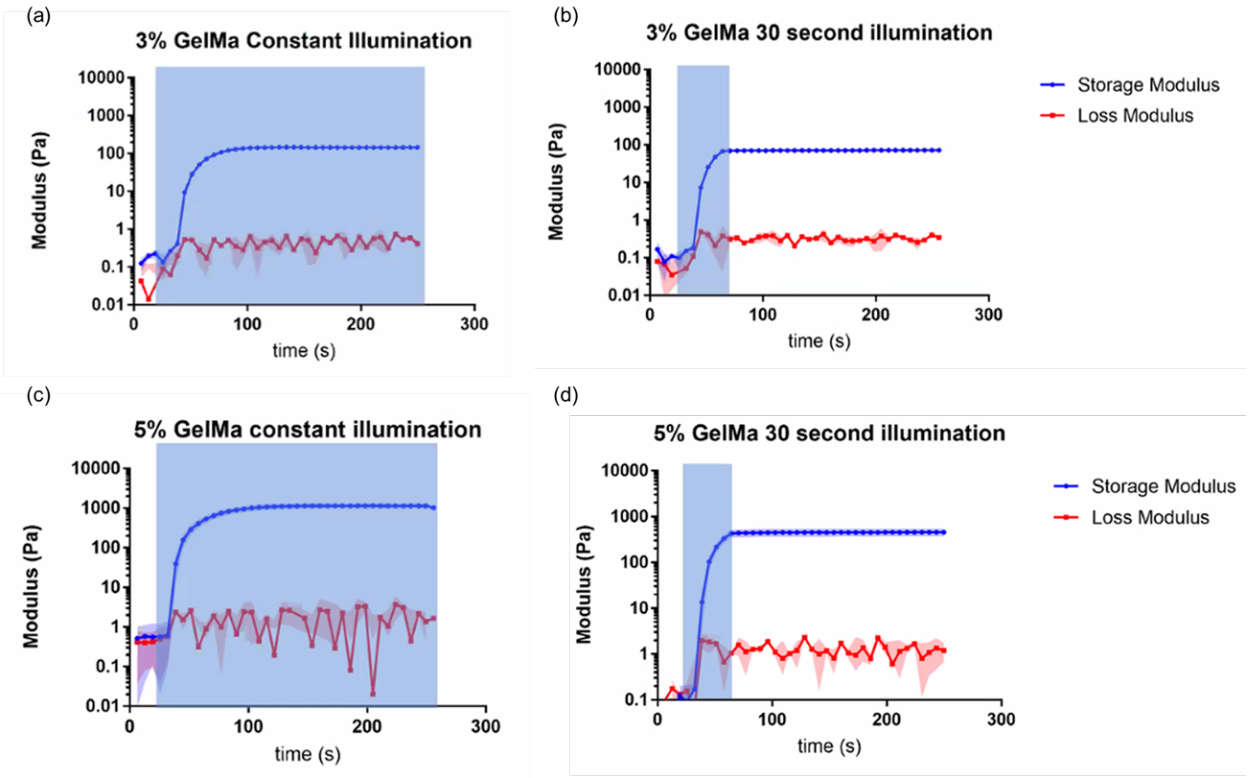

Figure 10 Photo-rheology to determine the elasticity of the gels as a function of exposure time: (a) and (c) constant exposure with a 405 nm light source; (b) and (d) the exposure window is shortened to only 30 seconds.

The results of the first exposure configuration suggest that the 5% Gel-MA hydrogels reached an elastic modulus of 300 Pa after a 30 second exposure, while the 3% Gel-Ma hydrogels reached an astonishing low modulus of less than 100 Pa (Figure 10b and d). Keeping the exposure on for the entire four-minute measurement window would allow further material conversion and a rise of modulus to a plateau value of 1000 Pa for the 5% Gel-MA, and 150 Pa for the 3% Gel-MA hydrogel (Figure 10a and c). Such low modulus values confirm the suitability of these matrices for three-dimensional cell-embedded prints. In the next sections we will observe the influence of this mechanical property on cell proliferation and microvascular network formation.

4.3. Fabricated hydrogel constructs

Unlike the multi-layered micro-casting process that can readily replicate hollow structures due to the nature of the pattern transfer process, computed axial lithography relies on careful dosing of the light energy delivered to the material as well as sensitive thresholding of material conversion. Hence, the following preliminary experiments were conducted to better understand the material and evaluate the challenges associated with printing, handling and post-processing the constructs.

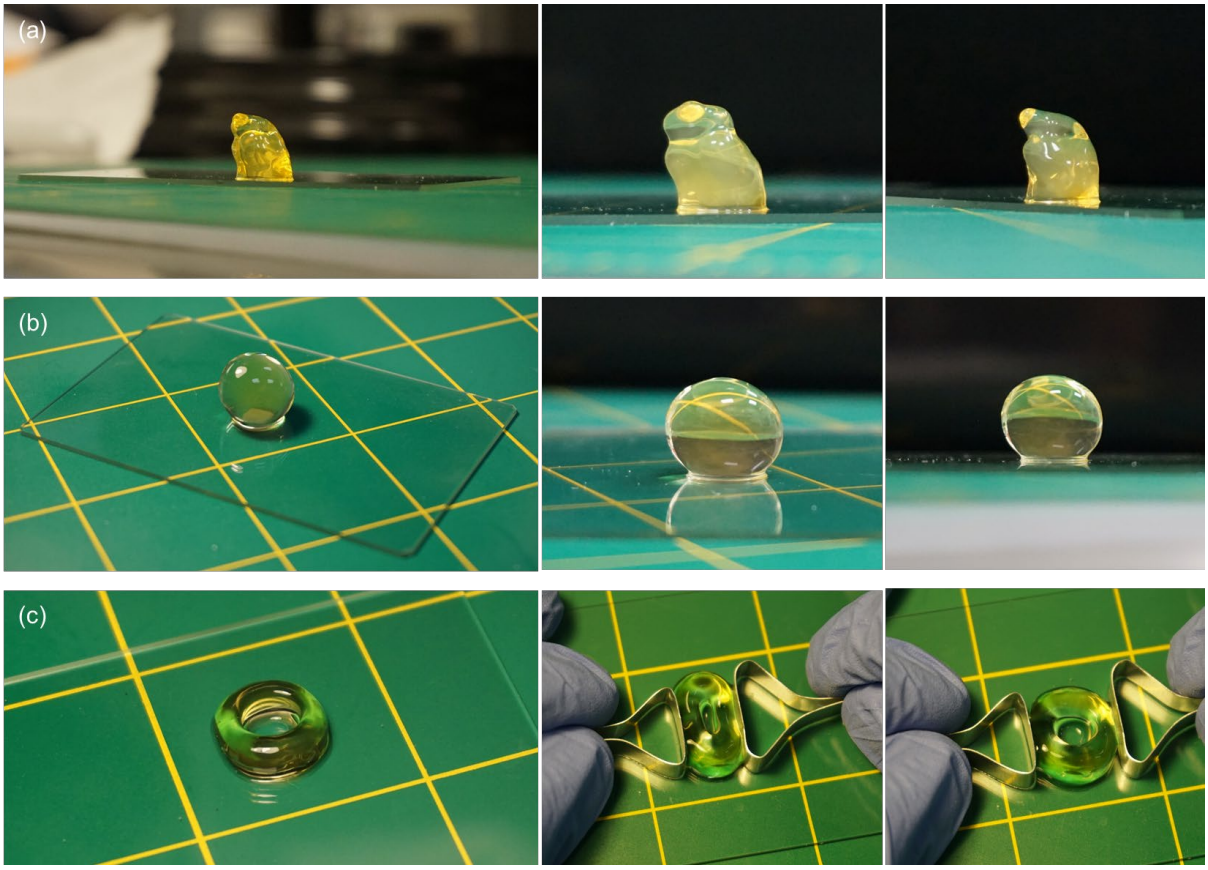

Figure 11 Preliminary test prints with Gel-Ma 5% showing the ablated features, compliance and deformability of the prints, and the smooth layer-less finish: (a) thinker with overexposed features; (b) sphere with extremely smooth finish; (c) donut demonstrating the flexibility and compliance of the hydrogel. Adapted from Kelly *et al.* *[70]*.

A first example is provided in Figure 11a where a thinker has been printed in 5% Gel-MA. A couple of things to note from this experiment are the seemingly dilated and over-cured features of this object, the slightly collapsed height of the thinker and the extremely smooth surfaces. The first could be a result of rapid over-curing that happens during the last minute of this three-minute print. Diffusion of oxygen and reactive species is extremely faster in water than in a viscous resin, hence feature dilation as a result of fast transport is expected to be more significant. The collapsed height of the object happens after removal from the print volume and like the donut of Figure 11c demonstrates yet again how deformable and compliant the gel under study is. The smooth finish of these prints is a result of the elimination of layers from the print process.

The results further exemplify the complications associated with hydrogels with such low stiffness values. To address the challenges above, improvements were made: as mentioned before, a contact-free perfusion capsule would eliminate the requirement to remove the parts after print completion; prints were repeated with consistent thermal gelation times to replicate the exposure timing and delivered dosage as accurately as possible; the projection sets were enhanced, altered and optimized to produce better dosage contrast at feature edges and hollow regions.

4.4. Perfusable hydrogel structures

The next challenge was to print hollow perfusable structures out of these extremely compliant gels. To better understand the complications associated with printing hollow features and internal cavities, we started by experimenting with engineering resins. Here we will summarize our findings with respect to the computed axial lithography process and this specific class of perfusable hollow structures that we're most interested in for the purpose of this work.

As mentioned before, two unique advantages of CAL are the ability to print objects without the use of support structures, and the ability to keep extremely delicate objects intact throughout the print process regardless of their compliance and deformability. Here we will experimentally demonstrate these two advantages and many other unique capabilities of CAL such as overprinting that we will utilize here for integration purposes, print speed and volumetric stacking of objects that enables a convenient use of build volume.

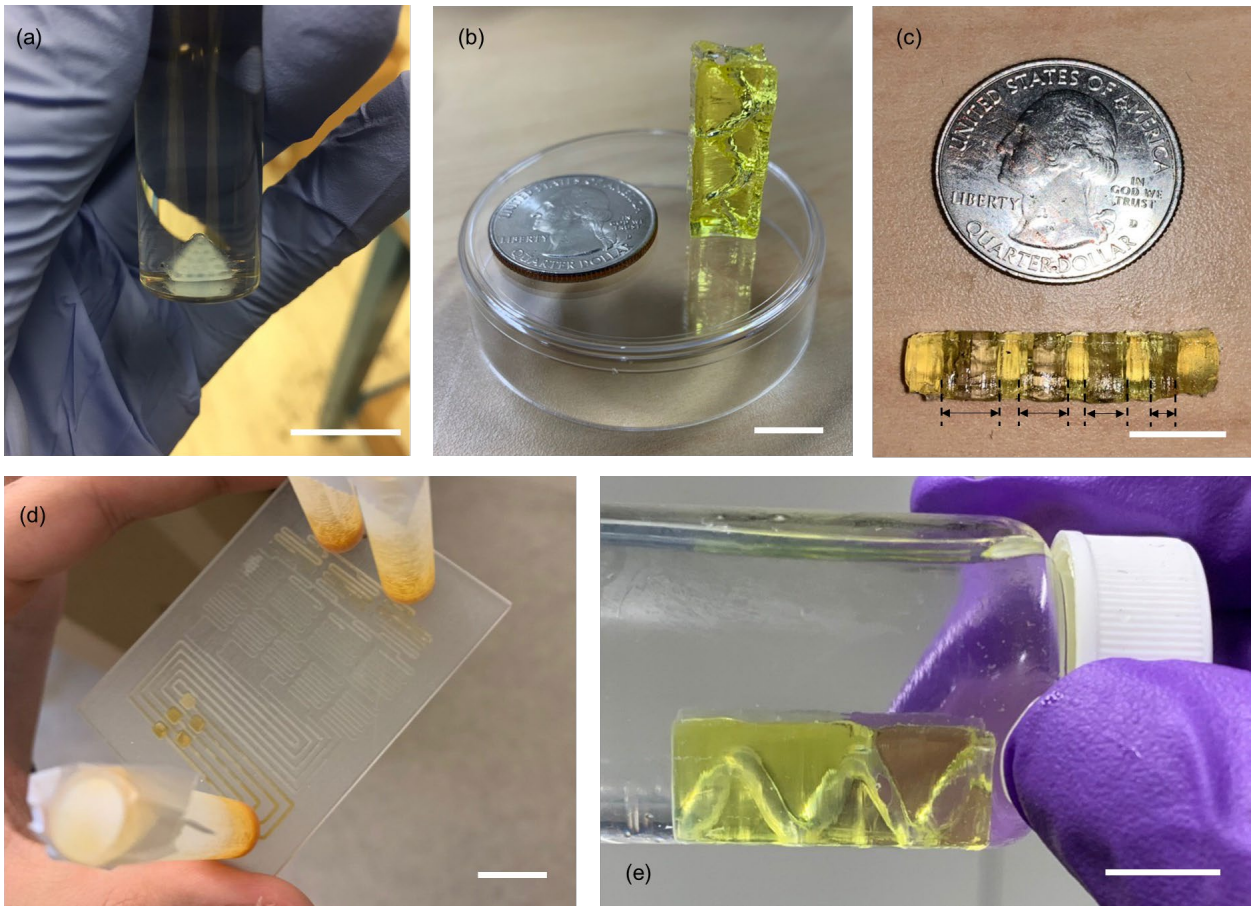

Figure 12 Perfusable structures printed in engineering resins: (a) a 3D gradient generator; (b) a hollow spiral channel; (c) a test piece with varying channel diameters ranging from 0.5 to 2 mm; (d) a perfusable gradient generator chip printed on an inkjet printer; (e) ease of support removal in a perfusable spiral structure printed with CAL. Adapted from Heidari *et al.* *[75]*.

One of the substantial advantages of CAL over other additive processes is the elimination of support structures and support material waste. The perfusable gradient generator shown in Figure 12d is printed on an inkjet printer. The soluble solid support material entrapped in the channels requires days to get fully removed from those cavities. The printed construct shown in Figure 12e was immediately cleansed after 5 minutes of heating at 65 °C and rinsing with isopropyl alcohol. This process is much easier for hydrogels because the uncured gels go back to the viscosity of water upon heating at 37 °C and can then be removed very simply. To put this advantage in precise terms, the uncured material surrounding a CAL print serves as a support holding the part buoyant due to the small density change. This thermally gelled or liquid uncured material can be easily removed by heating up the vial and pouring out the excess material. This uncured material can be easily recovered by allowing the resin or hydrogel precursor to equilibrate in an oxygen-rich or even ambient environment.

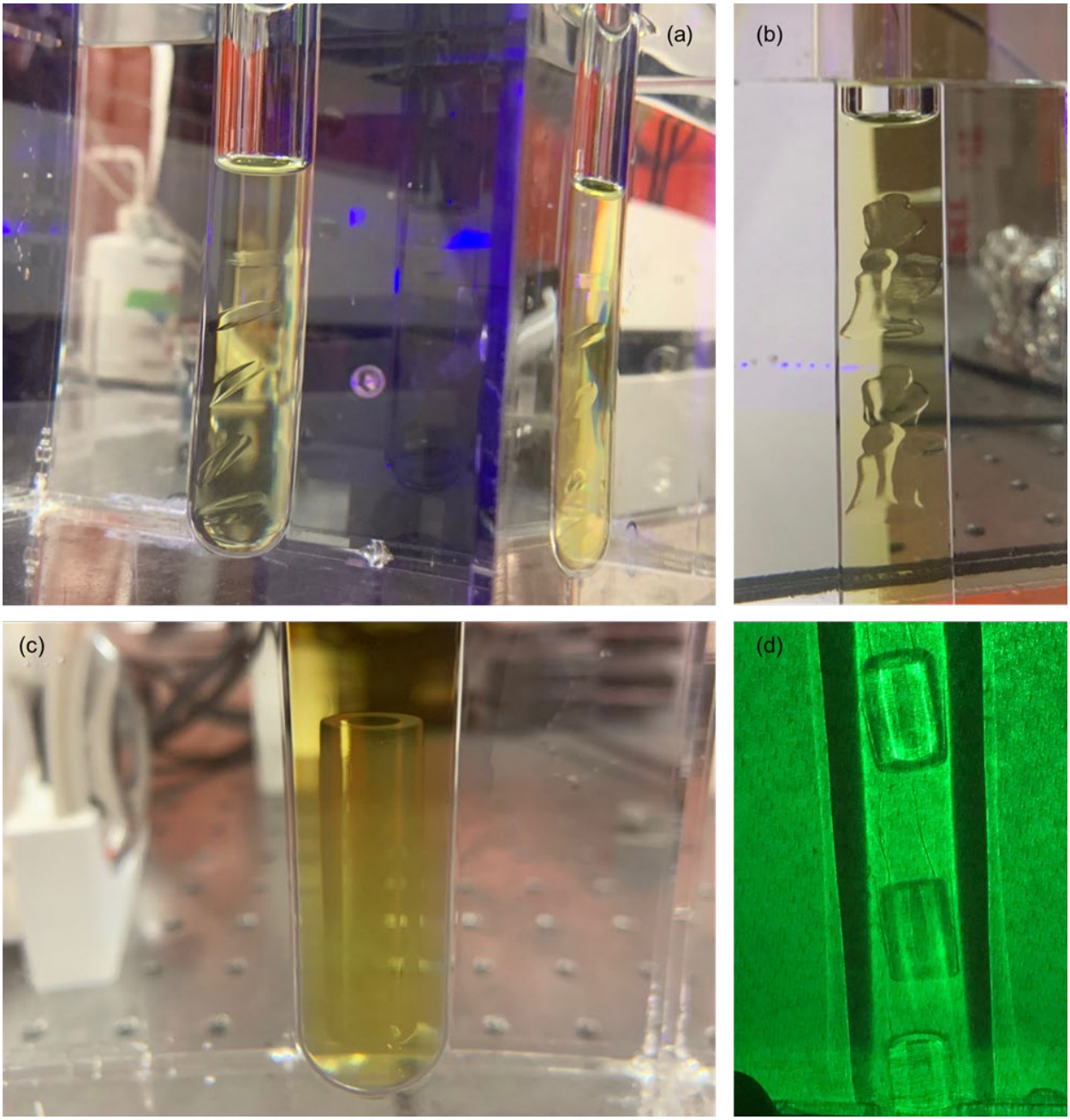

Figure 13 The sinking issue with engineering resins, and the ability to stack objects in the print volume with volumetric printing: (a) printing an array of plano-convex lenses. Sinking of the bottom lenses printed prior to the others can be easily observed in this image; (b) printing two thinkers in the same volume with vertical stacking; (c) a single tube printed in an engineering resin; (d) a shadow graph of a vertical array of the same tube geometry demonstrating the sinking problem with engineering resins, and the hardly visible streamlines showing how the surrounding space can be influenced be the displacement of objects throughout the print process.

Another interesting feature of CAL is the ability to volumetrically pack the objects in the build volume. The prints of Figure 13a, 13b and 13d demonstrate such capability in printing a vertical array of objects which is impossible with other AM processes that utilize two-dimensional packing on a flat print bed. As can be observed from Figure 13a and 13d, a critical problem that exists with

volumetric AM is the sinking of objects during the print process resulting from slight density change in the polymerization process. Firstly, it should be noted that this sinking only starts to happen after a certain degree of conversion has been reached and this typically only includes the last 10 to 20% of the print time. Hence, in most cases where the print is completed within less than half an hour this issue is almost negligible. Secondly, the use of resins with higher viscosities can help us overcome this challenge by increasing the drag forces exerted on the object and reducing the terminal sinking speed. Thirdly, this does not apply to the hydrogel compositions that we have chosen to work with. This is due to the thermal gelation step that was explained in Chapter 2 which provides a thixotropic environment throughout the print eliminating any sinking or displacement of the printed objects.

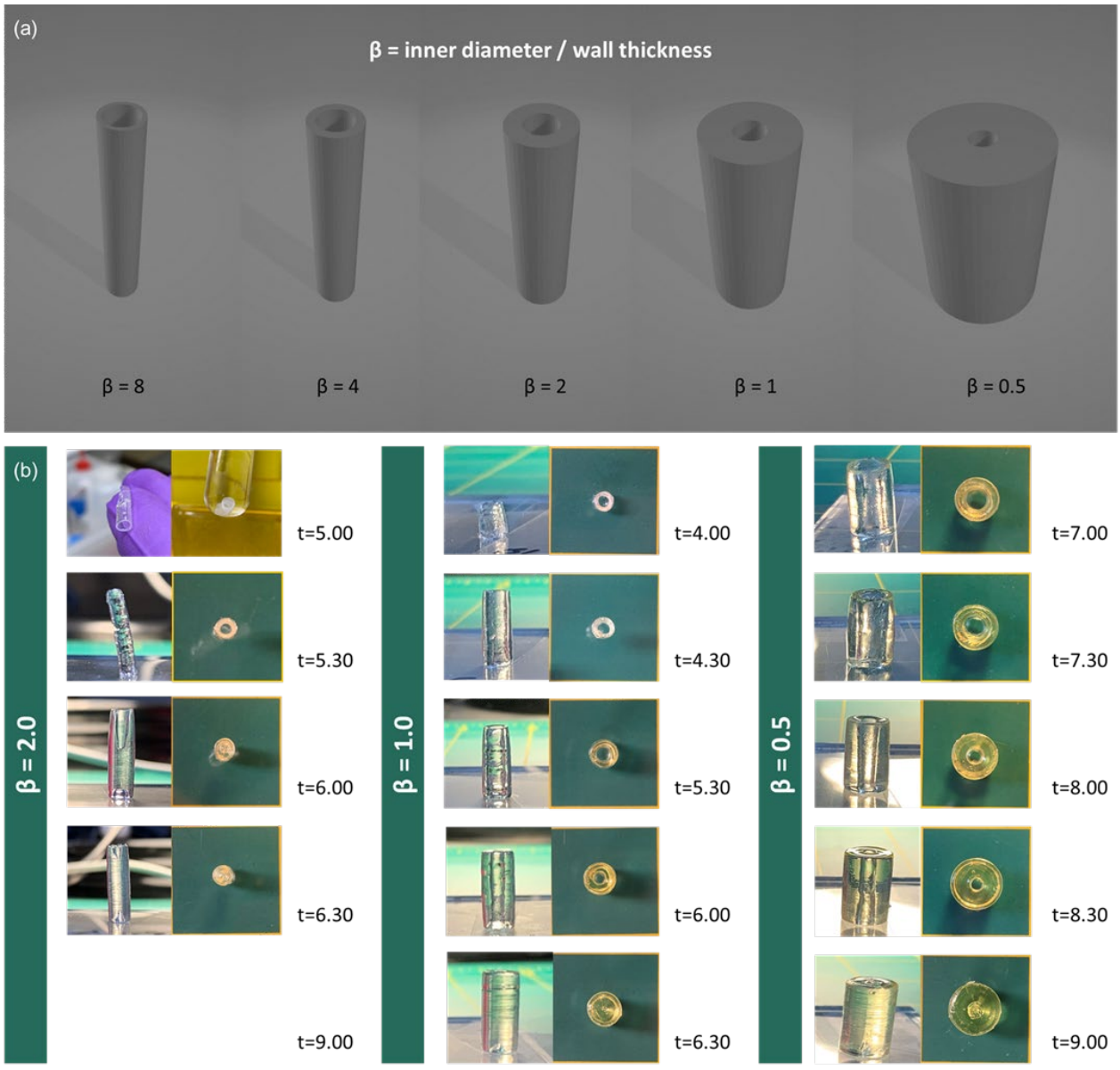

Figure 14 Varying the dimension-less beta parameter in the projection set, and exposure/print time to find the optimal combination: (a) graphical demonstration of the general effect of beta values on tube geometry; (b) experimental results of printing with different configurations.

To better understand the geometry-dependency of the process with respect to negative spaces and cavities, we defined a beta parameter that is the ratio of the tube inner diameter and wall thickness. As this parameter increases from zero to infinity, we transition from extremely isolated channels with bulky walls to very fine channels with thin walls. In the experimental scheme, projection sets were designed for various target beta values. The print duration was refined and varied across different experiments to achieve an optimal print termination time. It is observed that with a given projection set and target beta value, as the print time is increased, the object is over-cured. This over-curing which happens in the form of an increase in wall thickness, narrows down the inner

diameter of the channel and thus decreases the actual beta value. Hence, apart from the designed projection set, precise control of print time is crucial in achieving a perfusable structure.

Another important observation from this experiment is that achieving lower beta values is typically much easier than higher beta values. In fact, it wasn't possible to achieve beta values beyond $\beta = 2.0$ using the algorithm originally developed for CAL. Beyond $\beta = 2.0$, all printed tubes were clogged and hence are not reported in the results shown in Figure 14. To solve this problem, a clever modification was made to the optimization target to allow for better contrast in the volumetric dose distribution. Instead of a binary target that was conventionally used, where solid regions were given a value of one and the other regions zero, negative values were assigned to the internal cavity regions. In the original case, the target dose would be zero everywhere outside the desired solid object. While a negative dose cannot be delivered, this approach influences the projection generation algorithm to deliver lower doses in these critical voids than would be delivered with the conventional algorithm. A negative value that substitutes a zero in the dose target matrix has the effect of suppressing the values of line integrals along the rays that pass through the voids in the Radon transform and therefore increases the contrast in the backprojected dose distribution between the dose delivered in the solid and void regions.

The printed tubes of Figure 15a show the results obtained by implementing this negative target assignment in generating the projection sets with $\beta = 4.0$ that wasn't achievable prior to this. As can be seen in Figure 15d, the projections without this implementation suffered from a finite exposure in the void regions that resulted in a poor contrast in the backprojected dose distribution (Figure 15e). However, the modified projections shown in Figure 15b display a zero intensity in the center and a stark contrast in the backprojected dose distribution (Figure 15c). Hence, beyond this point all perfusable structures printed in this thesis utilize the modified version of the algorithm.

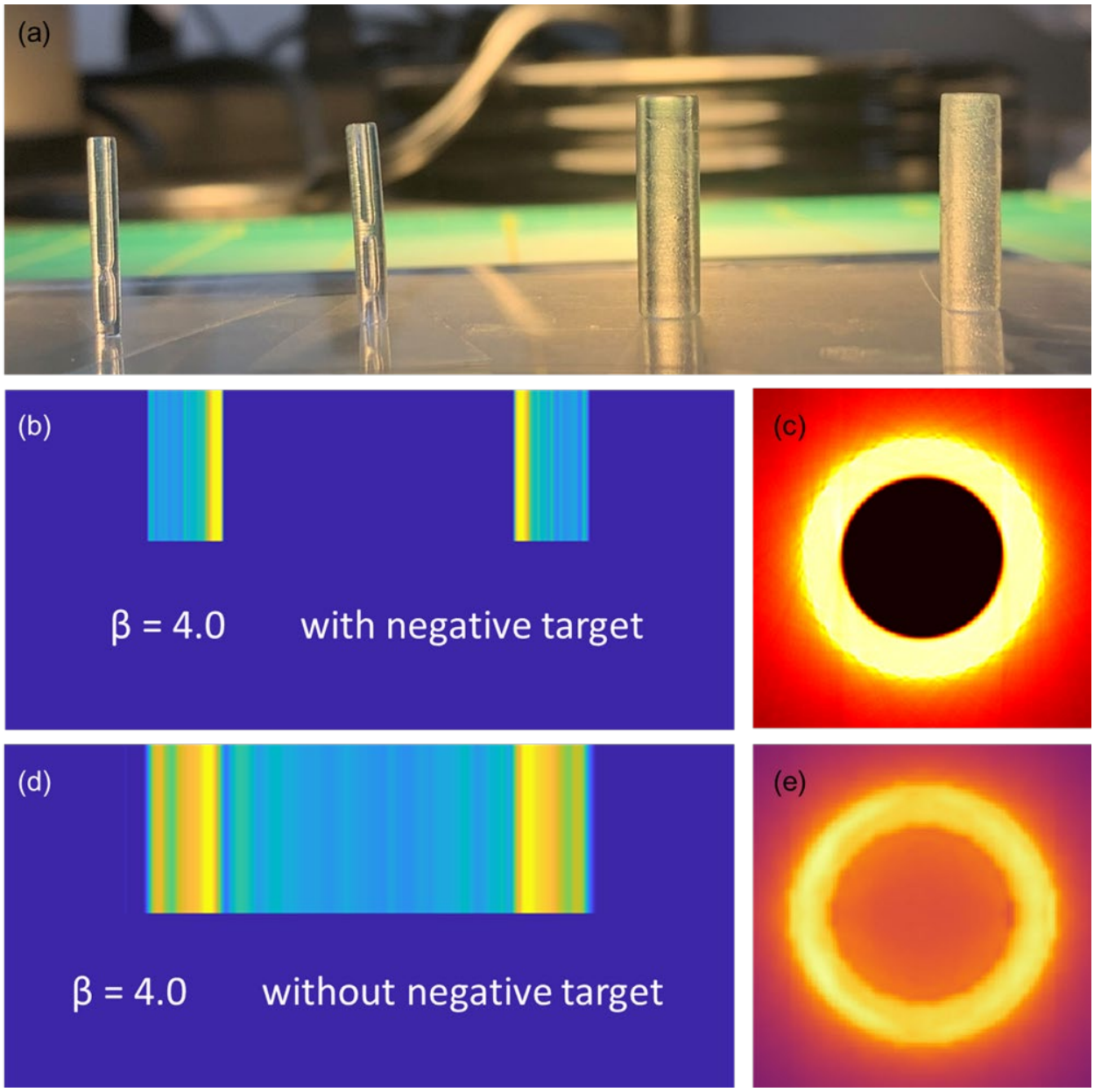

Figure 15 Implementation of the negative voids in the target improves dose distribution contrast and enables finer tubes with larger beta values to be printed with CAL: (a) tubes with β=2.0 and β=4.0 printed repeatably with the modified projection set shown in (b). (c) The backprojected dose distribution showing stark contrast in the cavity region whereas the original projection set shown in (d) suffers from poor backprojected dose distribution as displayed in (e).

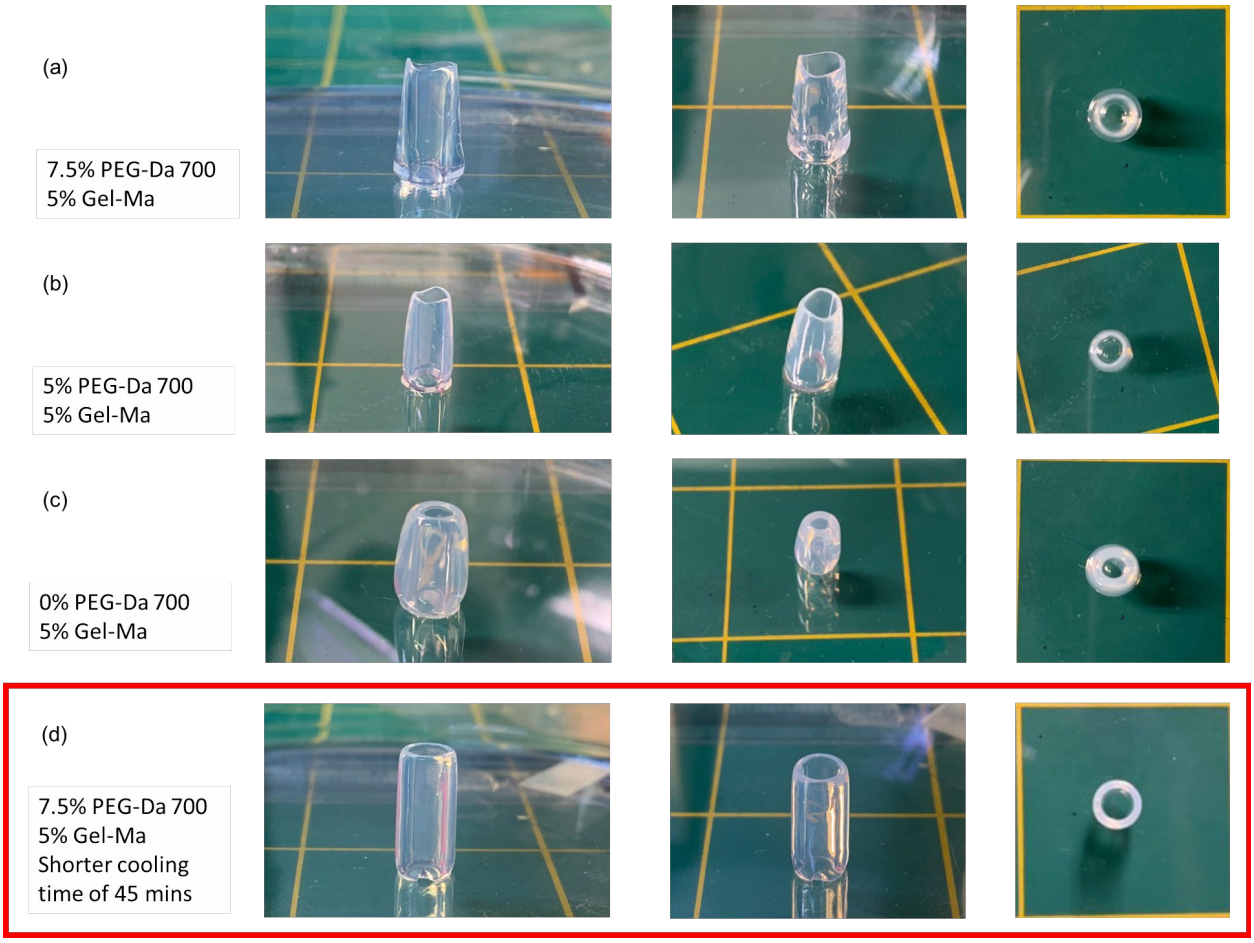

Figure 16 Perfusable structures printed in various hydrogel compositions: (a) tube printed in 7.5% PEG-DA 5% Gel-MA composition; (b) tube printed in 5% PEG-DA 5% Gel-MA composition; (c) tube printed in 5% Gel-MA only; (d) same structure of (a) without overnight cooling.

The next step was to demonstrate the printability of simple perfusable structures in hydrogels. The structures shown in Figure 16 demonstrate the results of printing a simple hollow cylindrical tube in various hydrogel compositions after an exposure time of 150, 270 and 300 seconds for the configurations shown in Figure 16 panel (a), (b), and (c) respectively, using the same projection set. Firstly, the print times for pure Gel-MA exceed that of composite hydrogels that also include PEG-DA in their composition. Increasing the PEG-DA content is also consistently observed to reduce print time. The second interesting observation was that despite using the same visual cues from the Schlieren imaging system, upon extraction the pure Gel-MA tube was more dilated and over-cured than the other tubes. This effect is very similar to the Gel-MA thinker of Figure 11. Another very interesting observation that was consistent across all compositions was the cone-like divergence of the tubes and the increase of wall thickness towards the bottom of the structures. We found the reason for this geometrical aberration to be as described in the following.

As explained in the second chapter, the thermal gelation of Gel-MA was utilized in order to hold and support the printed structure throughout the print process. Therefore, the temperature was

lowered to 2–8 °C to allow for the Gel-MA to thermally gel. The solubility of oxygen water has a strong dependency with temperature and lower temperatures allow for higher steady-state concentrations of oxygen. Since the Gel-MA is cooled down from a mixing temperature of 37 °C, it is subject to an inward diffusive flux of oxygen from the liquid-air interface at the top of the vial towards the bottom of the vial. This oxygen diffusion profile takes between two to three days to penetrate the 3 cm depth of the vials and flatten out. The two ways to achieve a uniform oxygen concentration is to either let the vials sit at lowered temperatures for that long, or to immediately use upon gelation so that the profile only penetrates a couple of millimeters of material depth. The procedure used in the case of structures shown in Figure 16a, 16b and 16c only involved an overnight cooling after which the gaussian diffusion profile was still present and hence the inhibition-controlled polymerization threshold of the hydrogel precursor varied as a function of material depth. As shown in Figure 16d, reducing the gelation time to 40 minutes resolved this issue and enabled a much more uniform wall thickness along the length of the tube.

Understanding some of the complexities associated with printing simple hollow channels, and implementing the algorithmic and experimental modifications tested previously, the geometrical complexity of the printed object was further increased to branched non-axisymmetric vascular architectures. To prove the generality of the printing capabilities of computed axial lithography, multiple perfusable geometries were designed, printed and evaluated for perfusability.

The first geometry that was tested was the Y-shaped bifurcation of Figure 17a printed in a hydrogel with a 7.5% PEG-DA and 5% Gel-MA composition using a projection set produced with the negative void target corrected algorithm. This structure as well as the structure shown in Figure 17b with a single inlet-single outlet configuration, demonstrate the possibility to print fully perfusable hydrogel structures with CAL. The perfusability of these structures was also confirmed although images of those experiments are not provided in Figure 17. Both structures were printed in slightly less than five minutes.

Following these prints, a more complex multi-vascular model that offers separate fluidic lines for transport of multiple solutions to/from the tissue compartment was printed in engineering resins (Figure 17c). The print took only eight minutes to complete, after which the vial was heated to 65 °C and the uncured resin was removed. The construct shown in Figure 17d is another good example of achievable geometrical complexities with CAL. In this case a triple-layered branched architecture was printed in engineering resins. The channel sizes range from 2 mm in the first level to 0.9 mm in the third level. In Figure 17, a single frame of the projection sets used to print these objects has also been included. The dark cavities and interiors of the channels and the stark contrast in the edges will further translate to a better backprojected dose distribution in the resin volume.

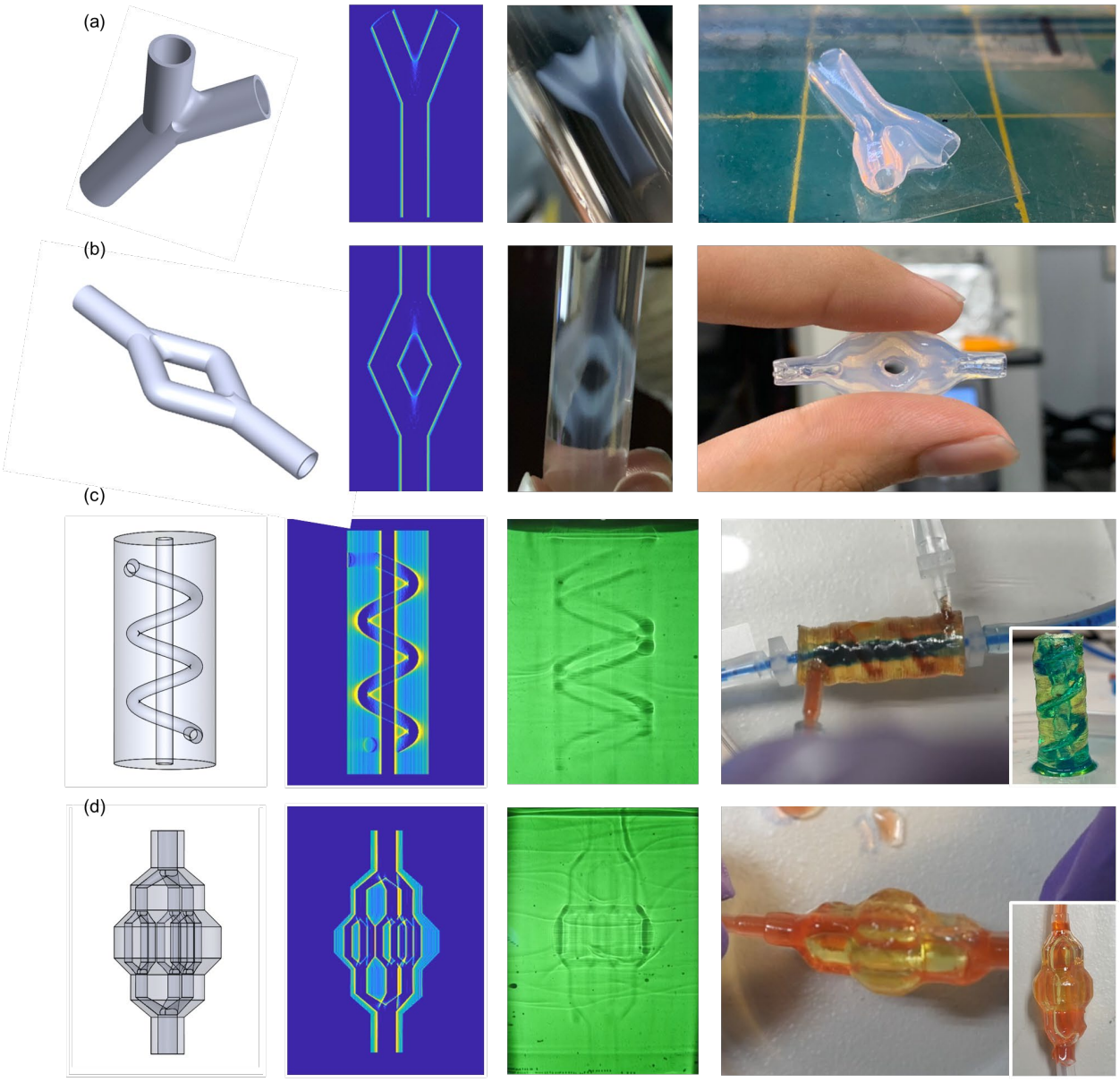

Figure 17 Printing complex non-axisymmetric perfusable structures with computed axial lithography: (a) a Y-shaped bifurcation printed in 7.5% PEG-DA 5% Gel-MA; (b) a similar branched structure with a single inlet and outlet printed in the same hydrogel composition; (c) a multi-vascular architecture with a straight and spiral channel printed in engineering resins; (d) a triple-level branched architecture also printed in engineering resins.

The same multi-vascular and branched geometries of Figure 17c and 17d were printed with the 3% Gel-MA composition and are displayed in Figure 18. Although the emergence of the object was hardly observed in the Schlieren images, due to the low sensitivity of the imaging system to such minor changes in refractive index that happen in the case of the case of extremely low Gel-MA concentrations, the print termination timing was not perfect and hence many of the channels were clogged and over-cured and only the central channels were perfusable. However, the intricate internal structure of the channels can be seen in the images shown in Figure 18b, 18d, and 18e

where the object is immersed in a PBS solution. This further supports the existence and emergence of these fine features during the print process.

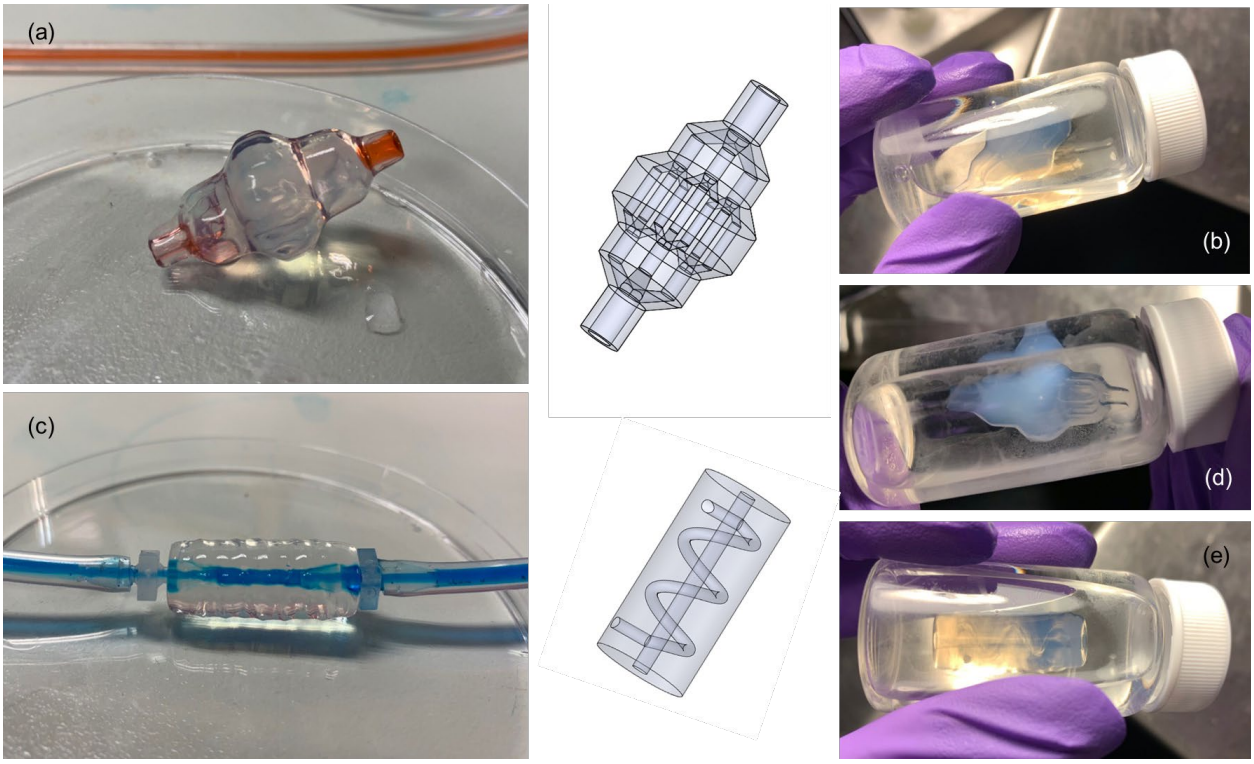

Figure 18 The multi-vascular and triple-level branched vascular structures of Figure 17 printed in 3% Gel-MA: (a), (b) and (d) the triple-level structure; (c) and (e) multi-vascular structure with a helical and a straight channel.

4.5. Biocompatibility of fabricated constructs

A conventionally used metric for biocompatibility of synthetic and natural hydrogel compositions is the cell viability of three-dimensionally embedded cells that are cultured within the gel and at a specific distance from immediate exposure to media. This value is typically high (more than 90%) for two-dimensional cultures, however the use of a three-dimensional culture environment and immobilization of the cells within a gel matrix can significantly reduce cell viability. This can be a result of the low diffusivity of the gel, lack of cell-adhesive ligands, and lowered mobility of the cells within the microenvironment or may even be a consequence of the fabrication technique and the cytotoxic conditions or species used in the different steps of the process.

Cell viability was separately assessed for SY5Y cells (Figure 19a) and HMECs (Figure 19b) after seven days in 3D culture in a variety of agarose-collagen gel compositions. In the absence of collagen, the hydrogels elicit relatively poor viability—less than 60%—from both cell types. Increasing the collagen content to intermediate concentrations of 0.05–0.1% w/v raises cell viability for both cell lines to 70–85%. Interestingly, however, further increasing the collagen

concentration to 0.2% w/v reduces cell viability again, in some cases resulting in lower viability than if collagen were entirely absent.

The existence of an optimal collagen concentration may result from a competition between two effects. On one hand, it has been shown by Balgude [61] and many others that softer microenvironments—which are provided by lower polymer concentrations—favor cell mobility and proliferation freedom. On the other hand, mechanosensitive pathways such as MAPK influence proliferation, migration, and differentiation, and their activation depends on the there being a high enough density of adhesive protein sequences in the ECM for focal adhesions to form and transmit forces between the nucleus, the cytoskeleton, and the surrounding ECM [76] [77]. Collagen provides these adhesive proteins, but increasing its concentration also increases stiffness.

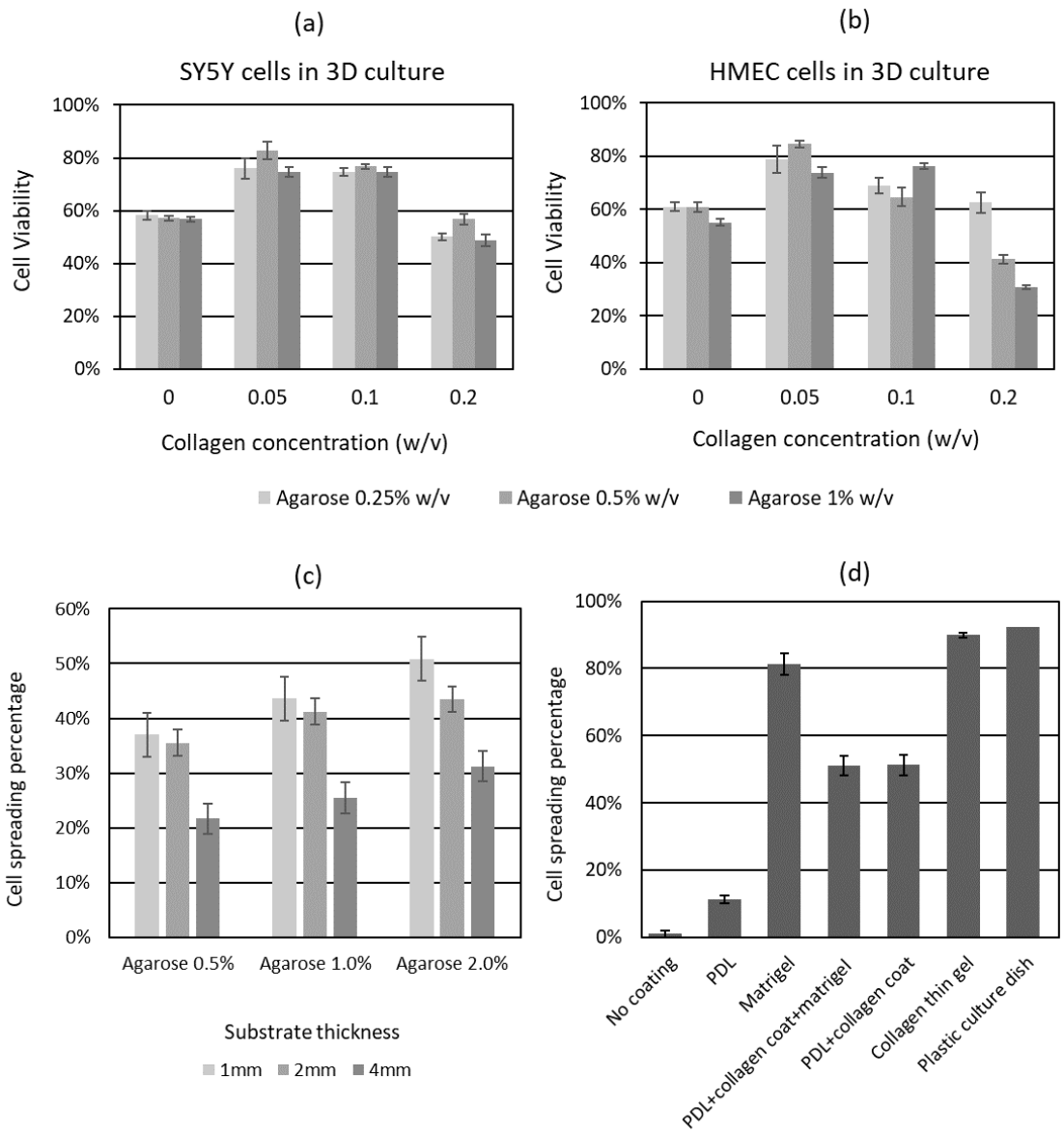

Figure 19 Cell viability and spreading analysis. Viability values are shown for (a) SY5Y cells and (b) HMECs in 3D culture with varying agarose and collagen concentrations after seven days in vitro. Spreading results are evaluated as the percentage of HMECs exhibiting a clearly non-spherical shape and/or one or more filopodia after two days in vitro, depending on (c) substrate thickness and agarose content (collagen concentration is zero), and (d) surface coatings on a 2 mm-thick hydrogel layer with 0.5% agarose and 0.05% collagen. Error bars show ±1 standard error of the mean, based on a sample size of four. Reproduced from Heidari and Taylor *[67]*.

Viability may be further compromised at higher collagen concentrations by the apparent tendency of the material to reorganize itself into larger fibers (Figure 9c–f). In addition to increasing stiffness, the reorganization into thicker fibers may be expected to result in lower surface-to-volume ratios, which could hide a larger fraction of adhesive proteins from the cells in culture. Overall, the results show an optimal concentration of 0.5% w/v agarose and 0.05% w/v collagen,

at which the seven-day viability values for the SY5Y and HMEC lines were 83% and 85% respectively. These values indicate the suitability of such a gel for 3D culture of both cell lines.

4.6. Cell-embedded biofabricated constructs

For the cell-embedded prints, as described in Chapter 2 the microvascular HMEC cells were uniformly mixed with the hydrogel precursors. They were immediately cooled down and transferred to the printer. In order to study the possibility of vascular network formation in different gel compositions, stacks of cylindrical tablets were printed in Gel-MA 3% and PEG-DA 7.5% + Gel-MA 5% hydrogels as shown in Figure 20a and 20b.

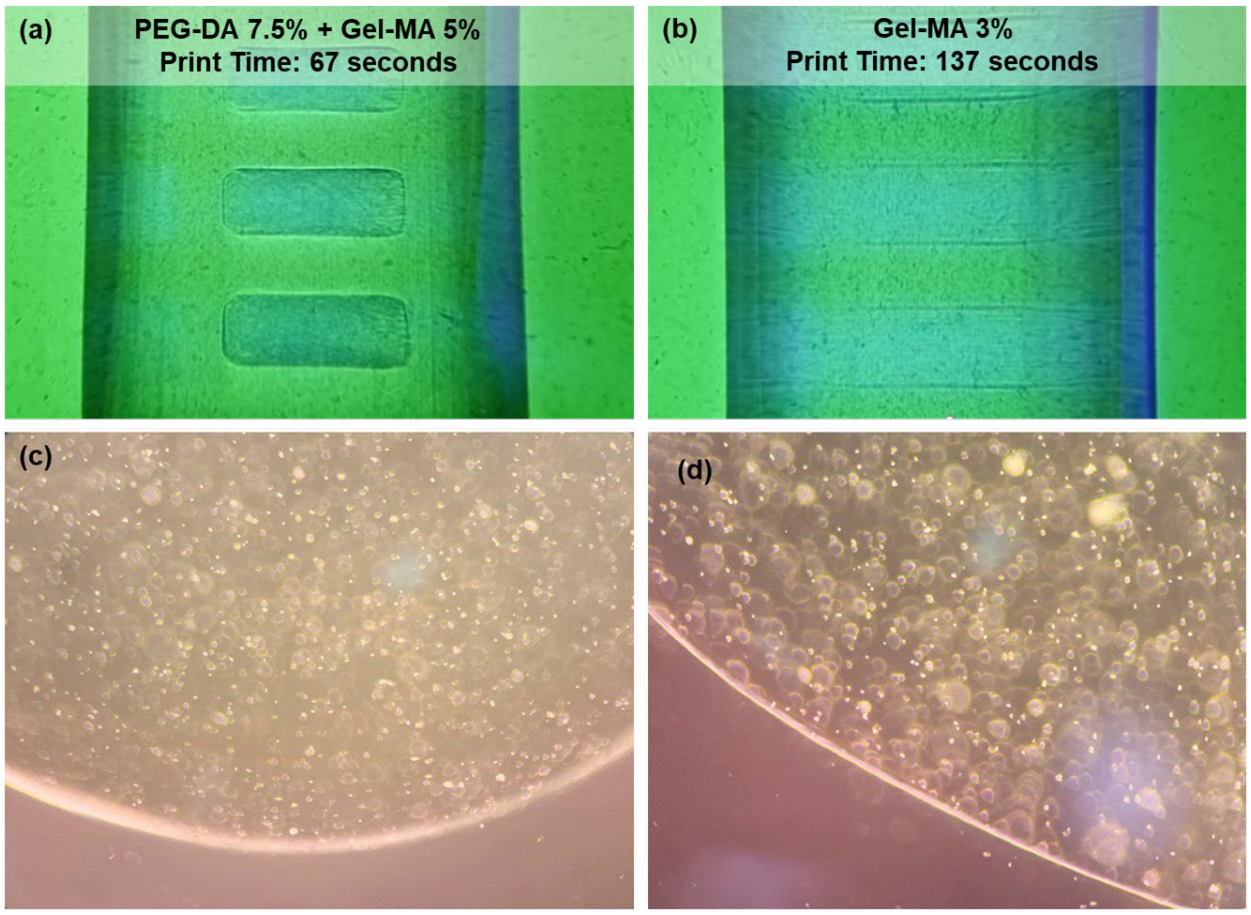

Figure 20 Printing small cylindrical tablets with cell-embedded hydrogels using computed axial lithography: (a) a vertical stack of tablets printed in a composite hydrogel with 7.5% PEG-DA and 5% Gel-MA; (b) same stack printed in a pure 3% Gel-MA hydrogel; (c) and (d) micrographs of the tablets printed in the previously mentioned composite and pure hydrogels respectively.

HMEC microvascular endothelial cells embedded at a high density within these tablets can be seen as bright spots in Figure 20c and 20d. After the completion of the print, the samples were processed in a sterile environment where the uncured surrounding mixture was recovered, and the tablets

were transferred to 12-well plates for the purpose of incubation and culture. In the next section we will examine the vascular networks obtained after weeks of culture.

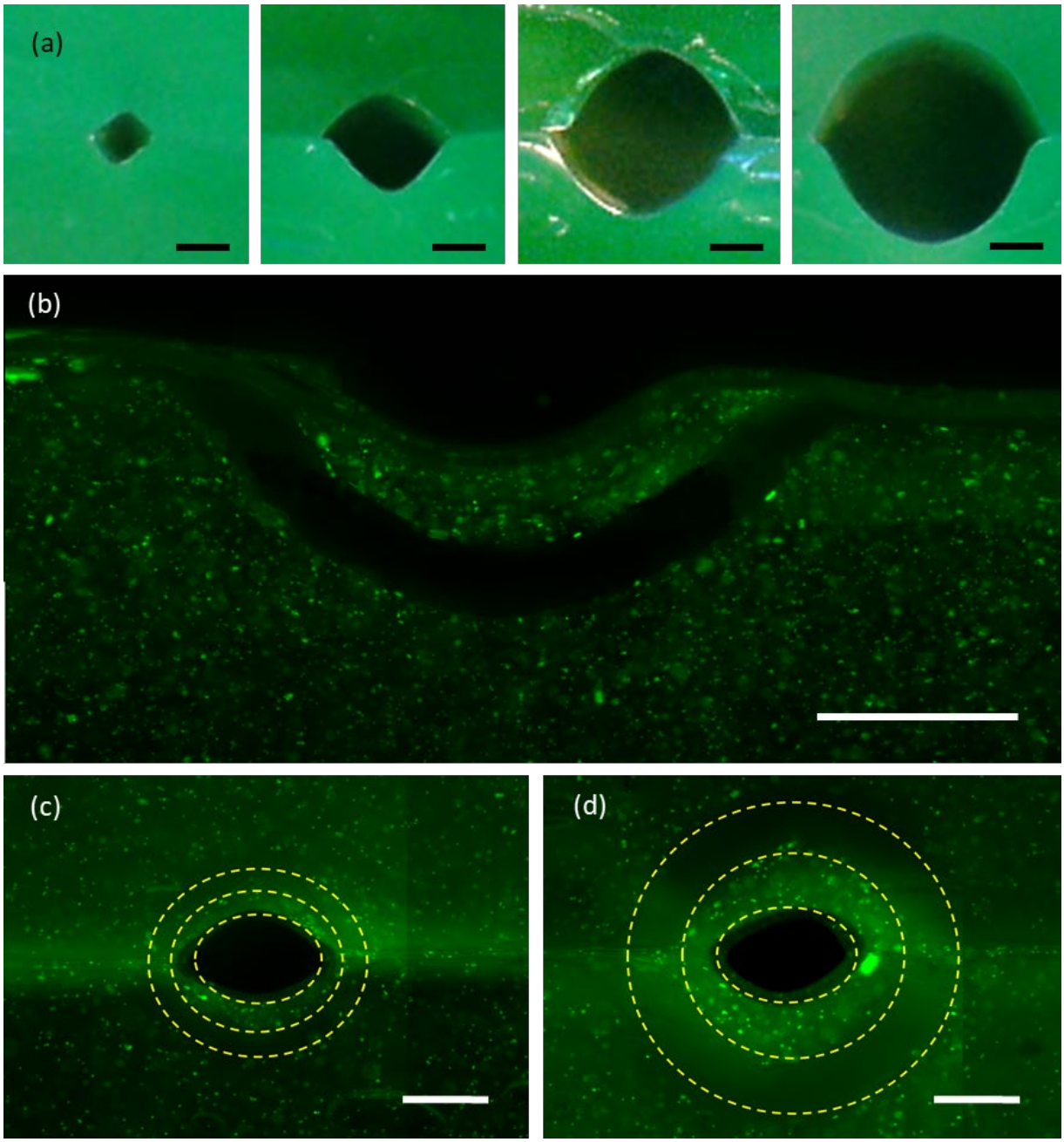

Figure 21 Cell embedded multi-layered structures produced with multi-layered micro-casting: (a) optical micrographs of cross-sections through molded channels with diameters varying from 400–2000 µm: hydrogel is dyed green. (b) Close-up view of a tri-layered construct with 500 µm inner diameter and cell-laden layer thickness of 250 µm, before binding to its opposite half. Fully enclosed channels are formed with 500 µm inner diameter and SY5Y-laden layer thicknesses of (c) 125 µm and (d) 250 µm. Adapted from Heidari and Taylor *[67]*.

For the micro-casting process, a similar scheme was used with glial SY5Y cells. As explained in Chapter 2, cells were loaded in the gel precursors and the mixture was then molded using the process explained in Chapter 3. Firstly, we confirmed an ability to produce sub-millimeter enclosed channels in the cast hydrogels. Molds were printed with semi-cylindrical protrusions having various diameters. With these molds, a single casting step was carried out with 1% w/v agarose solution to produce each half of a hydrogel construct, yielding vessel diameters from 400 to 2000 μm (Figure 21a). FITC fluorescent green dye was mixed into the gel prior to casting the samples shown in Figure 21a, to aid visualization.

4.7. Three-dimensional growth of endothelial and glial cells within the gels

Next, we monitored the proliferation, colonization and growth of our embedded cells and their ability to vascularize the surrounding hydrogel environment. For this purpose, the printed hydrogel tablets were cultured in a media-rich 37 °C incubator environment for four weeks. These cellular hydrogels were imaged every few days and the brightfield micrographs of these samples at different points of the culture period are shown in Figure 22.

The cell concentrations in both compositions were equal. Hence, immediately after the gels were printed and during the first 24 hours no visible differences were observed. However, after only a week of culture, endothelial sprouts and stretched actin structures had started to emerge and were broadly observed throughout the 3% Gel-MA prints (Figure 22b). The 5% Gel-MA 7.5% PEG-DA composite however didn't show any signs of cellular aggregates or colonies (Figure 22a). After 11 days of culture, the 3% Gel-MA constructs showed a tremendous density of multi-cellular networks and colonies spanning 200 μm distances (Figure 22d), whereas the cells cultured in the composite hydrogel were still isolated and singular (Figure 22c). After two weeks of culture, the networks previously observed in the 3% Gel-MA prints had already spun distances of over 500 μm displaying astonishing branched capillary networks such as those shown in Figure 22f and the fluorescent and confocal images shown in Figure 23. These remarkable organic networks only emerged in this specific composition and neither of the Gel-MA+PEG-DA composites nor the higher concentration 5% Gel-MA prints were able to cultivate such networks. The 5% Gel-MA hydrogels gradually displayed extended actin structures and slightly better cell spreading but no cellular networks were observed in the four-week culture window.

These results further confirm the significance of mechanical properties such as matrix stiffness in determining the fate of endothelial cell networks embedded in the gels. The cell motility and ability to extend its filopodia and migrate within the gel as well as its ability to extend its actin structures and communicate with neighboring cells by spreading within the microenvironment are key factors in forming a confluent tissue structure.

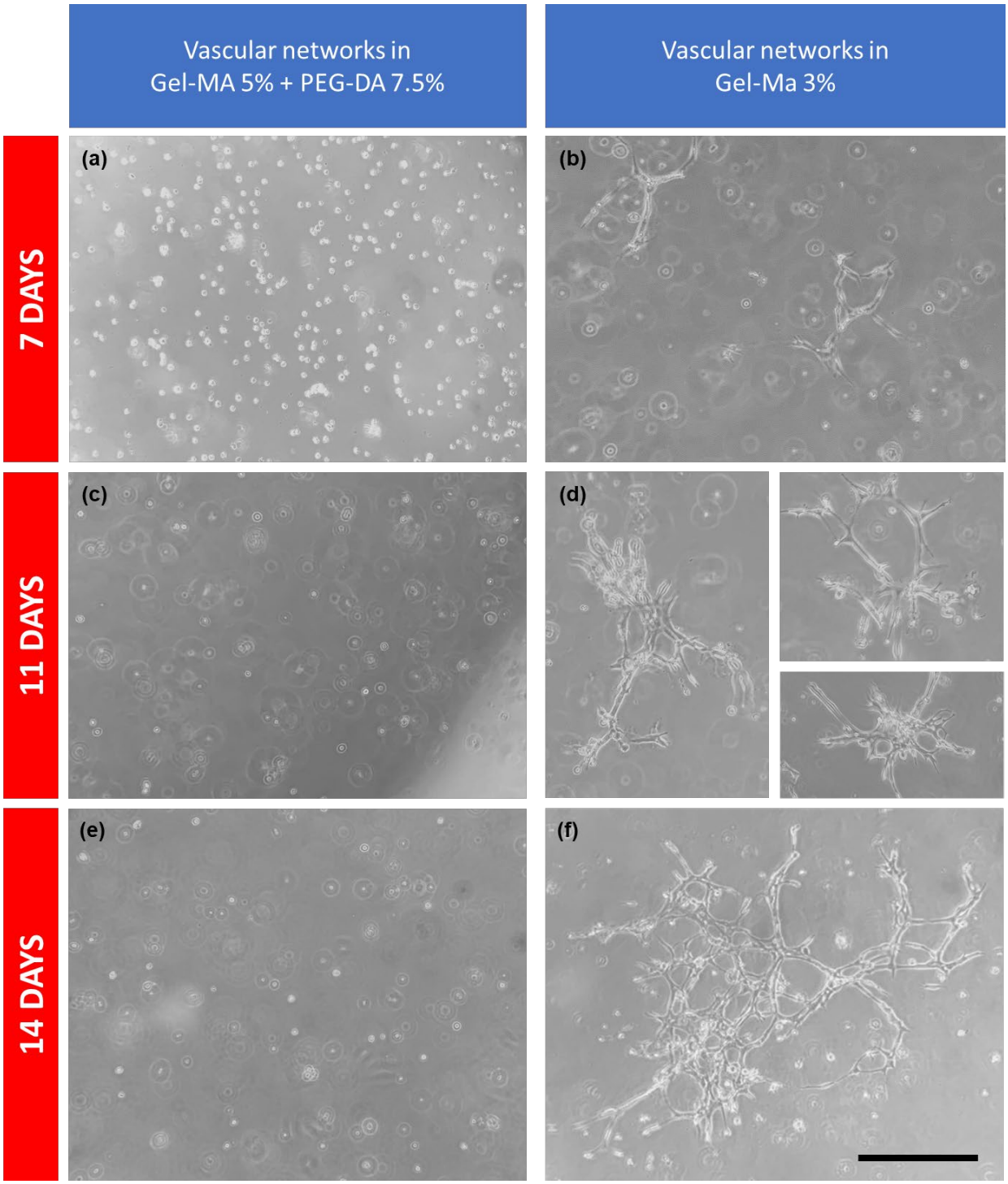

Figure 22 Microvascular endothelial networks emerging within the hydrogel prints: (a), (c) and (e) the growth of endothelial cells within the 3% Gel-MA 7.5% PEG-DA composite gels imaged after seven, 11 and 14 days of culture. Samples do not show any form of cellular extensions and network formation, and the cells are isolated even after two weeks of culture; (b), (d) and (f) show images of the pure 3% Gel-MA composition taken at the same time intervals. These samples however show exceptional network formation and colonization after only a week of a culture. Networks easily span distances of 500 µm after two weeks. Scale bar is 200 µm and can be used for all sub-figures.

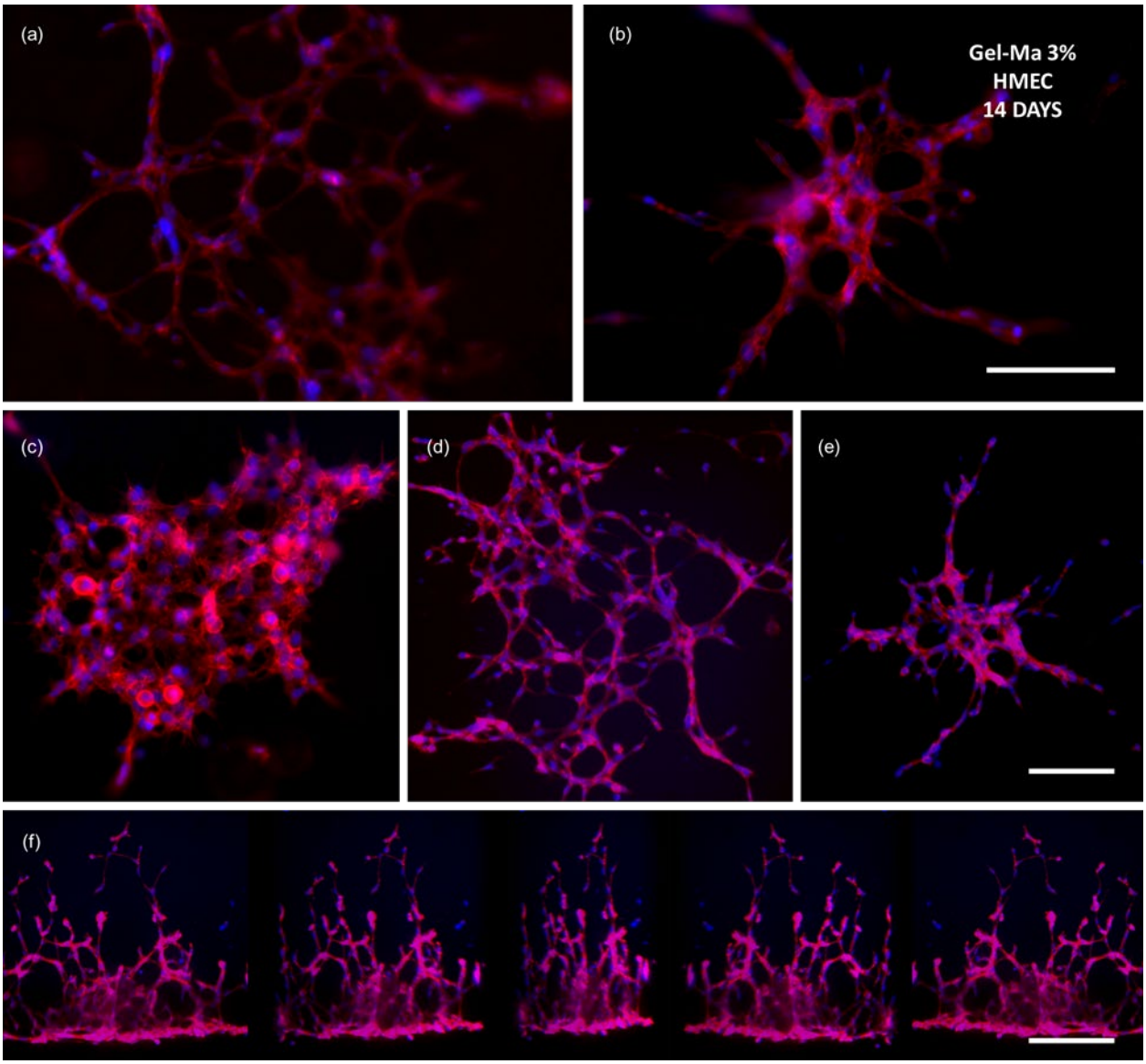

Figure 23 Microvascular endothelial networks in 3% Gel-MA prints after two weeks of incubation: (a) – (e) examples of such organic networks spanning distances of over 500 µm within the hydrogels; (f) projections of endothelial networks emerging from a gel-media interface. Scale bars are all 200 µm and are common among the sub-figures of each row. Staining: red: actin, blue: nuclei.

For the multi-layered micro-casting process, the embedded cells were glial SY5Y cells and hence the colonization and growth of these cells in 3D agarose-collagen hydrogel matrices with varying compositions were monitored (Figure 23). As the agarose concentration is increased from 0.25% w/v to 1.0% w/v, less proliferation is seen after seven days in culture (Figure 23a–c). Moreover, at the lower agarose concentrations the 3D clusters of cells tend to be larger (Figure 23d–f), and neurite extensions tend to be longer (Figure 23g–i). Since lower agarose concentrations have been shown to correspond to lower elastic moduli (Figure 19), these results are consistent with the idea that more compliant microenvironments promote proliferation and mobility [78]. Nevertheless,

the strength of the effect of agarose concentration on proliferation, cluster size and neurite growth is striking when it is considered that the seven-day viabilities of SY5Y cells remain within the reasonably narrow band of 70–85% for the same range of material compositions: 0.05% w/v collagen and 0.25–1.0% w/v agarose (Figure 19).

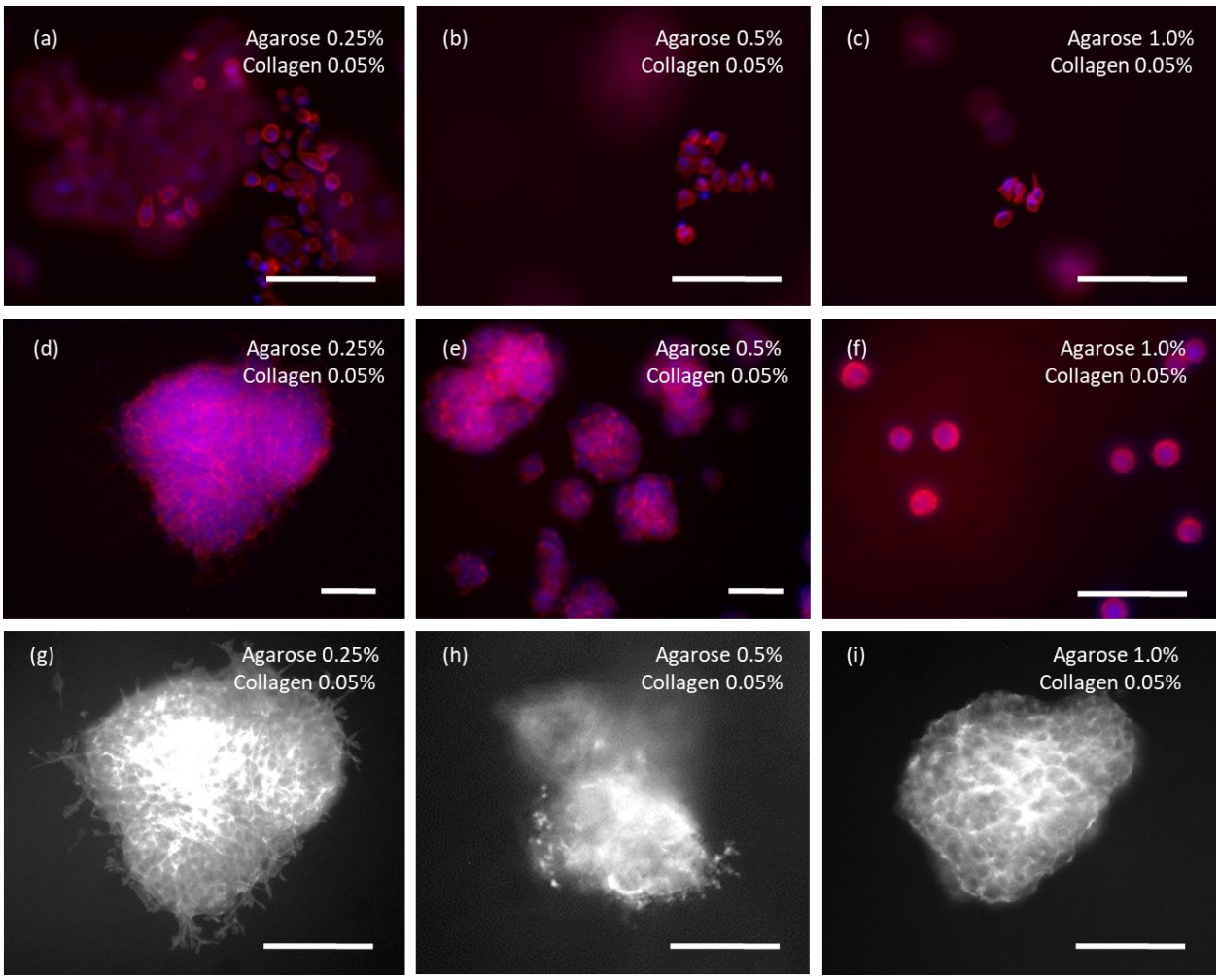

Figure 24 Expansion and colonization of SY5Y glial cells within 3D agarose–collagen hydrogels: (a–c) overall trend of cell population reduction with the increase in agarose concentration from 0.25% (a) to 1% (c); (d–f) decrease in size of cellular clusters with the increase of agarose concentration from 0.25% (d) to 1% (f); (g–i) decrease in length of neurite extensions with the increase of agarose concentration from 0.25% (g) to 1% (i). Scale bars are all 50 µm. Staining: (a–f): red: actin, blue: nuclei; (g–i): actin. All samples were fixed after seven days in culture. Adapted from Heidari and Taylor *[67]*.

4.8. Two-dimensional growth of endothelial lumens on hydrogel surfaces

An ideal *in vitro* vascular model should be able to combine these spectacular bottom-up micro-capillary networks with top-down millimeter scale blood vessels that act as arterioles carrying the

flow to the capillaries and collecting it on the other side. Hence, to complete the model we need to cover the larger biofabricated channels with a confluent monolayer of endothelial cells with adequate adhesion to the surface of the hydrogel ECM. To this end, we have studied the 2D spreading behavior of HMECs on agarose-collagen hydrogels, including with a range of candidate coatings.

We first consider uncoated layers of purely agarose gels with no collagen content and thicknesses between 1 and 4 mm (Figure 19c). These hydrogel layers were deposited onto relatively rigid polystyrene culture surfaces. Cell spreading after two days *in vitro* is defined as the percentage of cells exhibiting a clearly non-spherical shape and/or one or more filopodia. Higher spreading percentages occur with higher agarose concentrations and thinner layers, both of which can reasonably be supposed to make the hydrogel surface appear stiffer to the HMECs, enhancing migration. A high spreading percentage does not, on its own, confirm that a confluent monolayer has formed or could form. Neither does it provide direct information about proliferation; it simply shows a propensity of the cells to migrate laterally on a surface, which may ultimately assist monolayer and tight junction formation. In fact, the purely agarose gels did not exhibit confluent monolayer growth after two days, so we investigated the use of coatings following the methods in Chapter 2. For these tests, a 2 mm-thick base gel of 0.5% w/v agarose and 0.05% w/v collagen was used.

The first coatings that were experimented with were the hFN coating and type 1 rat-tail collagen applied separately, HMECs were found not to attach to these surfaces at all. Meanwhile, a PDL coating dispensed at a concentration of 0.25 mg/mL resulted in just 11% spreading cells after two days (Figure 19d and Figure 25d). However, when the PDL deposition was followed by either the rat-tail collagen coating or by both rat-tail collagen and 0.2 mg/mL Matrigel coatings in that order (inspired by the work of Han *et al*. [79]) the spreading fractions increased to approximately 50%. These multi-material coatings in fact resulted in the greatest apparent surface coverage and confluence of HMECs after two days.

The simple application to the base agarose–collagen hydrogel of a Matrigel coating from a 0.2 mg/mL solution (without a preceding PDL deposition) or of a bovine type 1 collagen treatment from a 5 mg/mL solution (Figure 25e) resulted in even higher two-day spreading percentages: 81% and 90% respectively. They did not, however, correspond to as extensive HMEC surface coverage after two days as was seen with the PDL/rat-tail collagen and PDL/Matrigel/rat-tail collagen coatings. It makes sense that the highest spreading percentages would not necessarily correspond to the greatest confluence at a specific time, because once a layer has become confluent and cells are in lateral contact with each other, they can be expected to cease or reduce their spreading. From these results we find that, of the coatings tried, the multi-material treatments provide the best option to induce rapid confluence of HMEC monolayers.

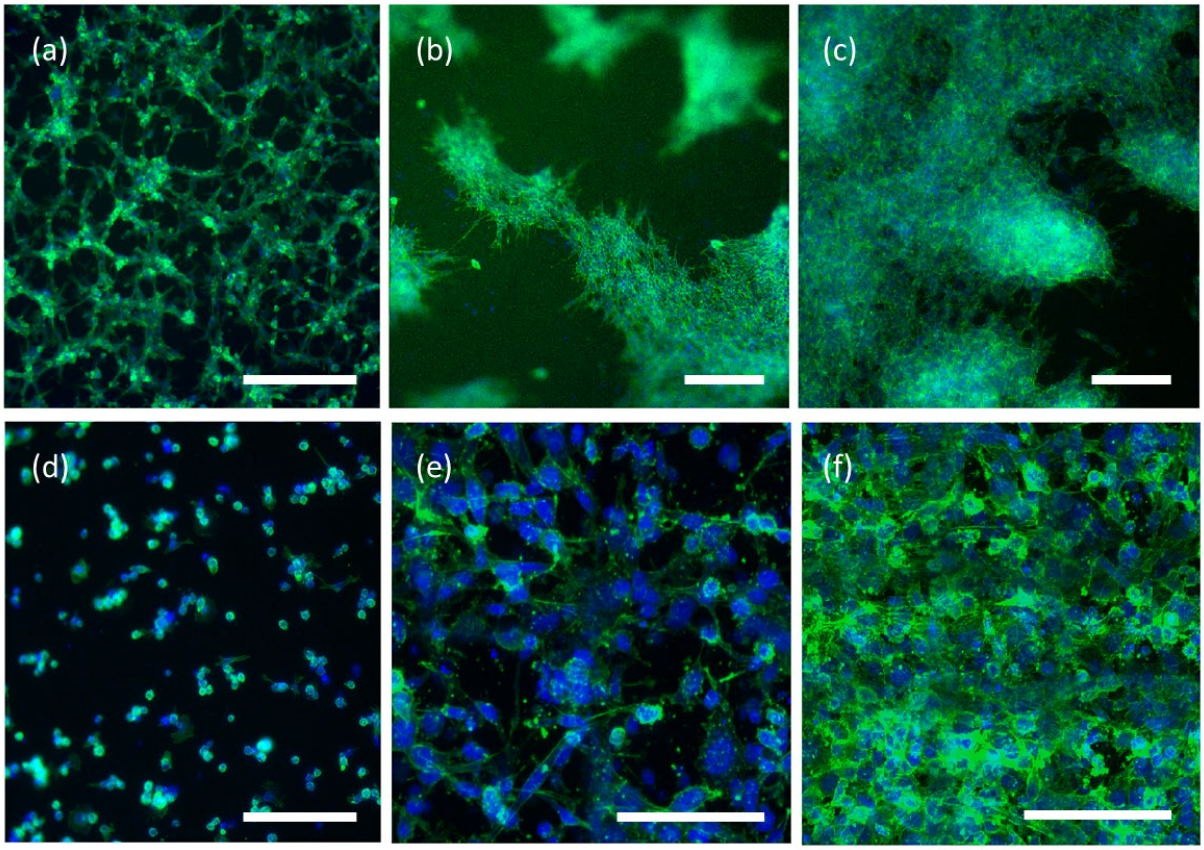

Figure 25 Effects of modulating the surface adhesion properties of the agarose–collagen hydrogel for SY5Y and HMEC cells. Adhesion of SY5Y cells on the optimal coating (0.1% w/v PDL) on the optimal substrate (2 mm-thick layer of 0.5% agarose and 0.05% collagen): (a) cell adherence after one day in vitro; (b) accumulation of cells on the surface after two days in vitro; (c) presence of a bovine type 1 collagen coating on top of the PDL enabling stable attachment of the layer of cells even after three days. Adhesion of HMEC cells on different coatings: (d) PDL coating found to be unsuitable for HMEC cells; (e) best cell spreading achieved using a bovine type 1 collagen coating; (f) the same configuration as (e), but with the addition of 3D-cultured SY5Y cells in the gel underneath the endothelium, substantially improving surface coverage and area confluence. All scale bars: 100 µm. All images: green stain: actin; blue stain: nuclei. Reproduced from Heidari and Taylor *[67]*.

The above results show that the two different types of collagen coating have elicited rather different HMEC behavior: while the rat-tail collagen coating on its own enabled negligible adhesion, the bovine collagen coating yielded some of the highest spreading percentages. A plausible explanation, other than the differing source of the material, is that the rat-tail collagen was supplied at an acidic pH and was diluted but not fully neutralized before deposition, likely inhibiting significant gelation on the surface. The bovine collagen was supplied at near-neutral pH and may have been able to form a more substantial gel coating during the one-hour incubation period. We also found that rapid formation of a confluent HMEC monolayer can be promoted by the proximity of SY5Y cells in 3D culture in the hydrogel base layer beneath the developing monolayer (Figure 25f). This finding is encouraging, because in a neurovascular model, an HMEC monolayer grown on the inner surface of the cast lumen is indeed surrounded by glial cells in 3D culture. While glial cells would typically be grown in 3D, we did also study the 2D growth of

SY5Y cells on a 2 mm-thick layer composed of 0.5% w/v agarose and 0.05% w/v collagen, treated with the range of coatings described in Chapter 2. The only coatings that facilitated SY5Y attachment were PDL and PDL/bovine collagen. Favorable adhesion and spreading of SY5Ys were observed for up to two days on a PDL coating that had been deposited from 0.1 mg/mL solution (Figure 25a–b). After the second day of culture, however, the SY5Ys tended to separate from the purely PDL-coated substrate. This tendency can be attributed to over-confluence of the layer and breakage of the adhesion complexes as a result of layer expansion. The addition of a bovine collagen coating from 5 mg/mL solution on top of the PDL gave better stability to the layer of cells at later stages of culture (Figure 25c).

Finally, devices were produced with an integrated endothelial monolayer, bringing together the ingredients of a plausible neurovascular model. These devices involved a simplified casting sequence. The outermost layer of the construct, with an inner diameter of 1 mm, was again made of a 0.5% w/v agarose, 0.05% w/v collagen AC composite gel, and was populated with 5×10^5 cells/mL SY5Y cells. An intermediate layer with an inner diameter of 0.5 mm—and hence a layer thickness of 250 μm—was then cast from a mixture of 0.5% w/v agarose and 0.5% w/v collagen in which had been suspended 5×10^6 SY5Y cells/mL. The higher collagen concentration of 0.5% w/v in this intermediate layer was chosen because, although viability and proliferation would not be expected to be as high as in the optimal 0.05% w/v case, it was expected to provide a somewhat stiffer gel with greater cell-spreading potential during endothelialization, analogous to the results for finite-thickness gels shown in Figure 19c.

To promote cell spreading further, a bovine type 1 collagen coating was then deposited onto the inside surface of the lumen, following the protocol of Chapter 2. Bovine collagen was applied because, when used with SY5Y cells cultured within the underlying gel, it had been found to support excellent HMEC spreading and confluence (Figure 25f). HMECs were then seeded inside the lumen from a suspension of 8.4×10^5 cells/mL. After being incubated at 37 °C in a humidified 5% CO_2 atmosphere for 24 hours, surplus HMECs were rinsed out from the channel with fresh medium, and incubation continued for a further three days before the structures were fixed and imaged.

A 3D image of the resulting triple-layered lumen was constructed via fluorescence confocal microscopy, and several projections of it are shown in Figure 26a and 26b. The majority of the cells in these images are the HMECs lining the lumen. The SY5Y glial cells in the intermediate cast layer can be seen scattered in the region around the lumen. The SY5Y cells in the outermost cast layer have a lower density than those in the intermediate layer and hence appear very sparsely in the images.

To verify that the inner layer is actually a confluent endothelial monolayer with BBB-like integrity, intercellular tight junction proteins ZO-1 were stained and imaged. The top view of a horizontal slice through the lumen of Figure 6k is shown in Figure 26c, and it reveals strong ZO-1 expression, indicating the formation of a tightly packed endothelial monolayer after three days *in vitro*.

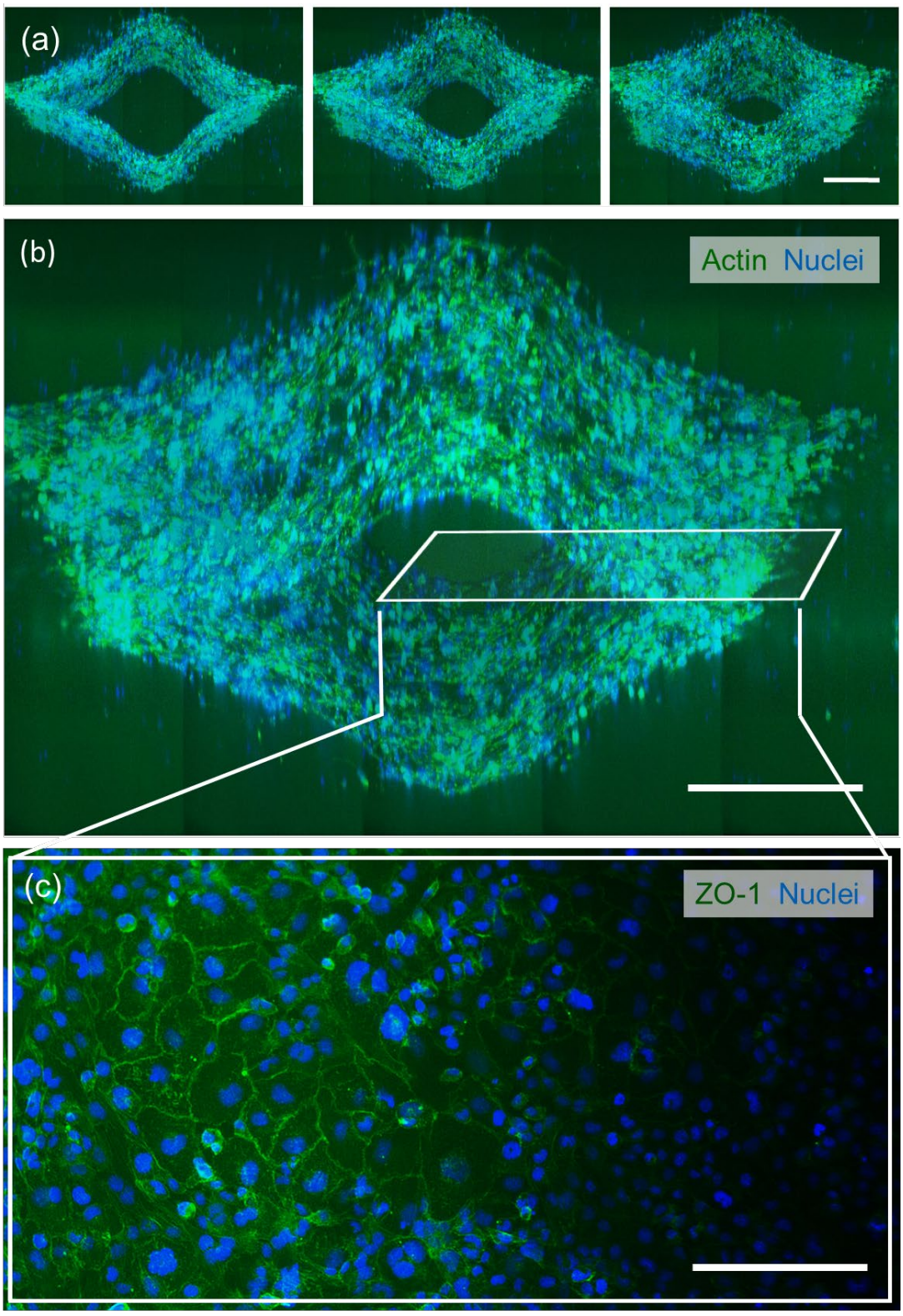

Figure 26 Fabricated 3D vascular construct: (a) projections of endothelia with glial cells surrounding the lumen; (b) enlarged view of the same lumen; (c) ZO-1 immunofluorescence micrograph of the endothelial monolayer indicating the tight junction proteins. Scale bars are all 100 µm. Adapted from Heidari and Taylor *[67]*.

Figure 26 also shows that the molded geometries are not perfectly circular in cross-section, even though the mold protrusions were designed as half-cylinders. Scanning electron microscopy of a representative 3D-printed mold confirmed that the semi-cylindrical mold protrusions were sharply defined at their bases. It is possible that the shape deviations of the molded hydrogels resulted from imperfect wetting of the mold. If imperfect wetting is responsible, it might be improved by increasing the hydrophilicity of the mold prior to casting, for example via a brief oxygen plasma exposure. Another possible explanation for the shape deviations is that the hydrogel's own surface tension may have led to the rounding of sharp corners after gelation and removal from the mold. This second possible behavior could potentially be pre-compensated for to some extent by modifying the mold geometry to include additional, small recesses along the bases of the semi-circular protrusions, so that when the cast hydrogel retreats under the action of surface tension, its final geometry would more closely approximate the desired shape. Nevertheless, the extent to which any lack of lumen cylindricity affects the permeability and hence usefulness of a BBB model is not clear.

4.8. Trans-endothelial electrical resistance of the endothelial lumens

Trans-endothelial electrical resistance (TEER) is a powerful yet convenient technique for characterizing *in vitro* endothelial and epithelial models. The direct current (DC) resistance is associated with greater confluence, or integrity, of the endothelium and with lower permeability of the barrier [64]. It has also been used as a measure of how well-differentiated the endothelial cells are [80]. While conventional TEER measurements are made at a single frequency of voltage excitation (typically around 12.5 Hz [65]) and can therefore report only a single resistance value at a given moment, the use of impedance spectroscopy, involving an excitation frequency sweep, enables a richer model of the endothelial impedance to be uncovered [65]. This is because endothelial barriers are not purely resistive but also exhibit capacitive behavior originating from the cellular membranes and intercellular gaps and crevices.

TEER requires electrodes to be placed on opposite sides of the endothelium, and this is usually achieved with silver–silver chloride electrode pairs immersed in the surrounding medium or embedded into adjacent ECM [65]. Once in place, the electrodes enable constant monitoring of the TEER throughout the culture process, which may last many days. This long-term measurement capability is a distinct advantage over both cell-staining and molecular diffusion observations. However, for most early microfluidic models and without an integrated electrode design, the difficulty of threading an electrode into a cylindrical micro-capillary and the associated risk of damaging the endothelium appeared to have limited the use of electrical measurements in 3D *in vitro* models.

To track the evolution and stability of the endothelia over time, TEER measurements were carried out on two distinct chips every three to four days over an 11.5-day period. These measurements exceed the temporal span of TEER measurements taken from most other reported in vitro models of the BBB (Figure 27c). The TEER of our 3D vascular constructs with co-cultured HMECs and

SY5Y cells reached a maximum average value of 350 Ω.cm^2 after four days. This value reduced to 290 Ω.cm^2 after eight days in vitro and stabilized at this level until the end of the 12-day culture period.

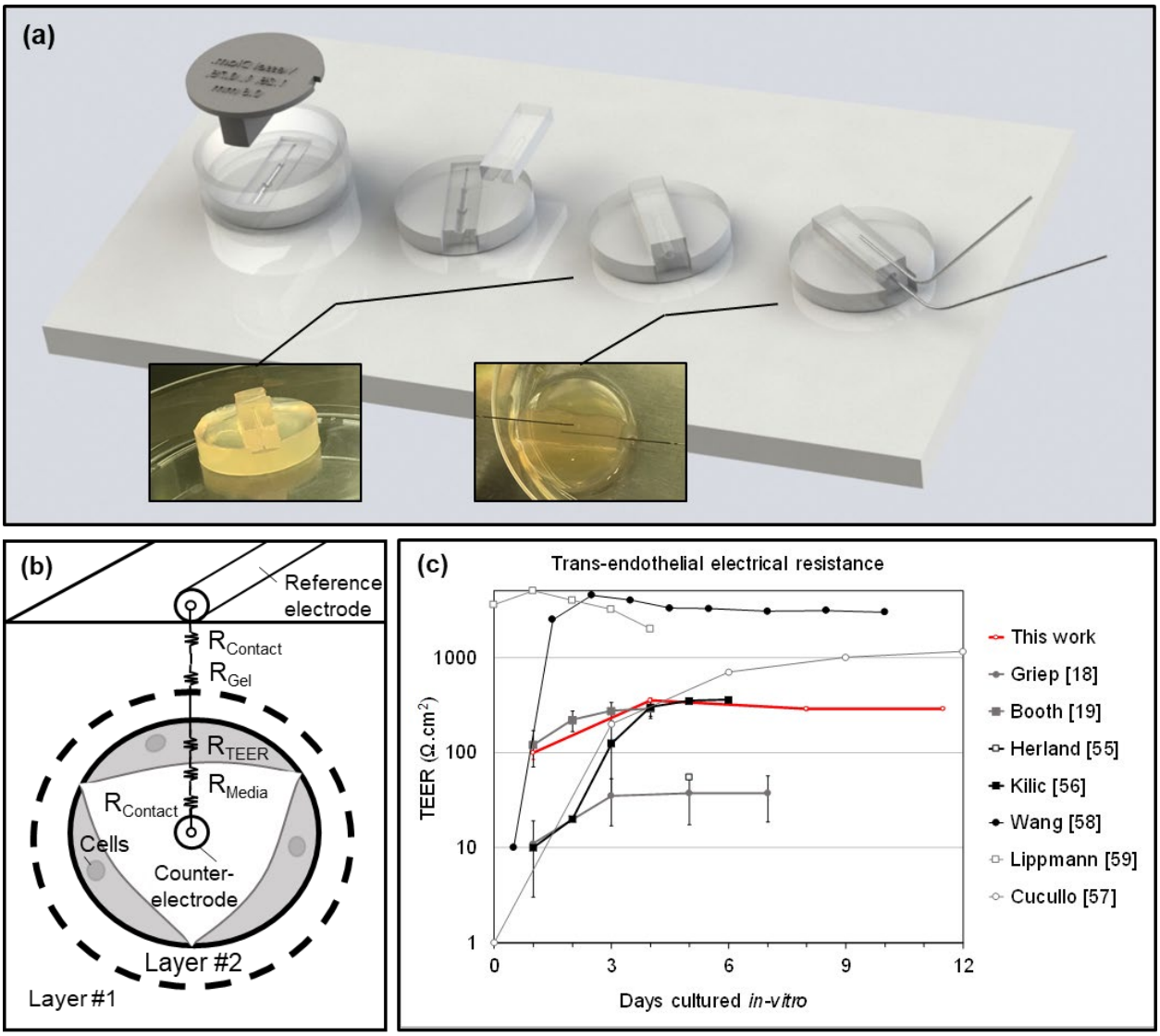

Figure 27 TEER measurement. (a) Electrode configuration and measurement setup. (b) Schematic of the equivalent circuit adopted for the vascular construct. (c) Progression of TEER values over 12 days for the present work and other reported neurovascular unit models. Error bars for our work (red line) indicate ± one sample standard deviation based on at least four independent measurements from each of two separate devices. Error bars are smaller than the symbols in all but the 1-day case. Reproduced from Heidari and Taylor *[67]*.

The TEER values obtained with our platform indicate utility as a BBB model, although, like many previous BBB models, they lie below physiological values, e.g. those of approximately 900–1500 Ω.cm^2 reported for rat brain [81]. One possible explanation for the difference is that our results were obtained after culturing in static conditions, whereas the role of hydrodynamically induced shear stress in promoting tight junction formation has been widely demonstrated, e.g. in Cucullo's

DIV-BBB model [82], where higher and closer-to-physiological TEER values of up to 1200 $\Omega.cm^2$ were obtained after 12 days by applying shear stress to the endothelium. Our structures are, fortunately, compatible with continuous perfusion and culturing conditions could be refined accordingly in the future.

Additionally, retinoic acid is known to play an important role in brain vascular development [61] and it has been observed that the addition of retinoic acid to the culture medium can substantially enhance the tightness of the barrier. Considerably higher TEER values have been reported, e.g. by Wang (> 2000 $\Omega.cm^2$) [83] and Lippmann (~5000 $\Omega.cm^2$) [84], using retinoic acid. These values may in fact be higher than is physiologically realistic. Significantly, Lippmann's system without retinoic acid resulted in TEER values that fell below 300 $\Omega.cm^2$ after less than three days, suggesting that the retinoic acid plays a critical role. Although retinoic acid was not used in the present work, it could easily be incorporated.

Chapter 5
Conclusions

We believe that the mechanics of the cellular microenvironment determine the fate of the tissue construct, cell proliferation and colonization, and the ability of vascular and glial cells to form organic networks within the matrix. As we have demonstrated in this dissertation, an elastic modulus of even a thousand pascals can be too stiff for the HMEC cells and can inhibit cell motility and the formation of microvascular networks. On the other hand, hydrogels of sub-kilopascal stiffness are impossible to print using conventional layer-based additive processes due to their compliance and deformation during the print process. We have further demonstrated the possibility to print perfusable structures with sub-millimeter channel sizes in such low-stiffness matrices.

Apart from the ability of these matrices to support bottom-up vascularization and formation of micro-capillaries in bulk, using the two techniques proposed in this work, we have succeeded in top-down fabrication of complex sub-millimeter architectures such as multi-layered branched networks, multi-vascular architectures and three-dimensional vascular networks. Architecture, geometry and topology of the vascular structure are extremely important, not only from the biological perspectives briefly explained before but also from a fluid mechanics perspective, where the critical effects of biological flow such as pulsatility and wall compliance, and the induced wall shear stress can significantly alter cell growth, morphology and arrangement as well as mass transport either throughout the culture process or after the *in vitro* model is prepared and ready to study.

Every category of human vasculature e.g. coronaries, veins, cerebral vessels, etc. is characterized with specific cell types, tissue layer thicknesses and lumen diameters that result in a unique set of values for permeability, compliance and integrity of that exchange site. For instance, cerebral capillaries are characterized with a very thin and tightly packed layer of endothelial cells covered by pericytes and glial cells whereas coronary arteries consist of a thick layer of smooth muscle cells and elastic tissue offering huge compliance and much less integrity. Therefore, in order to suffice the biological requirements of each category, the multi-layered micro-casting process

allows for the fabrication of an *in vitro* model with the same multilayered tissue composition, mechanical properties and architecture.

The technique can be used to build in vitro vascular structures that are fully embedded in physiologically realistic hydrogels. It eliminates rigid polymeric surfaces from the vicinity of the cells—overcoming a limitation of many microfluidic models—and allows layers of multiple cell types to be defined with tailored ECM composition and stiffness, and in direct contact with each other. We have demonstrated channels with internal diameters as small as 175 μm, and agarose–collagen (AC) gels whose Young's moduli range from 1.4–8.3 kPa. We also showed co-axial geometries with layer thicknesses as small as 125 μm. One potential application of such structures is to simulate brain microvasculature. Towards this goal, the composition and mechanical properties of the composite AC hydrogels are optimized for cell viability and biological performance in both 2D and 3D culture. Seven-day viability of human microvascular endothelial cells (HMECs) and SY5Y glial cells is found to be maximized with a collagen content of 0.05% (w/v) when agarose content ranges between 0.25% and 1% (w/v). Additionally, we quantify the roles of type I bovine and rat-tail collagen, Matrigel, and poly-d-lysine–collagen–Matrigel coatings in promoting HMEC spreading, proliferation and confluence. 3D triple-layer vascular constructs have been fabricated, composed of a cannular monolayer of HMECs surrounded by two regions of SY5Ys with differing spatial densities. The endothelia are confluent and maintain trans-endothelial electrical resistance (TEER) values around 300 $\Omega.cm^2$ over 11.5 days. This prototype opens the way for intricate multi-luminal blood vessels to be fabricated *in vitro*.

With computed axial lithography, we have demonstrated printing in 3% w/v Gel-MA hydrogels with an elastic modulus of approximately 100 Pa. We've also shown that with typical cell seeding densities of a few million cells per mL these matrices enable microcapillary networks to form that span distances of more than 500 μm in only two weeks. The challenges associated with printing high aspect ratio thin-walled channels have been resolved through algorithm modifications and experimental tweaks enabling channels with internal diameters as small as 800 μm to be fabricated. More complex non-axisymmetric bifurcated channels were also printed in 3% w/v Gel-MA hydrogels. Multi-vascular networks and triple-level branched three-dimensional networks were printed in engineering resins and though not achieved yet, are planned to be printed in 3% w/v Gel-MA. Furthermore, an integrated perfusion plugin was engineered and perfected to enable contact-free post-processing and perfusion of the printed hydrogel constructs. This system highlights the unique capability of computed axial lithography in overprinting soft structures on prefabricated solid components positioned within the build volume. Further characterization of the printed constructs with TEER and dye permeability assays is necessary to determine the integrity of the endothelium and is planned for future work.

References

[1] A. Gefen, S. S. Margulies, "Are in vivo and in situ brain tissues mechanically similar?," *Journal of Biomechanics,* vol. 37, no. 9, p. 1339–1352, 2004.

[2] M. T. Prange, S. S. Margulies, "Regional, Directional, and Age-Dependent Properties of the Brain Undergoing Large Deformation," *J Biomech Eng,* vol. 124, no. 2, p. 244–252, 2002.

[3] S. Budday et al. , "Mechanical properties of gray and white matter brain tissue by indentation," *Journal of the Mechanical Behavior of Biomedical Materials,* vol. 46, p. 318–330, 2015.

[4] S. Budday et al., "Mechanical characterization of human brain tissue," *Acta Biomaterialia,* vol. 48, p. 319–340, 2017.

[5] H.-H. G. Song, R. T. Rumma, C. K. Ozaki, E. R. Edelman, and C. S. Chen, "Vascular Tissue Engineering: Progress, Challenges, and Clinical Promise," *Cell Stem Cell,* vol. 22, no. 3, p. 340–354, 2018.

[6] S. Kim, W. Kim, S. Lim, and J. S. Jeon, "Vasculature-On-A-Chip for In Vitro Disease Models," *Bioengineering,* vol. 4, no. 1, p. 8, 2017.

[7] Adam Smith Institute, "Don't have a cow, man: The prospects for lab grown meat," Available: https://www.adamsmith.org/research/dont-have-a-cow-man-the-prospects-for-lab-grown-meat, 2018.

[8] K. Kupferschmidt, "Lab Burger Adds Sizzle to Bid for Research Funds," *Science,* vol. 341, no. 6146, pp. 602-603, 2013.

[9] Discher, Dennis E., Paul Janmey, and Yu-li Wang, "Tissue cells feel and respond to the stiffness of their substrate," *Science,* vol. 310, no. 5751, pp. 1139-1143, 2005.

[10] Dewey, C. F., Bussolari, S. R., Gimbrone, M. A., & Davies, P. F., "The dynamic response of vascular endothelial cells to fluid shear stress," *Journal of biomechanical engineering,* vol. 103, no. 3, pp. 177-185, 1981.

[11] Booth, R., & Kim, H, "Characterization of a microfluidic in vitro model of the blood-brain barrier (μBBB)," *Lab on a chip,* vol. 12, pp. 1784-1792, 2012.

[12] Adriani, G., Ma, D., Pavesi, A., Kamm, R. D., & Goh, E. L., "A 3D neurovascular microfluidic model consisting of neurons, astrocytes and cerebral endothelial cells as a blood–brain barrier," *Lab on a Chip,* vol. 17, no. 3, pp. 448-459, 2017.

[13] Ford, M. C., Bertram, J. P., Hynes, S. R., Michaud, M., Li, Q., Young, M., ... & Lavik, E. B., "A macroporous hydrogel for the coculture of neural progenitor and endothelial cells to form functional vascular networks invivo," *Proceedings of the National Academy of Sciences of the United States of America,* vol. 103, no. 8, pp. 2512-2517, 2006.

[14] Zervantonakis, I. K., Hughes-Alford, S. K., Charest, J. L., Condeelis, J. S., Gertler, F. B., & Kamm, R. D., "Three-dimensional microfluidic model for tumor cell intravasation and endothelial barrier function," *Proceedings of the National Academy of Sciences,* vol. 109, no. 34, pp. 13515-13520, 2012.

[15] Guo, S., Kim, W. J., Lok, J., Lee, S. R., Besancon, E., Luo, B. H., ... & Lo, E. H., "Neuroprotection via matrix-trophic coupling between cerebral endothelial cells and neurons," *Proceedings of the National Academy of Sciences,* vol. 105, no. 21, pp. 7582-7587, 2008.

[16] Bischel, L. L., Young, E. W., Mader, B. R., & Beebe, D. J, "Tubeless microfluidic angiogenesis assay with three-dimensional endothelial-lined microvessels," *Biomaterials,* vol. 34, pp. 1471-1477, 2013.

[17] Herland, A., van der Meer, A. D., FitzGerald, E. A., Park, T. E., Sleeboom, J. J., & Ingber, D. E., "Distinct contributions of astrocytes and pericytes to neuroinflammation identified in a 3D human blood-brain barrier on a chip," *PLoS One,* vol. 11, no. 3, 2016.

[18] Mannino, R. G., Santiago-Miranda, A. N., Pradhan, P., Qiu, Y., Mejias, J. C., Neelapu, S. S., ... & Lam, W. A., *Lab on a Chip,* vol. 17, no. 3, pp. 407-414, 2017.

[19] Kolesky, D. B., Truby, R. L., Gladman, A., Busbee, T. A., Homan, K. A., & Lewis, J. A, *Advanced materials,* vol. 26, pp. 3124-3130, 2014.

[20] Norotte, C., Marga, F. S., Niklason, L. E., & Forgacs, G, "Scaffold-free vascular tissue engineering using bioprinting," *Biomaterials,* vol. 30, pp. 5910-5917, 2009.

[21] Jakab, K., Norotte, C., Damon, B., Marga, F., Neagu, A., Besch-Williford, C. L., ... & Markwald, R, "Tissue engineering by self-assembly of cells printed into topologically defined structures," *Tissue Engineering Part A,* vol. 14, pp. 413-421, 2008.

[22] Bektas, C. K., & Hasirci, V., "Cell loaded 3D bioprinted GelMA hydrogels for corneal stroma engineering," *Biomaterials science,* vol. 8, no. 1, pp. 438-449, 2020.

[23] Zhuang, P., Ng, W. L., An, J., Chua, C. K., & Tan, P., "Layer-by-layer ultraviolet assisted extrusion-based (UAE) bioprinting of hydrogel constructs with high aspect ratio for soft tissue engineering applications.," *PLOS One,* vol. 14, no. 6, 2019.

[24] Berg, J., Hiller, T., Kissner, M. S., Qazi, T. H., Duda, G. N., Hocke, A. C., Kurreck, J. , "Optimization of cell-laden bioinks for 3D bioprinting and efficient infection with influenza A virus," *Scientific reports,* vol. 8, no. 1, pp. 1-13, 2018.

[25] Noor, N., Shapira, A., Edri, R., Gal, I., Wertheim, L., & Dvir, T., "Tissue Engineering: 3D Printing of Personalized Thick and Perfusable Cardiac Patches and Hearts," *Advanced Science,* vol. 6, no. 11, 2019.

[26] Ji, S., Almeida, E., & Guvendiren, M., "3D bioprinting of complex channels within cell-laden hydrogels," *Acta biomaterialia,* vol. 95, pp. 214-224, 2019.

[27] Jia, W., Gungor-Ozkerim, P. S., Zhang, Y. S., Yue, K., Zhu, K., Liu, W., ... & Khademhosseini, A., "Direct 3D bioprinting of perfusable vascular constructs using a blend bioink," *Biomaterials,* vol. 106, pp. 58-68, 2016.

[28] Mironov, V., Visconti, R. P., Kasyanov, V., Forgacs, G., Drake, C. J., & Markwald, R. R, *Biomaterials,* vol. 30, pp. 2164-2174, 2009.

[29] Hinton, T. J., Jallerat, Q., Palchesko, R. N., Park, J. H., Grodzicki, M. S., Shue, H. J., ... & Feinberg, A. W., "Three-dimensional printing of complex biological structures by freeform reversible embedding of suspended hydrogels," *Science advances,* vol. 1, no. 9, 2015.

[30] Lee, A., Hudson, A. R., Shiwarski, D. J., Tashman, J. W., Hinton, T. J., Yerneni, S., ... & Feinberg, A. W. , "3D bioprinting of collagen to rebuild components of the human heart," *Science,* vol. 365, no. 6452, pp. 482-487, 2019.

[31] Huang, T. Q., Qu, X., Liu, J., & Chen, S, "3D printing of biomimetic microstructures for cancer cell migration," *Biomedical microdevices,* vol. 16, pp. 127-132, 2014.

[32] Hahn, M. S., Taite, L. J., Moon, J. J., Rowland, M. C., Ruffino, K. A., & West, J. L., "Photolithographic patterning of polyethylene glycol hydrogels," *Biomaterials,* vol. 27, no. 12, pp. 2519-2524, 2006.

[33] Zhu, W., Qu, X., Zhu, J., Ma, X., Patel, S., Liu, J., ... & Zhang, K., "Direct 3D bioprinting of prevascularized tissue constructs with complex microarchitecture," *Biomaterials,* vol. 124, pp. 106-115, 2017.

[34] Grigoryan, B., Paulsen, S. J., Corbett, D. C., Sazer, D. W., Fortin, C. L., Zaita, A. J., ... & Johansson, F. , "Multivascular networks and functional intravascular topologies within biocompatible hydrogels," *Science,* vol. 364, no. 6439, pp. 458-464, 2019.

[35] Ma, X., Yu, C., Wang, P., Xu, W., Wan, X., Lai, C. S. E., ... & Chen, S. , "Rapid 3D bioprinting of decellularized extracellular matrix with regionally varied mechanical properties and biomimetic microarchitecture," *Biomaterials,* vol. 185, pp. 310-321, 2018.

[36] Zhu, W., Tringale, K. R., Woller, S. A., You, S., Johnson, S., Shen, H., ... & Yaksh, T. L., "Rapid continuous 3D printing of customizable peripheral nerve guidance conduits," *Materials Today,* vol. 21, no. 9, pp. 951-959, 2018.

[37] Shusteff, M., Browar, A. E., Kelly, B. E., Henriksson, J., Weisgraber, T. H., Panas, R. M., ... & Spadaccini, C. M., "One-step volumetric additive manufacturing of complex polymer structures," *Science advances,* vol. 3, no. 12, p. 5496, 2017.

[38] Shin, Y., Jeon, J. S., Han, S., Jung, G. S., Shin, S., Lee, S. H., ... & Chung, S., "In vitro 3D collective sprouting angiogenesis under orchestrated ANG-1 and VEGF gradients," *Lab on a chip,* vol. 11, no. 13, pp. 2175-2181, 2011.

[39] Leslie-Barbick, J. E., Moon, J. J., & West, J. L., "Covalently-immobilized vascular endothelial growth factor promotes endothelial cell tubulogenesis in poly (ethylene glycol) diacrylate hydrogels.," *Journal of Biomaterials Science, Polymer Edition,* vol. 20, no. 12, pp. 1763-1779, 2009.

[40] Hsu, Y. H., Moya, M. L., Hughes, C. C., George, S. C., & Lee, A. P. , "A microfluidic platform for generating large-scale nearly identical human microphysiological vascularized tissue arrays," *Lab on a chip,* vol. 13, no. 5, pp. 2990-2998, 2013.

[41] DeLong, S. A., Gobin, A. S., & West, J. L., "Covalent immobilization of RGDS on hydrogel surfaces to direct cell alignment and migration," *Journal of Controlled Release,* vol. 109, no. 1-3, pp. 139-148, 2005.

[42] Puleo, D. A., & Bizios, R., "RGDS tetrapeptide binds to osteoblasts and inhibits fibronectin-mediated adhesion," *Bone,* vol. 12, no. 4, pp. 271-276, 1991.

[43] Browning, M. B., Cereceres, S. N., Luong, P. T., & Cosgriff-Hernandez, E. M., "Determination of the in vivo degradation mechanism of PEGDA hydrogels," *Journal of Biomedical Materials Research Part A,* vol. 102, no. 12, pp. 4244-4251, 2014.

[44] Qiu, Y., Lim, J. J., Scott Jr, L., Adams, R. C., Bui, H. T., & Temenoff, J. S., "PEG-based hydrogels with tunable degradation characteristics to control delivery of marrow stromal cells for tendon overuse injuries," *Acta biomaterialia,* vol. 7, no. 3, pp. 959-966, 2011.

[45] Yue, K., Trujillo-de Santiago, G., Alvarez, M. M., Tamayol, A., Annabi, N., & Khademhosseini, A., "Synthesis, properties, and biomedical applications of gelatin methacryloyl (GelMA) hydrogels," *Biomaterials,* vol. 73, pp. 254-271, 2015.

[46] Gao, G., Schilling, A. F., Hubbell, K., Yonezawa, T., Truong, D., Hong, Y., ... & Cui, X. , "Improved properties of bone and cartilage tissue from 3D inkjet-bioprinted human mesenchymal stem cells by simultaneous deposition and photocrosslinking in

Photocrosslinking in PEG-GelMA.," *Biotechnology letters,* vol. 37, no. 11, pp. 2349-2355, 2015.

[47] Khalil, S., & Sun, W., "Bioprinting endothelial cells with alginate for 3D tissue constructs," *Journal of biomechanical engineering,* vol. 131, no. 11, 2009.

[48] Song, S. J., Choi, J., Park, Y. D., Hong, S., Lee, J. J., Ahn, C. B., ... & Sun, K. , "Sodium alginate hydrogel-based bioprinting using a novel multinozzle bioprinting system," *Artificial organs,* vol. 35, no. 11, pp. 1132-1136, 2011.

[49] Gao, G., Lee, J. H., Jang, J., Lee, D. H., Kong, J. S., Kim, B. S., ... & Cho, D. W., "Tissue engineered bio-blood-vessels constructed using a tissue-specific bioink and 3D coaxial cell printing technique: a novel therapy for ischemic disease," *Advanced functional materials,* vol. 27, no. 33, 2017.

[50] Wu, Z., Su, X., Xu, Y., Kong, B., Sun, W., & Mi, S., "Bioprinting three-dimensional cell-laden tissue constructs with controllable degradation," *Scientific reports,* vol. 6, no. 1, pp. 1-10, 2016.

[51] Huang, J., Fu, H., Wang, Z., Meng, Q., Liu, S., Wang, H., ... & Zhang, Z., "BMSCs-laden gelatin/sodium alginate/carboxymethyl chitosan hydrogel for 3D bioprinting," *Rsc Advances,* vol. 6, no. 110, pp. 108423-108430, 2016.

[52] Price, G. M., Wong, K. H., Truslow, J. G., Leung, A. D., Acharya, C., & Tien, J., "Effect of mechanical factors on the function of engineered human blood microvessels in microfluidic collagen gels," *Biomaterials,* vol. 31, no. 24, pp. 6182-6189, 2010.

[53] Sundararaghavan, H. G., Masand, S. N., & Shreiber, D. I., "Microfluidic generation of haptotactic gradients through 3D collagen gels for enhanced neurite growth," *Journal of neurotrauma,* vol. 28, no. 11, pp. 2377-2387, 2011.

[54] Leclerc, E., Sakai, Y., & Fujii, T. , "Cell culture in 3-dimensional microfluidic structure of PDMS (polydimethylsiloxane)," *Biomedical microdevices,* vol. 5, no. 2, pp. 109-114, 2003.

[55] Rhee, S., Puetzer, J. L., Mason, B. N., Reinhart-King, C. A., & Bonassar, L. J., "3D bioprinting of spatially heterogeneous collagen constructs for cartilage tissue engineering," *ACS Biomaterials Science & Engineering,* vol. 2, no. 10, pp. 1800-1805, 2016.

[56] Stratesteffen, H., Köpf, M., Kreimendahl, F., Blaeser, A., Jockenhoevel, S., & Fischer, H. , "GelMA-collagen blends enable drop-on-demand 3D printablility and promote angiogenesis," *Biofabrication,* vol. 9, no. 4, 2017.

[57] Fan, R., Piou, M., Darling, E., Cormier, D., Sun, J., & Wan, J. (2016). , 31(5), 684-692., "Bio-printing cell-laden Matrigel–agarose constructs," *Journal of biomaterials applications,* vol. 31, no. 5, pp. 684-692, 2016.

[58] López-Marcial, G. R., Zeng, A. Y., Osuna, C., Dennis, J., García, J. M., & O'Connell, G. D. (2018).. , 4(10), 3610-3616., "Agarose-Based Hydrogels as Suitable Bioprinting Materials for Tissue Engineering," *ACS Biomaterials Science & Engineering,* vol. 4, no. 10, pp. 3610-3616, 2018.

[59] Huh, J. T., Yoo, J. J., Atala, A., & Lee, S. J., "Three-dimensional bioprinting for tissue engineering," *Principles of Tissue Engineering,* pp. 1391-1415, 2020.

[60] Chen, D. X. , "Biomaterials for Bioprinting," in *Extrusion Bioprinting of Scaffolds for Tissue Engineering Applications*, Springer, 2019, pp. 33-48.

[61] A. P. Balgude, X. Yu, A. Szymanski, and R. V. Bellamkonda, "Agarose gel stiffness determines rate of DRG neurite extension in 3D cultures," *Biomaterials,* vol. 22, no. 10, pp. 1077-1084, 2001.

[62] Y. Luo and M. S. Shoichet, "Light-Activated Immobilization of Biomolecules to Agarose Hydrogels for Controlled Cellular Response," *Biomacromolecules,* vol. 5, no. 6, pp. 2315-2323, 2004.

[63] Oliver, W. C., & Pharr, G. M., "Measurement of hardness and elastic modulus by instrumented indentation: Advances in understanding and refinements to methodology," *Journal of materials research,* vol. 19, no. 1, pp. 3-20, 2004.

[64] Benson, K.; Cramer, S.; Galla, H., *Fluids and Barriers of the CNS,* vol. 10, no. 1, p. 5, 2013.

[65] Srinivasan, B., Kolli, A. R., Esch, M. B., Abaci, H. E., Shuler, M. L., & Hickman, J. J., *Journal of laboratory automation,* vol. 20, no. 2, pp. 107-126, 2015.

[66] Y. Qiu et al., "Microvasculature-on-a-chip for the long-term study of endothelial barrier dysfunction and microvascular obstruction in disease," *Nature Biomedical Engineering,* vol. 2, no. 6, p. 453, 2018.

[67] Heidari, H., & Taylor, H. , "Multilayered microcasting of agarose–collagen composites for neurovascular modeling," *Bioprinting,* vol. 17, no. 69, 2020.

[68] "Vero Clear.", "http://www.stratasys.com/materials/search/veroclear," [Accessed: 26-Aug-2018].

[69] X. Zheng et al., "Design and optimization of a light-emitting diode projection micro-stereolithography three-dimensional manufacturing system," *Review of Scientific Instruments,* vol. 83, no. 12, p. 125001, 2012.

[70] Kelly, B. E., Bhattacharya, I., Heidari, H., Shusteff, M., Spadaccini, C. M., & Taylor, H. K., "Volumetric additive manufacturing via tomographic reconstruction," *Science,* vol. 363, no. 6431, pp. 1075-1079, 2019.

[71] J. Kastner, C. Heinzl, Integrated Imaging and Vision Techniques for Industrial Inspection: Advances in Computer Vision and Pattern Recognition, London: Springer, 2015, pp. 227-250.

[72] A. K. O'Brien, C. N. Bowman, "Impact of oxygen on photopolymerization kinetics and polymer structure," *Macromolecules,* vol. 39, pp. 2501-2506, 2006.

[73] Tzima, E., Irani-Tehrani, M., Kiosses, W. B., Dejana, E., Schultz, D. A., Engelhardt, B., ... & Schwartz, M. A., "A mechanosensory complex that mediates the endothelial cell response to fluid shear stress," *Nature,* vol. 437, no. 7057, pp. 426-431, 2005.

[74] R. Sudo et al., "Transport-mediated angiogenesis in 3D epithelial coculture," *FASEB J,* vol. 23, no. 7, pp. 2155-2164, 2009.

[75] Heidari, H., Kelly, B., Bhattacharya, I., & Taylor, H., "Support-free direct 3D-printing of millifluidic and microfluidic chips with tunable stiffness through computed axial lithography," in *Microfluidics, BioMEMS, and Medical Microsystems XVII*, San Fransisco, 2019.

[76] Q. Wu, Y. Zhang, and Q. Chen, "Indian hedgehog Is an Essential Component of Mechanotransduction Complex to Stimulate Chondrocyte Proliferation," *J. Biol. Chem.,* vol. 276, no. 38, pp. 35290-35296, 2001.

[77] D. E. Jaalouk and J. Lammerding, "Mechanotransduction gone awry," *Nature Reviews Molecular Cell Biology,* vol. 10, no. 1, pp. 63-73, 2009.

[78] A. P. Balgude, X. Yu, A. Szymanski, and R. V. Bellamkonda, "Agarose gel stiffness determines rate of DRG neurite extension in 3D cultures," *Biomaterials,* vol. 22, no. 10, pp. 1077-1084, 2001.

[79] S. Han et al., "Constructive remodeling of a synthetic endothelial extracellular matrix," *Scientific Reports,* vol. 5, p. 18290, 2015.

[80] Wolff, A., Antfolk, M., Brodin, B., & Tenje, M., *Journal of pharmaceutical sciences,* vol. 104, no. 9, pp. 2727-2746, 2015.

[81] A. M. Butt, H. C. Jones, and N. J. Abbott , "Electrical resistance across the blood-brain barrier in anaesthetized rats: a developmental study," *The Journal of Physiology,* vol. 429, no. 1, pp. 47-62, 1990.

[82] L. Cucullo et al., "Immortalized Human Brain Endothelial Cells and Flow-Based Vascular Modeling: A Marriage of Convenience for Rational Neurovascular Studies," *J Cereb Blood Flow Metab,* vol. 28, no. 2, pp. 312-328, 2008.

[83] Y. I. Wang, H. E. Abaci, and M. L. Shuler, "Microfluidic blood–brain barrier model provides in vivo-like barrier properties for drug permeability screening," *Biotechnology and Bioengineering,* vol. 114, no. 1, p. 184–194, 2016.

[84] E. S. Lippmann, A. Al-Ahmad, S. M. Azarin, S. P. Palecek, and E. V. Shusta, "A retinoic acid-enhanced, multicellular human blood-brain barrier model derived from stem cell sources," *Scientific Reports,* vol. 4, p. 4160, 2014.